FZR-413

Pavel Evtushenko

Electron Beam Diagnostic at the ELBE Free Electron Laser

FZR Forschungszentrum
Rossendorf

Pavel Evtushenko

Electron Beam Diagnostic
at the ELBE Free Electron Laser

**Forschungszentrum
Rossendorf**

Electron Beam Diagnostic
at the ELBE Free Electron Laser

Dissertation
zur Erlangung des akademischen Grades
Doctor rerum naturalium
(Dr. rer. nat.)

vorgelegt
der Fakultät Mathematik und Naturwissenschaften
der Technischen Universität Dresden

von
Pavel Evtushenko, Magister der Physik
geboren am 15. April 1975
in Berdsk, Russland

Contents

List of Figures

List of Tables

Introduction

   The radiation source ELBE is a scientific user facility able to generate electromagnetic radiation as well as beams of secondary particles. The figure below shows the layout of the facility. ELBE is based on a superconducting electron linac. The linac consists of two accelerating modules and uses TESLA type nine-cell niobium cavities, two cavities in each module. The cavities were developed at DESY in the framework of the TESLA linear collider project and the X-ray free electron laser (FEL) project. The ELBE linac is designed to operate with an accelerating field gradient of 10 MV/m so that the maximum design electron beam energy at the exit of the second module is 40 MeV. The essential difference of the ELBE linac from the future TESLA and X-ray FEL linacs is that ELBE operates in the continuous wave (CW) mode. ELBE delivers an electron beam with an average current of up to 1 mA. The electron source is a DC thermionic triode delivering beam with energy of 250 keV. The gun beam quality predefines the accelerated beam quality.

   One application of the electron beam is the generation of bremsstrahlung in the MeV energy range. The bremsstrahlung is used for nuclear spectroscopy experiments. Another application of the electron beam is the generation of quasi-monochromatic X-rays via channeling radiation in a single crystal. Thus X-rays with an energy from 10 keV through 100 keV can be generated. The channeling radiation is used for radio-biological and bio-medical experiments. In the future the ELBE electron beam will be used to produce monoenergetic positrons for material research. One more future application of the beam is the production of neutrons by bremsstrahlung via (γ,n) reactions. The neutrons will be used for material research oriented toward construction of future nuclear fusion reactors.

   In the author's opinion, the most exciting and elegant application of the electron beam at ELBE is the infrared FEL. There are two FELs planned to run simultaneously at ELBE. The first one, with an undulator period of 27 mm, is going to operate in the wavelength range from 3 µm through 30 µm. The second one is in the design stage only but it will be built to work at longer wavelengths from 25 µm to 150 µm where the FEL has no competition from conventional quantum lasers. While an infrared FEL makes possible a great variety of experiments it is the device most sensitive to the electron beam quality.

   This dissertation is dedicated to the development of beam instrumentation and the measurement of electron beam parameters at ELBE.

- In Chapter #1 we review fundamentals of FEL operation, discuss the importance of the electron beam quality for the FEL and lay down the requirements imposed by the FEL on the electron beam parameters.
- Chapter #2 describes measurements of the transverse emittance we did at ELBE including an explanation of the experimental methods and the measurement

error analysis. The transverse emittance was measured with the multislit method in the injector where the beam is space charge dominated. The transverse emittance of the accelerated beam was measured with the quadrupole scan method since the beam is emittance dominated.

- Measurements of the electron bunch length, which is in the picosecond range, are described in Chapter #3. The bunch length was estimated from a frequency domain fit of a specially constructed analytical function to the measured power spectrum of the bunch. The power spectrum was obtained as a Fourier transform of the measured autocorrelation function of the coherent transition radiation (CTR). The CTR autocorrelation function was measured with the help of a Martin-Puplett interferometer.
- A system of beam position monitors was designed, built, and commissioned in the framework of this effort. The design of our stripline BPM, the corresponding electronics and software is described in Chapter #4 along with the system performance as measured with the ELBE beam.
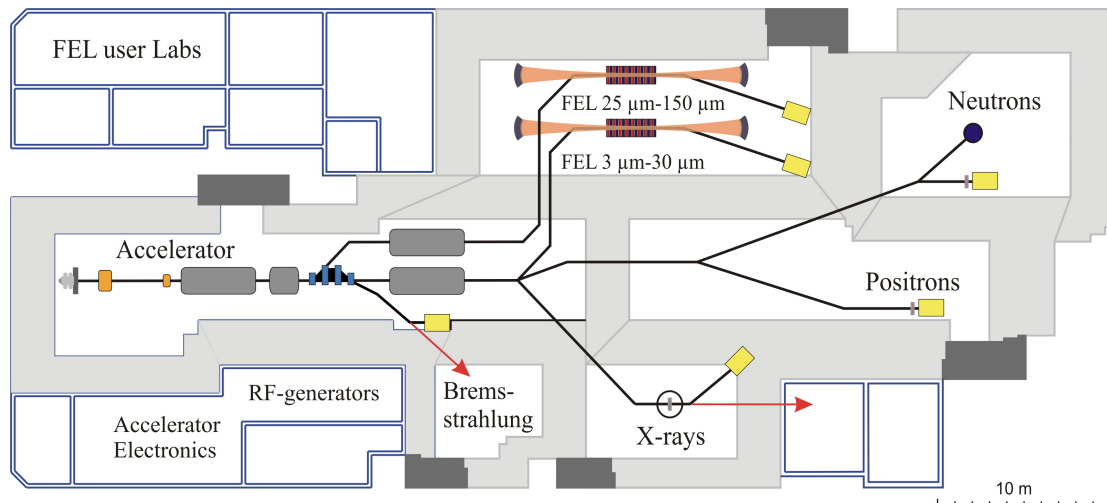
Layout of the radiation source ELBE

Chapter 1

Fundamentals of FEL operation

1.1 Introduction

The free electron laser (FEL) is a device utilizing an electron beam to produce an electromagnetic radiation. The name laser is originated from "**L**ight **A**mplification by **S**timulated **E**mission of **R**adiation". An FEL rightfully belongs to the laser family, though its structure differs a lot from conventional quantum lasers. An FEL can operate in the amplifier mode as well as in the oscillator mode. In both cases the gain medium is an electron beam traveling in the periodic magnetic field. A device supplying this magnetic field is called an undulator or wiggler. In the case of the amplifier FEL an external electromagnetic (EM) radiation is intensified. In an oscillator FEL, which is the ELBE case, an optical resonator is used to store the radiation of the electrons, which they produce in the undulator. Thus the electron beam radiates not only in the undulator field but due to the field stored in the resonator as well. This is the case of stimulated emission and for this reason an FEL is a real laser. In this chapter we will briefly consider the basic physical issues of the FEL operation. At first we will consider trajectories of the electrons in the undulator. Then we will discuss properties of the spontaneous undulator emission of the electrons, i.e., radiation from the field of the undulator. As a next step we will combine the radiation field and the undulator field to describe the stimulated emission. Then we consider the FEL gain. By the end of this chapter we discuss the influence of the electron beam quality on the FEL gain to show its importance and to set requirements for FEL electron beam diagnostics, which is the main subject of this thesis.

1.2 Electron trajectory in the undulator

A coordinate system is used where the electrons are propagating in *z* direction and the magnetic field of the undulator is vertical, as it is pictured in Fig. 1.1. Let us assume for simplicity that the undulator is infinite in the *x* direction. Of course, it is not so in practice, but since normally an undulator width in the *x* direction is much bigger than the distance between the undulator poles, such approximation shows correctly the main physical aspects, which we want to discuss now. In practice an FEL utilizes an electron beam with energy from a few MeV up to some hundreds of MeV. This is why we have to carry out all our considerations in the frame of the special theory of relativity. The Hamiltonian of the relativistic electrons in the undulator is

$$H = \left[\left(\vec{P} - \frac{e}{c} \vec{A} \right)^2 c^2 + m^2 c^4 \right]^{1/2}, \tag{1.1}$$

where $\vec{P}$ is the canonical momentum, $\vec{A}$ is the vector potential of the undulator, *m* is the electron mass and *c* is the light velocity in vacuum. The scalar potential is set to zero here, because we neglect the space charge effects. Since a static magnetic field does no work on the electrons, the energy of the electrons in the undulator field is constant. Hence we can write [1.1,1.2]

$$H = \gamma mc^2 \qquad \text{and} \qquad \dot{\gamma} = 0. \tag{1.2}$$

where γ is the relativistic Lorentz factor $\gamma = 1/\sqrt{1-\beta^2}$ and β is the normalized velocity of the electron $\beta = v/c$. The Hamiltonian does not depend on the generalized coordinates. For this reason we have the canonical equations

$$\dot{P}_x = -\frac{\partial H}{\partial x} = 0, \qquad \dot{P}_y = -\frac{\partial H}{\partial y} = 0. \tag{1.3 a, b}$$

These equations give two constants of motion and can be rewritten in the following form

$$\frac{d}{dt}(m\gamma c\beta_x + eA_x/c) = 0 \qquad \text{and} \qquad \frac{d}{dt}(m\gamma c\beta_y + eA_y/c) = 0. \tag{1.4 a, b}$$
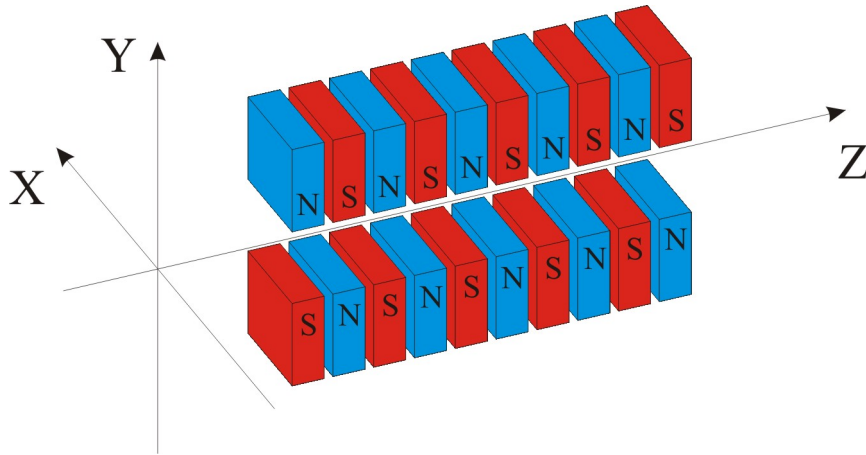
Figure 1.1 Coordinate system

Before an electron enters the undulator field we have the following conditions: $\beta_x = \beta_y = 0$ and $A_x = A_y = 0$. Now we recall our assumption that the undulator is infinite in the x direction. The magnetic field of the undulator has only a vertical component $B_y = B_0 \cos(k_u z)$ on the undulator axis, here $k_u = \dfrac{2\pi}{\lambda_u}$ and λ_u is the undulator period. The vector potential, which provides such a field is $A_x = (B_0 / k_u) \sin(k_u z)$, here B_0 is the amplitude of the magnetic field on the undulator axis. The equation of motion is obtained directly from the definitions $\dot{x} = c\beta_x$ and $\dot{y} = c\beta_y$. It is also convenient to introduce so-called undulator parameter $K = \dfrac{B_0 e}{k_u mc^2}$. Then the equations of the transverse motion look like

$$\dot{x} = -\frac{c \cdot K}{\gamma} \sin(k_u z) \quad \text{and} \quad \dot{y} = 0. \tag{1.5 a, b}$$

To obtain the equation of the longitudinal motion we set P_x and P_y to zero in Eq. (1.1). This is correct because of Eq. (1.3). We also use A_x of the undulator. With the help of the canonical equation one gets

$$\dot{\beta}_z = -\frac{ck_u K^2}{2\gamma^2} \sin(2k_u z). \tag{1.6}$$

The solution of the equation of motion is easy to find in the approximation when $\beta_z \approx 1$ and $\beta_x \ll 1$. Then the equations describing the electron trajectory are [1.1]

$$x = \frac{K}{\gamma \cdot k_u \beta_0}(\cos(k_u c\beta_0 t) - 1) + x_0, \quad y = y_0, \tag{1.7 a, b}$$

$$z = c\beta_0 t + \frac{K^2}{8\gamma^2 \cdot k_u \beta_0^2} \sin(2k_u c\beta_0 t) \tag{1.7 c}$$

where $\beta_0 = \sqrt{1 - (1 + K^2 / 2) / \gamma^2}$ is the average longitudinal electron velocity in the undulator. The motion in the x direction is an oscillation with the frequency $k_u c\beta_0$ and the amplitude $\dfrac{K}{k_u \beta_0 \lambda}$. The electron does not move in the y direction in this approximation. Longitudinally the electron travels in the undulator with the average velocity β_0 oscillating with the double frequency of the transverse oscillations $2k_u c\beta_0$, so that in the frame moving with the average electron velocity β_0 the electron trajectory is an eight-like figure [1.2].

As mentioned above the magnetic field used in the calculations is not realistic. Such a field does not even satisfy Maxwell's equations. One has to take the correct field to see one more physical aspect of the electron motion in an undulator. In a real undulator the magnetic field near the undulator poles is stronger than in the middle plane. Because of this fact the electrons propagating in the undulator are oscillating in the vertical direction too. These are the so-called betatron oscillations. The wavelength of these oscillations is $\lambda_\beta = \lambda_u \sqrt{2} \dfrac{\gamma}{K}$ [1.1].

Let us now make simple estimates of the beam trajectory in the ELBE undulator. The first interesting question is the amplitude of the transverse oscillations. For the typical ELBE parameters like an electron beam energy of 20 MeV, an undulator period of 27 mm, and an undulator parameter K=1, the amplitude $\dfrac{K\lambda_u}{2\pi\gamma\beta_0}$ is about 0.1 mm. The betatron oscillation period λ_β for the same beam and undulator parameters is about 153 cm.

1.3   Spontaneous emission

We saw in the previous section that an electron moves in the undulator with a non-constant velocity, i.e., $\dot{\vec{\beta}} \neq 0$. Hence, as a charged particle, the electron radiates an electromagnetic field. Here we will discuss the basic characteristics of this radiation. Let us consider an undulator with N_U periods. The overall length of the undulator is then $L = N_U\lambda_u$. The electron executes N_U oscillations passing the undulator. Obviously, the wave radiated by the electron consists of N_U periods as well. The length of the wave is the path difference of light and the electron in the time, which the electron needs to pass the undulator. If the electron velocity is $v = \beta c$, then its travel time in the undulator is $t = N_U\lambda_u / \beta c$. In this time period the light covers a distance ct and the electron covers distance vt. The radiation wavelength is the ratio of the packet length to the number of oscillations in it

$$\lambda = \frac{(c-v)t}{N_U} = \lambda_u \frac{1-\beta}{\beta}. \tag{1.8}$$

In a relativistic case, taking into account that $\beta \approx 1$, one can rewrite this equation as the following

$$\lambda = \frac{\lambda_u}{2\gamma^2}. \tag{1.9}$$

Deriving the formula we did one very strong simplification. We have assumed the electron moves in the undulator linearly as if the undulator does not change its trajectory. This is why the undulator parameter *K*, which is a characteristic of the undulator strength, is not in the formula, which is obviously wrong. But what the formula (1.9) shows correctly is the dependence on the undulator period λ_u and the electron energy. It is also very easy to see from the simple derivation that the $1/\gamma^2$ dependence is just a kinematical effect coming from the velocity difference of the electron and light. To see a dependence on the undulator strength one has to take into account details of the electron trajectory in the undulator. Imagine we are observing the radiation at the angle θ with respect to the undulator axis. Since the electron is relativistic its radiation is concentrated in the cone with a very small opening angle $1/\gamma$. Thus we see the radiation of the electron emitted in each period in the undulator but only in certain phase of the transverse oscillations, i.e. the radiation intensity is modulated. It is easy to show that the period of the modulation is

$$T = \frac{\lambda_u}{c}\left(\frac{1}{\beta_z} - cos(\theta)\right). \tag{1.10}$$

Since the deflection of the electron is small in the undulator θ is also small and we can use $cos(\theta) \approx 1 - \theta^2/2$. Now it is time to recall results we have obtained in Section 1.2. One can show, using Eq. (1.5a) and going through a simple mathematics that $(1 - \beta_z) = \dfrac{1}{2\gamma^2}(1 + K^2_{RMS})$, where $K_{RMS} = K/\sqrt{2}$ for a planar undulator. Then we get the well-known formula for the undulator radiation wavelength

$$\lambda = \frac{\lambda_u}{2 \cdot \gamma^2}(1 + K^2_{RMS} + \gamma^2\theta^2). \qquad (1.11)$$

Practically speaking, K is one in order of magnitude and can be adjusted in a small range by changing the field strength on the undulator axis. This can be done by either changing the distance between opposite pairs of magnets in the case of a permanent magnet undulator or by changing the current in an electromagnetic undulator coil. This is one possibility for changing the radiation wavelength. Another way to do this is to change the electron energy, which can be made to vary over a relatively wide range.
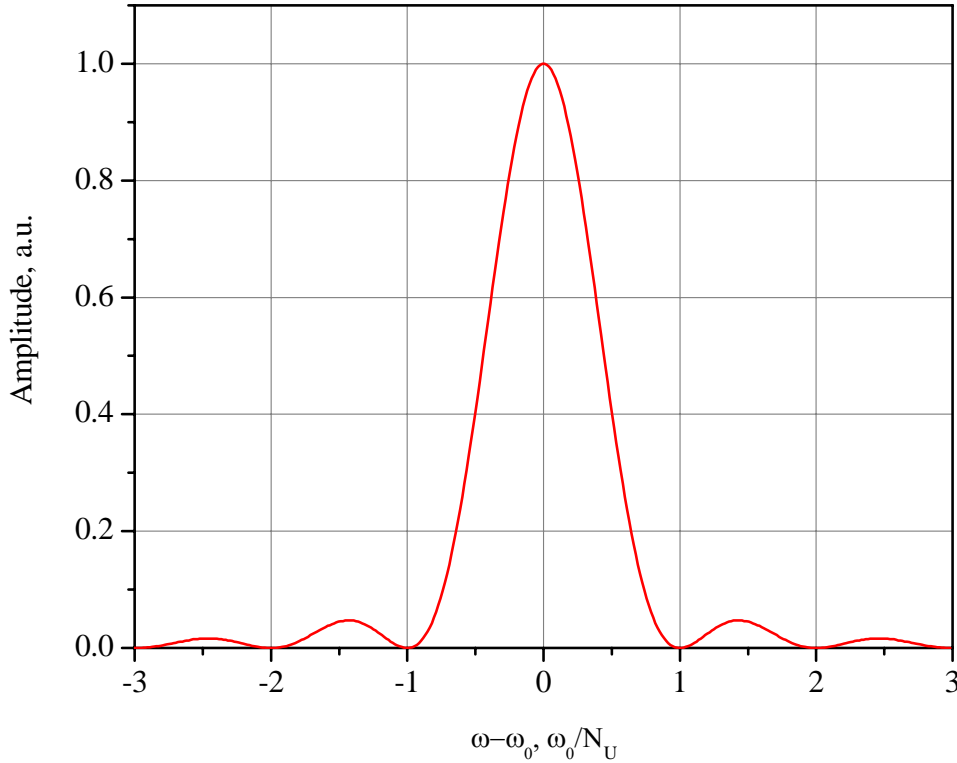
Figure 1.2 Spectrum of the spontaneous radiation

Another important characteristic of the radiation is its spectrum. If the radiation train, produced by an electron passing an undulator were infinitely long then a spectrum of the radiation would have only one frequency corresponding to the wavelength given by Eq. (1.11). In other words the spectrum would be one infinitely narrow line. Since the radiation train has a length of $\dfrac{N_U\lambda}{c}$ the frequency is not

uniquely defined. The spectrum and the time domain profile of the radiation pulse are related via a Fourier transform. Since an electron radiates uniformly in an undulator, the radiation packet has a square envelope. For the spectral intensity one can write

$$I(\omega) \propto \left| \int_0^{N_U \lambda / c} exp(-i(\omega - \omega_0)t)dt \right|^2 \propto \left(\frac{sin(2\pi N_U(\omega - \omega_0)/2\omega_0)}{2\pi N_U(\omega - \omega_0)/2\omega_0} \right)^2 \quad (1.12)$$

where $\omega_0 = 2\pi \dfrac{c}{\lambda}$ is the frequency corresponding to the central wavelength. The line shape function or the intensity spectral function of the spontaneous radiation is plotted in Fig. 1.2. It is convenient to characterize the spectrum with its whole width at half maximum (FWHM), which is

$$\frac{\Delta\omega}{\omega_0} \approx \frac{1}{N_U}, \quad (1.13)$$

and, as one can see, is defined by the undulator.

Speaking about the spontaneous radiation power, we have to take into account that in reality we always deal with an electron pulse consisting of a large number of electrons. All the electrons radiate in random phases if there is no correlation in the longitudinal electron beam distribution. For this reason the total intensity is the sum of the intensities from each electron. The power of spontaneous radiation is proportional to the number of electrons in the electron pulse that is to say to the electron beam current.

1.4   Stimulated emission

Stimulated emission was predicted by Einstein in 1917 and was one of the fundamental contributions to the creation of the laser. We consider an EM wave propagating in the undulator together with an electron. Now the electron will radiate not only in the undulator field but in the field of the EM wave as well. To make the system into a laser, we have to find a condition when the undulating electron is continuously giving its energy to the EM wave. In other words some portion of the kinetic energy of the electron has to be transferred to the EM radiation. There is a schematic of the interaction of the electron and the wave in the undulator in Fig. 1.3. The electron and the wave are propagating in the z direction. The undulator field forces the electron to oscillate in horizontal direction x, making $v_x \neq 0$. The EM wave is plane polarized so that its electric field lies in the (x, z) plane. In the situation pictured in Fig. 1.3 the electron interacts with the electric field of the EM wave so that the electron loses energy. In turn the EM wave gains energy, because of energy conservation in the system of the electron and wave. The wave always travels with the speed of light c. And the electrons propagate in the z direction with v_0, which is always less than c. For this reason the electron slips with respect to the wave. Hence, it will interact with the wave in its different phases.

When the electron slides in phase by π from the initial position it will gain energy by taking it from the wave. There is a phase range where the electron gives energy to the wave and there is a phase range where it takes the energy from the wave. This is why the overall energy exchange between the sliding electron and the wave, within the time when the electron passes the undulator is zero. Nevertheless, it is possible to

go around this problem. We can change the longitudinal velocity of the electron v_0 and, by means of this, control the slippage rate. Imagine we have chosen the electron energy γ and the undulator parameter K in such a way that electron slips exactly one period of the external EM wave while passing one period of the undulator. This can be expressed as

$$\lambda_W = c\tau - v_0\tau \tag{1.14}$$

where the λ_W is wavelength of the external wave and $\tau = \lambda_u / v_0$ is the time the electron needs to cover one period of the undulator.
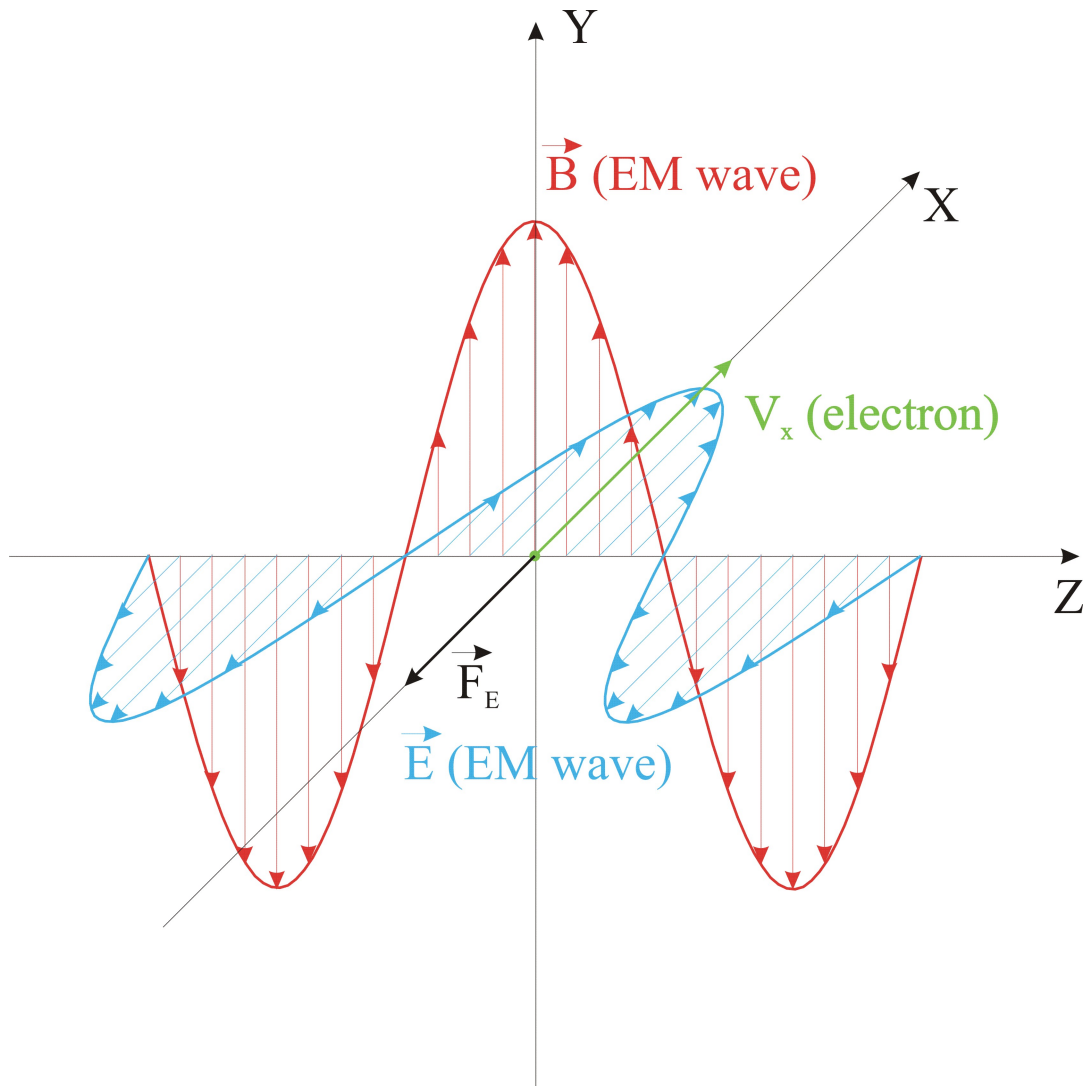
Figure 1.3 Interaction of the electron and the EM wave in the undulator

This situation is illustrated in Fig. 1.4. At the starting point, Fig. 1.4a, the electron is decelerated and its energy flows to the EM wave. One period of the undulator later, see Fig. 1.4c, the electron is in the same phase in respect to the EM wave and to the undulator, but one period back in the EM wave, which means it is giving its energy to the wave again. In the middle, between point (a) and (c), Fig. 1.4b, the electron velocity and electric field of the EM wave are flipped 180 degree with respect to their directions in points (a) and (c). Analysis of the forces acting on the electron at point

(b) shows that here the electron is giving its energy to the wave as well as in points (a) and (c). Intuitive it is clear such situation is kept everywhere between point (a) and (c). Condition (1.14) can be rewritten as follows

$$\lambda_W = \lambda_u \frac{1 - \beta_0}{\beta_0} \qquad (1.15)$$

which looks almost the same as Eq. 1.8 and is called the FEL resonant condition.
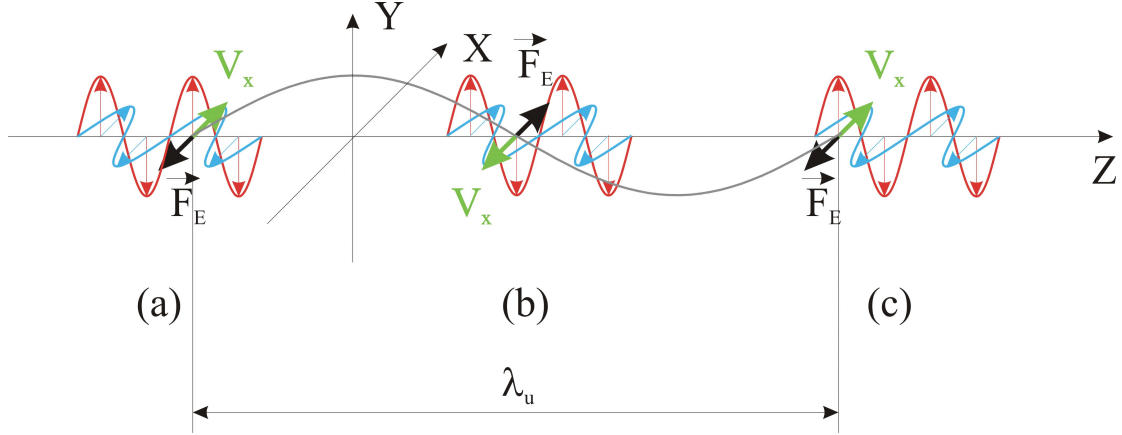
Figure 1.4 The FEL resonant condition

The resonant condition shows which wavelength the external EM wave must have to have net energy exchange with an electron of longitudinal velocity β_0 in an undulator with period λ_u. One can consider this process mathematically more strictly. The energy exchange between the electron and the electromagnetic wave is described by the equation

$$\dot{\gamma} = \frac{e(\vec{\beta} \cdot \vec{E})}{m \cdot c} \qquad (1.16)$$

where $\vec{E}$ is the electric field strength of the EM wave and $\vec{\beta}$ is the velocity of the electron. The electric field of the wave we consider has only one component $E_x = E_0 \sin(k_W z - \omega_W t)$. The electron velocity can be found from the Hamiltonian as was discussed in Section 1.2. The difference is that the vector potential is now a sum of the undulator vector potential and the wave vector potential, i.e. $\vec{A} = \vec{A}_u + \vec{A}_W$. Going through simple mathematics and requiring the phase of the right hand side of Eq. 1.16 to be constant, one gets the FEL resonant condition [1.1-1.3]

$$\lambda_W = \frac{\lambda_u}{2 \cdot \gamma^2}(1 + K^2_{RMS}) . \qquad (1.17)$$

As we see, to interact in a resonant way with the electrons the EM wave has to have a wavelength exactly the same as radiated spontaneously by the electron in the undulator. In some sense this is a decisive factor for an FEL operation. In the case of the FEL oscillator an optical resonator is built around the undulator to capture the radiation. An electron beam used to "pump" the FEL is pulsed with repetition rate f_0. The optical resonator length is chosen so that the light makes a round trip in the cavity with the period $1/nf_0$. Thus the radiation pulse from an electron bunch will meet the

next electron bunch at the entrance of the undulator and cause it to stimulate radiation in the undulator, i.e., it increases the energy of the radiation captured in the resonator.

Up to now we have considered stimulated radiation of one electron. As was already mentioned above an electron bunch consists of a very big number of electrons. If the longitudinal electron distribution in the bunch is uniform, then for each electron pumping energy into the radiation, there will be another electron, positioned at a distance $\lambda_W / 2$ from the first one, which will take from the radiation the same amount of energy. Hence, there will no net energy exchange between such a bunch and the EM wave. In terms of the quantum mechanics, stimulated emission is compensated for by stimulated adsorption. Fortunately, the interaction of the electron bunch with the external wave in the undulator leads to a modulation of the longitudinal velocity of the electrons and this in turn leads to a modulation of the longitudinal electron distribution. It is interesting that this happens even without a longitudinal force! We have $\dot{P}_Z = F_Z = 0$. This one can rewrite as $\gamma m \beta_Z = constant$. Thus these electrons, which gain the energy from the EM wave, lose longitudinal velocity β_Z and vice versa. Because of this the electrons tend to group with period of the radiation wavelength λ_W. This process is called microbunching. The microbunching and the way it influences the energy exchange between the electron beam and the radiation field will be discussed more in detail in the next sections.

The process of the microbunching as well as stimulated emission and resonant condition is an underlining principle of the FEL operation. The microbunching has two additional consequences, which we have to mention here. Since the electrons have the phase correlation the interference term is not zero anymore in the equation for the radiation power, which looks like

$$I \propto \left| \sum_{Ne} E_i \, exp(i \omega_W t_i \,) \right|^2 \propto N_e^{\,2} \tag{1.18}$$

where the sum is taken over the all electrons in the bunch and N_e is the number of electrons. Now the radiation power is proportional to $N_e^{\,2}$. As a reminder, in the case of spontaneous emission the power is proportional to N_e. For example, the maximum design bunch charge for the ELBE FEL is 77 pC. Such a bunch consists of 4.8×10^8 electrons and the ratio of the laser power and spontaneous undulator radiation power is about of 10^8! The next point to notice is that the microbunching also changes the radiation spectrum. The line width of the stimulated emission is $1/N_b$ where N_b is the ratio of the electron bunch length to the radiation wavelength, i.e., a number of the longitudinal beamlets in one bunch.

1.5 FEL gain

In the previous section we have discussed qualitatively the energy exchange between an electromagnetic wave and an electron propagating together in an undulator. The efficiency of this process is directly related to an important characteristic of an FEL called single pass gain. In this section we will outline a way to calculate the gain in the small-signal gain approximation. The definition of the single pass gain is intuitively comprehensible

$$G \equiv \frac{I_f - I_i}{I_i}, \qquad (1.19)$$

where I_i and I_f are respectively the radiation field intensity before and after an electron bunch passes the undulator. In the approximation the intensity change, is much smaller than the initial intensity of the field and, what is very important, the radiation field is far away from saturation. The field of the radiation, which is used to calculate the electron trajectory, is assumed to be constant. There is energy conservation in the system of the electron beam and the radiation field. This is why the radiation energy change is calculated as an energy change of the electron beam.

Let us have a look at the electron motion again, but in a little different way. The electron is moving in a periodic potential which is the result of the undulator field and the radiation field, as was mentioned in the previous section. The potential is called ponderomotive. It is possible to describe the motion of the electron in a specific phase space. One coordinate in this phase space is a phase of the electron in respect to the ponderomotive wave and is defined like

$$\theta = (k_u + k) \cdot z - k \cdot c \cdot t, \qquad (1.20)$$

where k_u and k are the wave numbers of the undulator field and the radiation field respectively and z is the longitudinal electron coordinate in the laboratory frame. The energy of the electrons that satisfies the FEL resonant condition (1.17) is called the resonant energy and is written as follows

$$\gamma_R = \sqrt{\frac{k \cdot (1 + K_{RMS}^2)}{2 \cdot k_u}} . \qquad (1.21)$$

Using the resonant energy one can define a dimensionless variable called detuning

$$\eta = \frac{\gamma - \gamma_R}{\gamma_R}, \qquad (1.22)$$

which is a measure of the electron energy. The detuning is the second coordinate in the phase space we will use to describe the electron motion. The following is assumed in the small-signal gain approximation: the electron beam quality is so good that we can neglect transverse electron motion before it enters the undulator, i.e., $P_{x0} = P_{y0} \approx 0$, the electrons are relativistic so that $\gamma >> 1$ and $\beta_z \approx 1$, but $\beta_x << 1$ and $\beta_y << 1$. In all equations we will keep terms to order $1/\gamma^2$, and the radiation field is smaller than the undulator field. We also will neglect the initial energy spread of the electrons. Starting from the Hamiltonian (1.1) and using the canonical equation together with equation (1.16), one can show that under the conditions mentioned above the electron motion in a planar undulator is described by the following differential equations

$$\dot\eta = -\Omega^2 \sin(\theta) \qquad \text{and} \qquad \dot\theta = 2ck_u\eta \qquad (1.23 \text{ a, b})$$

where $\Omega^2 = \frac{eE_R F_n(K)}{mc\gamma_R^2}$, E_R is the radiation electric field and the $F_n(K)$ is a factor responsible for harmonics generation, which is about unity for the fundamental frequency [1.1,1.3]. The Eqs. (1.23) can be obtained from a simplified Hamiltonian, written like

$$H(\eta,\theta) = c \cdot k_u \cdot \eta^2 - \Omega^2 \cdot \cos(\theta). \qquad (1.24)$$

It is easy to see that the equations (1.23) are just the canonical equations $\dot{\theta} = \dfrac{\partial H}{\partial \eta}$ and $\dot{\eta} = -\dfrac{\partial H}{\partial \theta}$ for the Hamiltonian (1.24). The phase space (θ, η) is plotted in Fig. 1.5.
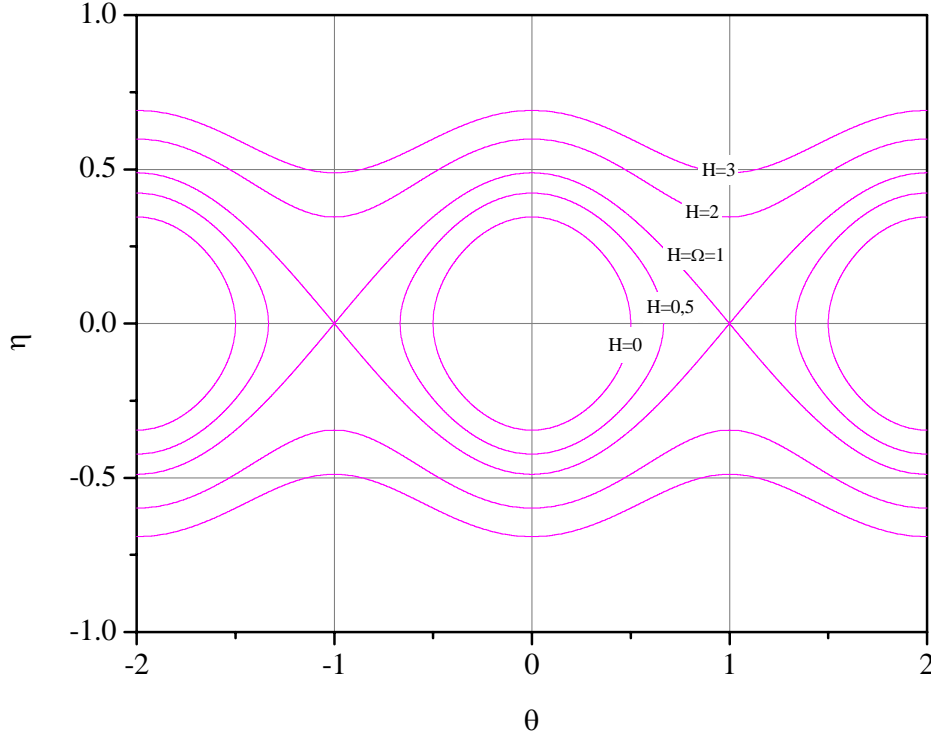
Figure 1.5 Phase space(θ, η) with H=constant surfaces

   Electrons move along surfaces, which correspond to a constant value of the Hamiltonian, since the Hamiltonian is a constant of motion. There are two different types of electron trajectories. The first one is closed so that the electron is oscillating always in one bucket of the ponderomotive wave, and the second type is open, electrons on such an H-surface travel from one bucket to another. If an electron moves up in the (θ, η) phase space then its energy is growing and radiation field is losing energy. In the opposite of this situation, if an electron moves down in the (θ, η) phase space it is giving its energy to the radiation field. Note that the phase space is symmetric in respect to η inversion. Assume all electrons injected into the undulator have the same energy, i.e., the same value of detuning. Hence, they are located along a line $\eta = constant$ in the beginning of their evolution in the phase space. As long as the electron bunch has uniform longitudinal distribution, the electrons are distributed uniformly in phase θ as well. Imagine that the electrons injected into the undulator have resonant energy γ_R. Because of phase space symmetry and the initial uniform distributions of the electrons, the electron distribution will keep its symmetry in respect to $\eta = 0$, see Fig. 1.6b. That means average energy exchange between the electron beam of energy γ_R and the radiation is zero. Obviously, in this case the FEL

gain is also zero. It can be seen in the Fig. 1.6b that the electrons of the beam will group around phase $\pm 2\pi n$, where n in integer. This is the microbunching which was already mentioned in the previous section. To make the gain positive an initial energy has to be chosen so that the microbunching occurs around a phase where the electrons are giving energy to the radiation field. To do so we have to take an electron beam with energy more than the resonant one, i.e., with positive value of η. Such a situation is pictured in Fig. 1.6c. Then the electrons moving down in the (θ, η) space change their energy more than the electrons moving up. And as one can see the micro bunching occurs in the phase range $\pm 2\pi n < \theta < \pi \pm 2\pi n$. Again, because of the phase space symmetry, the situation will be opposite for negative values of the detuning Fig. 1.6a. The microbunching will take place in the phase range $-\pi \pm 2\pi n < \theta < \pm 2\pi n$ where the electrons are gaining energy by taking it from the radiation. Hence for an electron beam with negative detuning the FEL gain has to be negative. From this consideration we can conclude now that the gain is an antisymmetric function of the detuning. To calculate the gain mathematically rigorously one has to solve Eq. (1.23) so information about energy and the phase in respect to the ponderomotive potential will be obtained for electrons as a function of time and their initial energy and phase. Doing this we should remember that we are interested in an average energy change of the electron beam, i.e., $<\Delta\eta>$. Applying perturbation theory to Eq. (1.23) one can show that

$$<\Delta\eta> \propto f(x) = \frac{d}{d(x/2)}\left(\frac{sin(x/2)}{(x/2)}\right)^2 \qquad (1.25)$$

where $x = 4\pi N_u(\gamma - \gamma_R)/\gamma_R$ [1.1-1.3]. The function (1.25) is plotted in Fig. 1.7. The function is an antisymmetric function of the energy as was discussed just before. The radiation intensity change can be calculated as following $\Delta I = -mc^2\gamma_R <\Delta\eta> N_e$ [1.1-1.3]. Substituting this into the gain definition formula (1.19) we will find an expression for the single pass gain in the form [1.1-1.3]

$$G = 4\sqrt{2}\pi^2\lambda^{3/2}\lambda_U^{1/2}\frac{K_{RMS}^2}{(1+K_{RMS}^2)^{3/2}}\frac{I_p}{I_A}\frac{N_U^3}{S}f(x) \qquad (1.26)$$

where I_p is a beam peak current, $I_A = ec/r_e$ is so-called Alfen current, which is about of 17 kA for an electron beam, and S is the transverse cross section of the radiation field, r_e is the classical radius of the electron. The gain calculated using this formula has to be less than unity, otherwise the above assumptions are violated. To estimate an order of magnitude of the gain we assume that the cross section of the radiation field in the undulator is diffraction limited. In this case $r_0 \cdot \alpha \approx \lambda$ where r_0 is the characteristic transverse size of the field and α is its angular divergence. If we want to have the field in the undulator within certain radius r_0 then divergence should be $\alpha = r_0/N_U\lambda_U$. Using this we substitute in (1.26) the cross section of the radiation field with $\pi\lambda\lambda_U N_U$. We also always chose all parameters so that we are in the maximum of the $f(x)$, which is described in Eq. (1.25). The function equals 0.54 in its maximum. Under this conditions the gain formula is rewritten like [1.1-1.3]

$$G \approx 4\sqrt{2}\pi\sqrt{\frac{\lambda}{\lambda_U}}\frac{K_{RMS}^2}{(1+K_{RMS}^2)^{3/2}}\frac{I_p}{I_A}N_U^2 0.54 . \qquad (1.27)$$
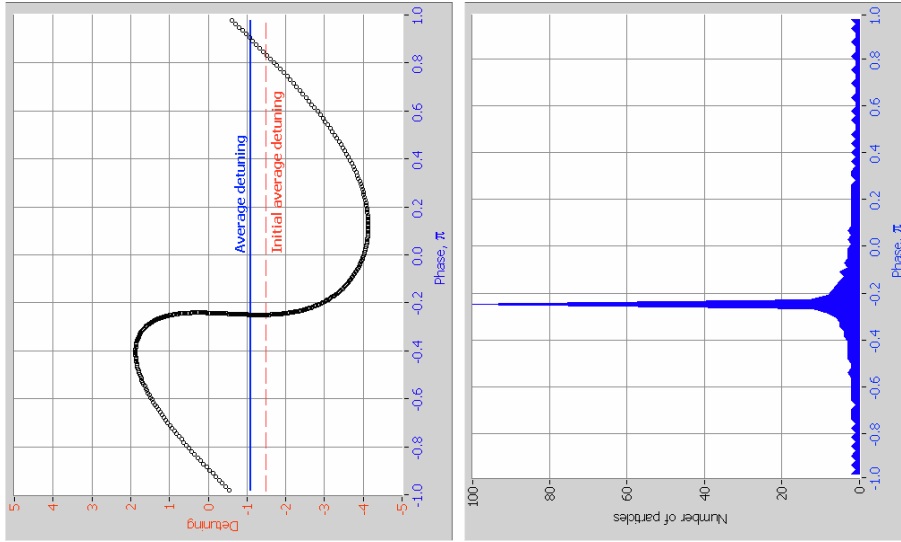
(a) *initial detuning -1,5; gain negative*
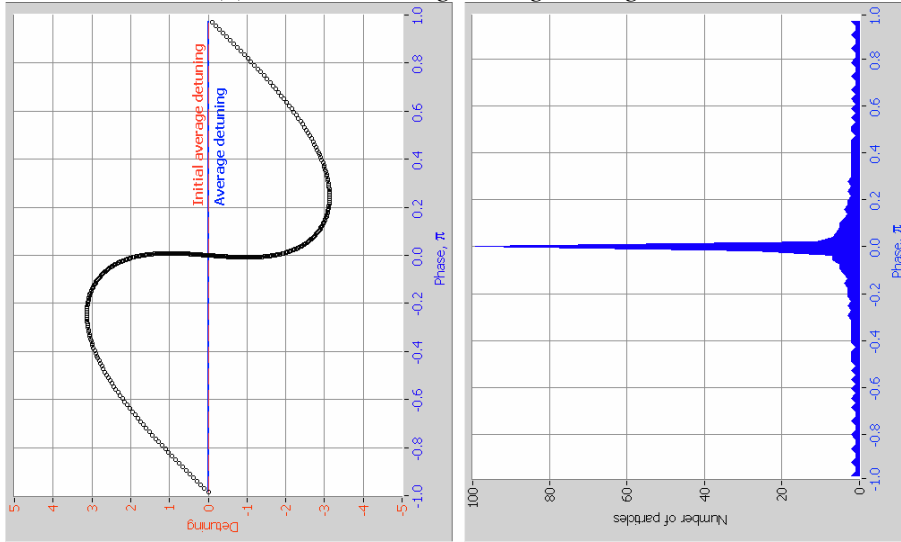
(b) *initial detuning 0; gain 0*
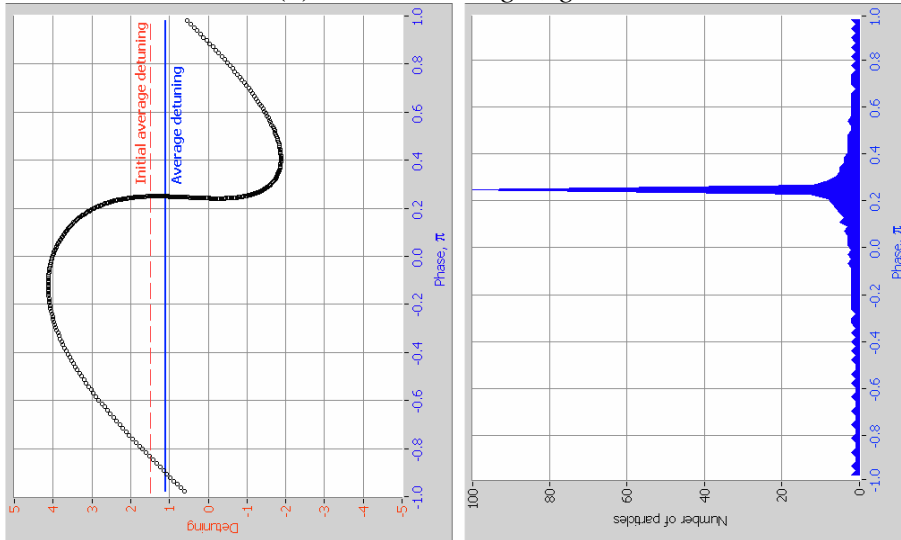
(c) *initial detuning 1,5; gain positive*

Figure 1.6 Microbunching at different initial detunings
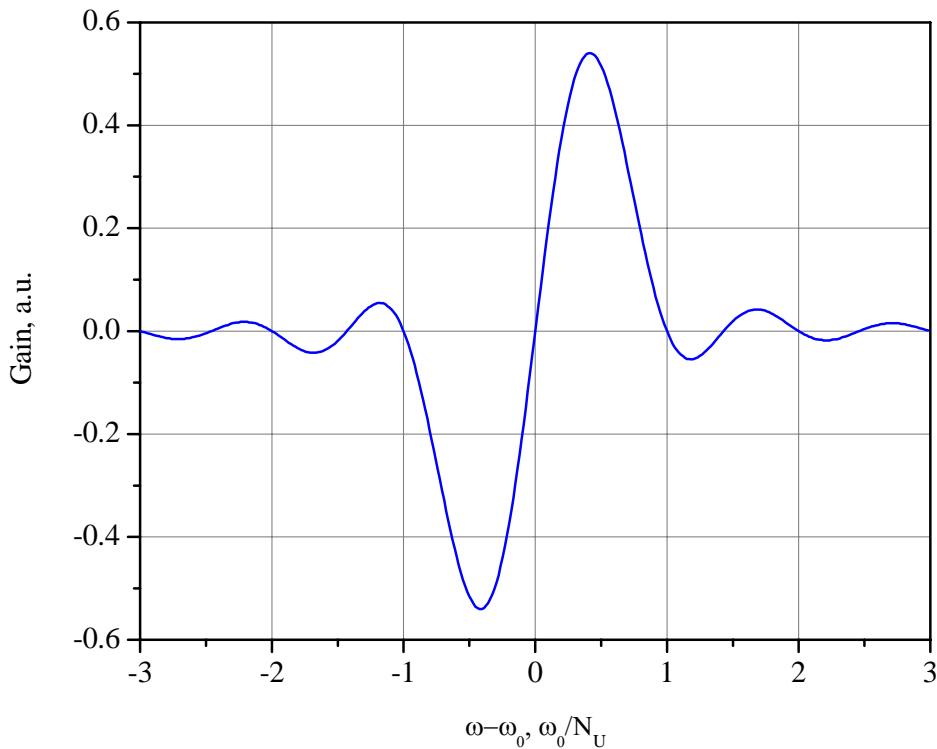
Figure 1.7 The shape of the FEL gain function

One should note here that the gain goes down for a smaller wavelength. Another important fact is that the gain is proportional to the beam peak current. In practice the gain is about several tenths of percent per one ampere of the peak current. Obviously, an FEL oscillator works if the gain of the field is larger that the field losses in the optical resonator. To make the FEL work the gain has to be at least several percent; that means a peak current of several tens of amperes is required. Another very interesting and fundamental fact is that the gain is proportional to the first derivative of the spectral intensity of spontaneous radiation. This statement is Madey's first theorem. Another fundamental FEL property is that the gain leads to energy spread of the electron beam. This is Madey's second, so-called gain-spread, theorem [1.4]. Due to the effect of the electron beam quality the FEL gain in practice is smaller as the one described by the Eq. (1.27). In the next section we discuss the gain reduction and the electron beam parameters which are critical for an FEL operation.

1.6 Electron beam quality requirements

Considering the FEL operation in all previous sections we have assumed that the electron beam used to drive the FEL is ideal. We have assumed that all electrons of the beam have the same energy and enter the undulator exactly on its axis. That means the electron beam has zero diameter. We also did not take into account that the electrons' trajectories have angular spread. Here we will consider an influence of the real beam quality on the FEL operation, and discuss the beam quality requirements which the FEL impose to the electron beam.

If an electron propagating in the undulator has an energy a bit different from the resonant one it tends to radiate at different wavelength. Since the magnetic field in the undulator is not homogeneous an electron traveling off axis in the undulator experiences slightly different magnetic field. In other words it sees another undulator parameter K. Obviously, variation of the entrance angle of the electron in the undulator leads to a wavelength variation, since this influences the electron trajectory. As was mentioned above the line width of the spontaneous radiation is inversely proportional to the number of undulator periods $\Delta\lambda/\lambda = 1/N_U$. If a change in the electron parameters is so big that the electron radiates at wavelength out of the spontaneous radiation bandwidth then this radiation is not amplified in the process of stimulated emission. Such electrons do not participate in the gain process. Increasing the number of such electrons decreases the FEL gain. If the number is big enough the gain is less than the losses and the FEL does not work. The main criteria in the consideration of the influence of beam quality to FEL gain is that the electron parameters change may modify the radiation wavelength for less than the natural bandwidth of the spontaneous radiation. Using Eq. (1.11) we can link the wavelength variation to the beam parameters variations like

$$\frac{\Delta\lambda}{\lambda} = \frac{2\Delta\gamma}{\gamma} + \frac{2K_{RMS}\cdot\Delta K_{RMS}}{1+K_{RMS}^2} + \frac{\gamma^2\cdot 2\theta\cdot\Delta\theta}{1+K_{RMS}^2} \qquad (1.28)$$

where $\Delta\theta$ now is the characteristic electron beam angular divergence. We require every term of the right hand side of the Eq. (1.28) to be less than $1/2N_U$. The first term is related to the energy spread of the electron beam. Considering the ELBE undulator with 64 periods we estimate required energy spread $\Delta\gamma/\gamma$ to be less then 0.4 %. The second term in the Eq. (1.28) is related to both the undulator quality and the beam diameter as was discussed before. We suppose that effects of the undulator imperfection itself is much smaller that the effect of the finite beam radius. One can show that in the case when the beam diameter r_b is much less than the undulator period λ_u the condition $\frac{2K_{RMS}\cdot\Delta K_{RMS}}{(1+K_{RMS}^2)} < \frac{1}{2N_U}$ can be rewritten as following [1.1]

$$r_b < \sqrt{\frac{1+K_{RMS}^2}{N_U k_U^2 K_{RMS}^2}}. \qquad (1.29)$$

The term in Eq. (1.28) imposing the limit to the beam angular divergence can be written as $\Delta\theta < \sqrt{\lambda/(\lambda_U N_U)}$. The angular divergence and the beam transverse size are not independent from each other. A concept of transverse beam emittance will be described in the next chapter. There we will see that there is one more motion invariant called emittance. A very simple definition of the transverse emittance is the product of the beam divergence and the beam radius in the beam waist, i.e., $\varepsilon = r_b\Delta\theta$. Now we can combine the requirements for the beam divergence and the Eq. (1.29) together in the following form

$$\varepsilon < \sqrt{\frac{1+K_{RMS}^2}{N_U k_U^2 K_{RMS}^2}}\cdot\sqrt{\frac{\lambda}{\lambda_U N_U}}. \qquad (1.30)$$

An electron beam in the undulator executes betatron oscillations as was mentioned in Section 1.2. The best condition for the electron beam transport in the undulator is

when $\lambda_\beta = \lambda_u N_U$ [1.1]. Using this fact we rewrite the Eq. (1.30) in a very convenient form for the FEL requirements to an electron beam emittance

$$\varepsilon < \frac{\lambda}{2\pi}. \qquad (1.31)$$

This requirement is very strict. To produce a radiation at desirable wavelength one must provide an electron beam with geometrical emittance less then $\lambda/2\pi$. It is convenient to use a normalized emittance to describe the electron beam quality. The normalized emittance is an invariant of the motion even when the electrons are changing their energy. The normalized emittance is related to the geometrical one like $\varepsilon_n = \gamma\beta \cdot \varepsilon$. As an example, if the ELBE FEL is supposed to operate at wavelength of 5 μm with electron beam energy of 30 MeV then the normalized emittance of the beam must be smaller than 55 mm×mrad.

As was mentioned in the previous section the beam peak current is very important for an FEL operation. This is why the electron bunch length measurement is a very important item for the beam diagnostics at an FEL. One more reason for that is the slippage of the electron beam with respect to the optical pulse in the undulator during their interaction. Electrons and the light have different velocity. This reduces their longitudinal overlap in the undulator, consequently the FEL gain is also reduced.

Calculating the FEL gain we have supposed that there is a transverse overlap of the electron beam and the optical field. Of course such condition is not accomplished automatically in an FEL. This is why one has to pay special attention to the electron beam position diagnostics in the undulator. The position of the optical field is defined by position and configuration of the optical resonator and can be adjusted by the resonator mirrors. Diagnostics used to ensure the transverse overlap of the electron beam and the optical field are very important for operation of any FEL oscillator.

The influence of such electron beam parameters like transverse emittance, energy spread and bunch length is calculated rigorously in the work of Dattoli et al. [1.5]. In the work the influence is described in terms of dimensionless factors, which reduce the FEL gain. Here we only outline some results of the work. The gain is reduced because of the energy spread by a factor $f_E = \dfrac{1}{(1+1.7(4N_U \cdot \sigma_E)^2)}$ where σ_E is the relative energy spread. To estimate the order of magnitude of the factor we suppose the energy spread to be 0.4 % if the undulator has 64 periods then the f_E is about 0.34. Finite transverse emittance reduces the gain by a factor $f_\varepsilon = \dfrac{1}{1+\mu_x^2} \cdot \dfrac{1}{1+\mu_y^2}$

where $\mu_x = \sqrt{2}\pi \dfrac{N_U \varepsilon_n}{\lambda_U} \dfrac{K_{RMS}}{1+K_{RMS}^2}$ and $\mu_y = 2\pi \dfrac{N_U \varepsilon_n}{\lambda_U} \dfrac{K_{RMS}}{1+K_{RMS}^2}$. For a normalized emittance of 10 mm×mrad and the undulator parameter $K=0.8$ the reduction factor is 0.99 i.e. almost negligible. The gain reduction related to bunch length σ_z is expressed by a factor $f_z = \dfrac{1}{(1+(N_U \lambda / 3\sigma_z))}$ that is about 0.85 for 2 ps bunch length and 5 μm radiation wavelength.

Let us estimate the small signal gain for the ELBE FEL. The design parameters of the ELBE FEL are the following. The undulator has a period of 27 mm and the number of periods is 64. An electron beam with an energy from 12 MeV up to 40

MeV will be available. The undulator parameter K_{RMS} can be changed from 0.3 up to 0.8. For the estimate we use the maximum bunch charge, which is 77 pC. One has to know the bunch length to calculate the peak current. The bunch length at ELBE is in the picosecond range. Assume the bunch length to be 2 ps. The gain calculated for the ELBE parameters is plotted in the Fig. 1.8. There are two sorts of curves one corresponds to a constant electron beam energy and variation of the undulator parameter from 0.3 up to 0.8. Another sort of the curves corresponds to a constant undulator parameter with electron beam energy variation from 12 MeV to 40 MeV. The calculated gain is only a simple estimation. Rudi Wünsch did more detailed gain calculations for the ELBE FEL [1.6].
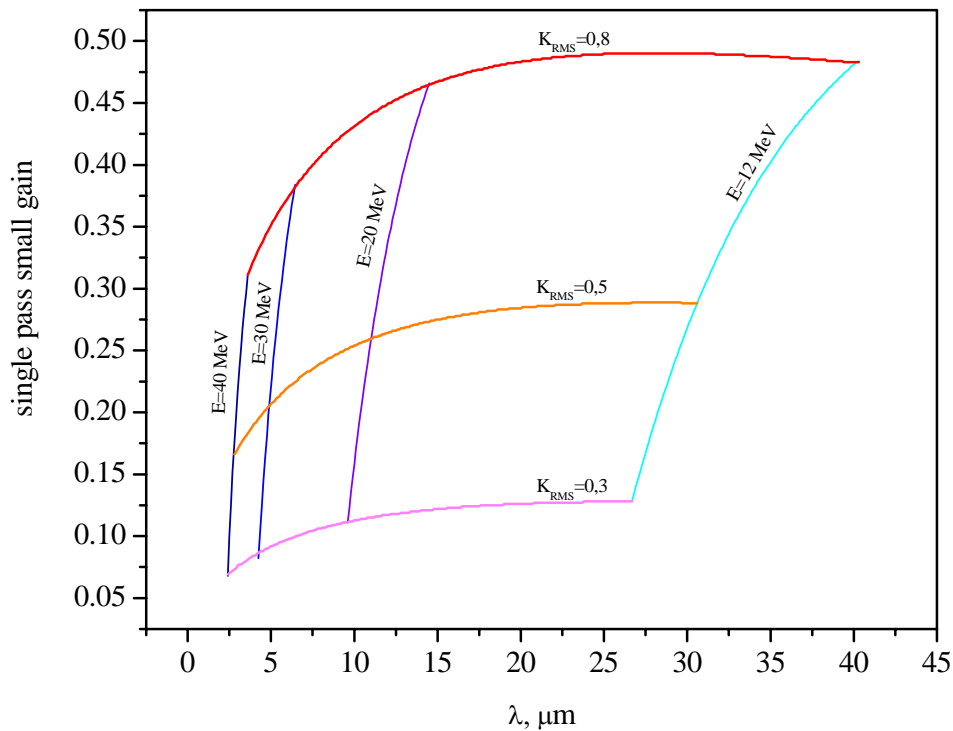
Figure 1.8 The ELBE FEL small-signal single pass gain

1.7 Conclusion

In this chapter we have considered such fundamental processes of FEL operation as stimulated emission and microbunching. The gain of the ELBE FEL was estimated in the small signal gain approximation. The importance of the electron beam quality for an FEL operation was discussed. At the end of the chapter we have laid down the requirements imposed by an FEL on the electron beam parameters.

Chapter 2

Transverse emittance

2.1   Introduction

The quantity transverse emittance was already mentioned in the previous chapter. Here we will discuss in detail the concept of transverse emittance and its importance. We will start from a short overview of linear beam dynamics, when space charge effects are negligible. Then we will take into account the influence of space charge on the beam dynamics. In general, the beam transport is influenced by external fields applied to focus and steer the beam, and by the electromagnetic field of the beam itself. There are two limiting cases. In the first one the field of the beam is negligible and the beam transport is emittance dominated. In the situation when the bunch field is significant the beam is called space charge dominated. One must take this into account in choosing a method to measure emittance. We will describe two methods used to measure the transverse emittance at ELBE. The multi-slit method was used to measure the transverse emittance in the ELBE injector and the quadrupole scan method to measure the emittance of the accelerated beam downstream of the accelerating module. The measurement setups are described. Results of the measurement as well as the measurement errors are presented and discussed.

2.2   Phase space and emittance

To completely define the position of a particle in space and its evolution one has to define six variables namely three coordinates $x(t)$, $y(t)$, $z(t)$ and three components of the particle momentum $p_x(t)$, $p_y(t)$ and $p_z(t)$. In other words, the motion of a particle is described in a six-dimensional space, which is conventionally called phase space. Any beam is composed of a very large number of particles, and we are interested in the collective behavior of the particles but not in a single particle evolution. In the six-dimensional phase space a distribution function

$f(x,y,z,p_x,p_y,p_z)$ is introduced to describe the local density of the beam particles. The number of particles in an elementary volume of the phase space is $dN = f(x,y,z,p_x,p_y,p_z)dxdydzdp_xdp_ydp_z$. The distribution function is normalized in a way that the integral over the entire phase space gives the number of particles in the beam:

$$N_b = \int\int\int\int\int\int f(x,y,z,p_x,p_y,p_z)dxdydzdp_xdp_ydp_z . \qquad (2.1)$$

Emittance in general is defined as a volume of the phase space occupied by the beam, which can be written like

$$\varepsilon_{(6)} = \int\int\int\int\int\int_{beam} dxdydzdp_xdp_ydp_z . \qquad (2.2)$$

The quantity $\varepsilon_{(6)}$ is also called six-dimensional hyper-emittance.
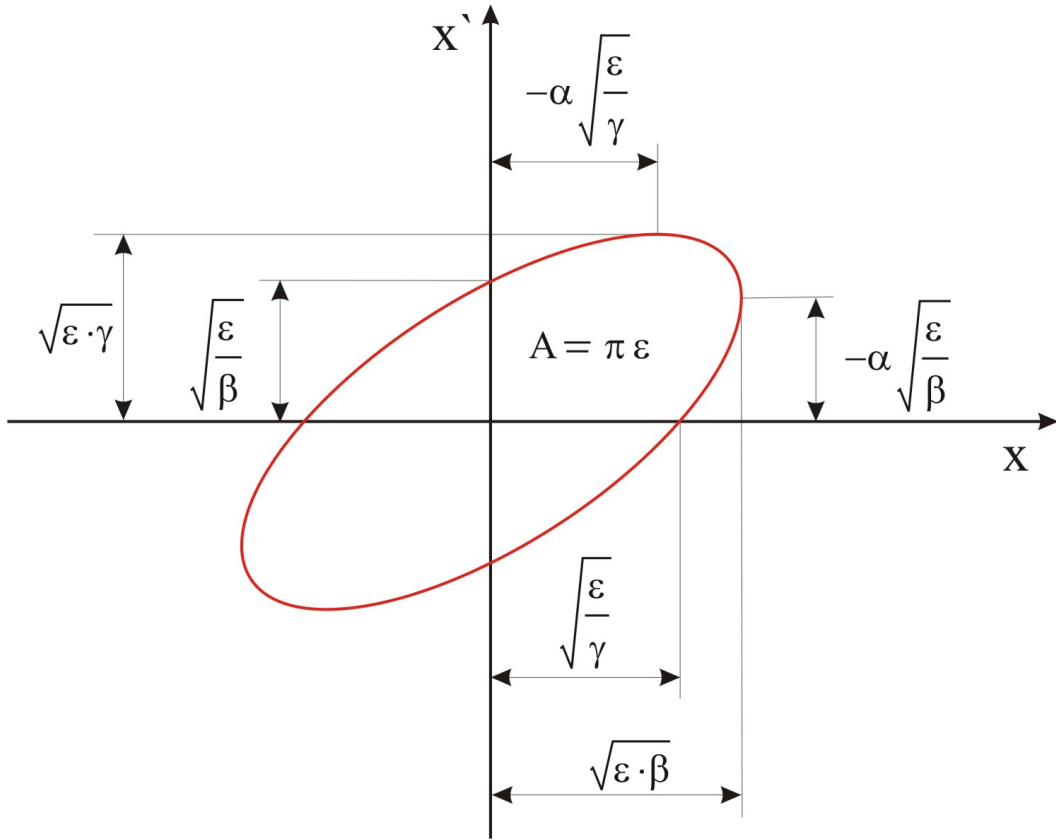
Figure 2.1 Phase space ellipse and its relation to the Twiss parameters

A significant simplification is possible when motion is independent in different degrees of freedom. In this case the distribution function is a product of two-dimensional distribution functions, which is written as following $f(x,y,z,p_x,p_y,p_z) = f_x(x,p_x)f_y(y,p_y)f_z(z,p_z)$. In such a case one can reduce the consideration to three independent two-dimensional phase spaces as follows (x,p_x), (y,p_y) and (z,p_z). Obviously a particle beam is associated with a preferable direction of propagation. Like the previous chapter we set z as the beam propagation direction. Thus (x,p_x) and (y,p_y) are two independent transverse phase spaces. The 6-D phase space can be projected onto the (x,p_x) plane. In this chapter we will consider only the (x,p_x) plane, the same formalism is valid for the (y,p_y) phase

space. Variables x and p_x were chosen since they are canonically conjugated as is required by the Hamiltonian formalism. Nevertheless it is more practical to use a normalized transverse momentum $x' = p_x/p_z$ instead of the momentum component p_x. The x' is also the divergence or an angle of the particle with respect to the reference particle trajectory. Emittance is a simultaneous measure of the beam size and divergence as we have mentioned in Chapter 1. In the (x,x') plane a point again represents every particle of the beam. As analogous to Eq. (2.2) a two-dimensional transverse emittance is defined as an area occupied by the beam in the (x,x') plane. This is a general definition of transverse emittance. There are several possibilities for defining emittance more practically. One convenient way is to choose an ellipse in the phase space so that it contains a certain fraction of the particles, for instance 90%, and has minimal possible area. In this case emittance is defined as the ellipse area divided by π, see Fig. 2.1 for illustration. There are several good reasons to use an ellipse in describing the transverse phase space. One of them is that an ellipse is transformed into an ellipse under canonical transformations. The canonical transformation is used in linear beam transport formalism, as we will see later. Another reason to use the ellipse to describe the entire beam is that the trajectory of a single particle on the phase plane is very often ellipse as well. Any ellipse can be described by a bilinear form

$$\gamma_T \cdot x^2 + 2\alpha_T \cdot xx' + \beta_T \cdot x'^2 = \varepsilon . \qquad (2.3)$$

The parameters α_T, β_T and γ_T are called Twiss parameters or Courant-Snyder parameters. There are only three independent parameters in Eq. (2.3) since there is a correlation between the Twiss parameters:

$$\beta_T \cdot \gamma_T - \alpha_T^2 = 1 , \qquad (2.4)$$

which is just the geometrical property of an ellipse. The area of the ellipse is equal

$$A = \iint\limits_{ellipse} dxdx' = \pi\varepsilon , \qquad (2.5)$$

where ε is the transverse beam emittance. The emittance definition using the phase space ellipse is very simple and it is also very useful for the first order beam transport. However such a definition suffers obviously from arbitrariness of the phase space contour, since a real particle distribution in general is not elliptical and can be rather complicated.

Statistical approach is another way to define the transverse emittance. To characterize the beam size very often the root-mean-square (RMS) beam size is used. The RMS beam size is the square root of the second order momentum of the distribution function $f(x,x')$

$$\sigma_X^2 = \left\langle x^2 \right\rangle = \frac{1}{N_b} \int x^2 f(x,x')dx . \qquad (2.6)$$

An RMS beam divergence is introduced in a similar way and can be written as follows:

$$\sigma_{X'}^2 = \left\langle x'^2 \right\rangle = \frac{1}{N_b} \int x'^2 f(x,x')dx' . \qquad (2.7)$$

The transverse emittance is a measure of the particle spread in the phase space and is analogous to the RMS beam size but only in two-dimensional space. Thus one can introduce an RMS emittance. As far as the transverse emittance is a measure of both the beam size and the beam angular divergence the RMS emittance should be a

composition of second order moments of the distribution function $f(x, x')$. Since the position of the beam in the phase plane does not change the phase volume or emittance, we are free to choose the coordinate system so that $\langle x \rangle$ and $\langle x' \rangle$ equal zero. As the next action we can rotate the coordinate system in the phase space, which also does not change particle distributions and emittance. By this rotation we can find a coordinate system in with σ_X^2 and $\sigma_{X'}^2$ reach their minimums. In this new coordinate system the transverse emittance is just a product of RMS beam size and RMS divergence. Then going though simple mathematics one can show that in our original or laboratory coordinate system the root-mean-square emittance is [2.1]:

$$\varepsilon_{RMS} = \sqrt{\langle x^2 \rangle \langle x'^2 \rangle - \langle x \cdot x' \rangle^2} \ . \tag{2.8}$$

Such an emittance definition has no link to any contour in the transverse phase space. Since different definitions do not change the nature of the thing it is possible to express the Twiss parameters in terms of the second order momentum

$$\beta_T = \frac{\langle x^2 \rangle}{\varepsilon}, \ a_T = -\frac{\langle x \cdot x' \rangle}{\varepsilon}, \ \gamma_T = \frac{\langle x'^2 \rangle}{\varepsilon} \ . \tag{2.9 a, b, c}$$

Using RMS beam size and the RMS beam divergence, defined in Eqs. (2.6) and (2.7) and introducing a correlation coefficient as $r = \dfrac{\langle x \cdot x' \rangle}{\sqrt{\langle x^2 \rangle \langle x'^2 \rangle}}$, emittance can be also expressed like in the following form:

$$\varepsilon_{RMS} = \sigma_X \sigma_{X'} \sqrt{1 - r^2} \ . \tag{2.10}$$

In different sources one can meet different definition of emittance, here we want to mention only one of them, which is defined like

$$\varepsilon_{eff} = 4\varepsilon_{RMS} = 4\sigma_X \sigma_{X'} \sqrt{1 - r^2} \tag{2.11}$$

and called effective emittance. The emittance defined above in different ways is always called geometrical or un-normalized emittance. If an electron beam is accelerated the longitudinal component of the momentum becomes bigger and transverse components remain the same. This is why beam divergence gets smaller. That means the geometrical emittance becomes smaller as well. To have a value independent of the beam energy a normalized emittance is introduced. The normalized emittance equals

$$\varepsilon_{RMS}^n = \beta \cdot \gamma \cdot \varepsilon_{RMS}, \tag{2.12}$$

where γ is the relativistic Lorentz factor and β is the normalized particle velocity i.e. $\beta = v/c$, here c is the speed of light in vacuum.

A fundamental and important property of the beam dynamics in phase space is stated by Liouville's theorem [2.2]. The statement is that in a Hamiltonian system the area of phase space occupied by a set of beam particles, and the particles density in the phase space in vicinity of any particle are constants of motion. In other words the particles in the phase space behave like an uncompressible fluid. This can be expressed in the following way

$$\frac{d}{dt} f(\vec{r}, \vec{p}) = 0, \tag{2.13}$$

here $f(\vec{r}, \vec{p})$ is the distribution function introduced in the beginning of this chapter. The direct consequence of Liouville's theorem applied to the transverse phase space is emittance conservation in any Hamiltonian system, i.e., in a system without

dissipation. We also want to note here that there are several processes whose presence makes a particle beam a non-Hamiltonian system, leading to an increase of emittance in an accelerator. Most important of them are: interaction of the beam particles with the Coulomb field of the bunch, radiation by the beam particles, interaction of the beam with its radiation, interaction with high order mode fields in the accelerator structure, and interaction with wake fields.

2.3   Beam transport in linear approximation

To transport an electron beam from the electron source to the accelerator and later to the place where it is used for experiments an external electrical and magnetic field can be applied. To describe the motion of the beam particle one could solve the equation of motion, for instance numerically, for every particle. Since a beam of interest consists of a huge number of particles such an approach to the beam transport calculations is impractical and would take too much of computation time. To overcome this problem an alternative formalism was developed by Twiss and Frank [2.3]. This approach is called *Matrix Formalism* and is based on both the Liouville's theorem and on linear particle dynamics. In general, a particle is represented by the six-component vector X:

$$X = \begin{pmatrix} x \\ x' \\ y \\ y' \\ l \\ \delta \end{pmatrix}, \tag{2.14}$$

where instead of canonical variables z and p_z new variables l and δ are used. Here l is the particle distance in the direction of beam propagation from the reference particle and δ is the particle momentum deviation $\delta = \Delta p / p_0$, p_0 is the reference or design momentum. On its way through the accelerator the particle passes focusing elements like solenoids and quadrupoles, bending magnets and, if necessary, high-order elements like sextupoles and octupoles. Certainly the magnetic elements are separated by drift spaces. Every element of a beamline is represented by a 6×6 matrix, which is usually referred as R matrix. Suppose a particle upstream of some beamline element is represented by X_0 then a new vector X_1 represents the same particle past the element, the new vector representing the particle equals

$$X_1 = R \cdot X_0. \tag{2.15}$$

Consider now a sequence of n elements. Each of these elements has its matrix R_i. A single matrix R_t then describes the entire sequence. The R_t is a product of all matrixes of the sequence:

$$R_t = R_n \ldots R_3 \cdot R_2 \cdot R_1 \tag{2.16}$$

Here R_1 is the matrix of the first element passed by the particle and R_n represents last elements of the sequence. Thus, the position of the particle in the phase space can be found for any place along the accelerator if the initial position of the particle and the R matrix is known. In fact an equation such as 2.15 is nothing but a matrix form of a linear differential equations system. The theory of differential equations [2.4]

provides us with some important statements. One of them is that there is only one solution for a set of initial conditions; in our case the initial condition is a position of the particle in the phase space X_0. That means two traces of two particles started from different positions will never cross each other. Now we return to the case of uncoupled motion in independent degrees of freedom. We consider the two-dimensional transverse phase space (x, x'). The vector describing the particle is two-dimensional as well:

$$X = \begin{pmatrix} x \\ x' \end{pmatrix},$$ (2.17)

and the transport matrix R is a square 2×2 matrix. It is easy to see that the ellipse Eq. (2.3) can be written in a matrix form as follows

$$X^T \sigma^{-1} X = 1,$$ (2.18)

where the beam matrix or the σ matrix is defined as:

$$\sigma = \begin{pmatrix} \sigma_{11} & \sigma_{12} \\ \sigma_{21} & \sigma_{22} \end{pmatrix} = \varepsilon \begin{pmatrix} \beta_T & -\alpha_T \\ -\alpha_T & \gamma_T \end{pmatrix}.$$ (2.19)

The beam matrix contains all information about the phase space ellipse. Eq. (2.18) as well as the phase space ellipse is defined for any point along the beamline. One just has to take vector X and beam matrix σ corresponding to the point on the beam line. Thus in the beginning of the beam line the matrix form is $X_0^T \sigma_0^{-1} X_0 = 1$. Expressing X_0 in the last equation in terms of X_1 and making some basic matrix transformations one ends with

$$X_1^T (R \sigma^0 R^T)^{-1} X_1 = 1.$$ (2.20)

Since Eq. (2.20) has to have the form of Eq. (2.18) we can conclude that the beam matrix σ is transformed from one point of the beam line to another one with the help of the same transport matrix R as well as for a single particle

$$\sigma^1 = R \sigma^0 R^T.$$ (2.21)

Certainly this result is valid not only for the two-dimensional phase space but for the general six-dimensional phase space, too. Equation (2.21) is of great importance for the emittance measurements. As one can easily see from the σ matrix Eq. (2.19), the emittance can be expressed in terms of the matrix elements as follows

$$\varepsilon = \sqrt{det(\sigma)}.$$ (2.22)

That means if we can determine the elements of the σ matrix at some point of the beamline we will know the beam emittance.

To ensure that there is no significant emittance increase in the ELBE accelerator and for better understanding of the machine, several emittance measurements have been done. First, the transverse emittance is measured in the injector, where the beam is space charge dominated. This is why the multi-slit method was used as described in Section 2.6. Downstream in the accelerator, because the electrons are relativistic, the influence of the space charge force is strongly suppressed. The beam is emittance dominated and the quadrupole scan method is used to measure emittance as explained in Section 2.4. In the rest of this chapter we will describe experimental methods and present results of the measurements and analysis of measurements errors.

2.4 Quadrupole scan emittance measurements

There are several methods of emittance measurements based on the linear beam transport formalism. Here we will describe only one of them which is used at ELBE. This is the quadrupole scan method.

Let us consider a section of a beam line consisting sequentially of a quadrupole lens, a drift space and a view screen which is used for beam transverse profile measurements. From the σ matrix definition and the Eq. (2.9a) we have $r_{rms}^2 = \langle x^2 \rangle = \varepsilon \beta_T = \sigma_{11}$, which means that the RMS beam size measurements are measurements of the beam matrix element σ_{11}. Let σ^0 be the beam matrix in front of the quadrupole and σ^1 is the beam matrix at the position of the view screen. From Eq. (2.21) we have

$$\sigma_{11}^1 = R_{11}^2 \sigma_{11}^0 + 2 R_{12} R_{11} \sigma_{12}^0 + R_{12}^2 \sigma_{22}^0, \tag{2.23}$$

where R_{11}, R_{12}, R_{22} are the elements of the transport matrix, which is a product of the matrix of the quadrupole and the drift space matrix. The elements σ_{11}^0, σ_{12}^0 and σ_{22}^0 are constants and our goal is to determine them. In the experiment the beam profile is measured with the help of the view screen at different quadrupole settings, more exactly as a function of the quadrupole current I. Measured RMS beam size is a function of the quadrupole current $r_{rms}^2{}_i = \sigma_{11}^1(I_i)$, i is the measurements index. The transport matrix is a function of the current as well. Thus the left hand side of Eq. (2.23) is the measured data and the right hand side is a known function with three unknown constants. Using a nonlinear least square fit (NLSF) procedure we fit the function to the measured data. The least square fit approximation finds a set of σ_{11}^0, σ_{12}^0 and σ_{22}^0, which minimizes the chi-square value

$$\chi 2 = \sum_i \frac{(r_{rms}^2{}_i - f_{fit}(I_i))^2}{\delta r_i^2}, \tag{2.24}$$

here δr_i is an accuracy of the *i-th* measurement of the RMS beam size. The transverse geometric emittance is calculated following Eq. (2.22) as $\varepsilon = \sqrt{\sigma_{11}^0 \sigma_{22}^0 - (\sigma_{12}^0)^2}$.

The transport matrix of a drift space is

$$R_{drift} = \begin{pmatrix} 1 & D \\ 0 & 1 \end{pmatrix}, \tag{2.25}$$

where D is the drift space length. The transport matrix of a quadrupole has the following form

$$R_{quad} = \begin{pmatrix} cos(kL_{eff}) & sin(kL_{eff})/k \\ -k\,sin(kL_{eff}) & cos(kL_{eff}) \end{pmatrix}, \tag{2.26}$$

where L_{eff} is the effective magnetic length and k is a measure of the quadrupole strength. This is described in more detail below. We multiply R_{drift} and R_{quad} to find the transport matrix from entrance of the quadrupole to the place of the view screen, which is written as

$$R = R_{drift} R_{quad} = \begin{pmatrix} cos(kL_{eff}) - Dk\,sin(kL_{eff}) & sin(kL_{eff})/k + D\,cos(kL_{eff}) \\ -k\,sin(kL_{eff}) & cos(kL_{eff}) \end{pmatrix}. \tag{2.27}$$

Using this transport matrix and Eq. (2.23) we find the fit function

$$f_{fit}(I) = \sigma_{11}^0 (cos(\varphi(I)) - k(I)D sin(\varphi(I)))^2$$

$$+ \sigma_{22}^0 \left(\frac{sin(\varphi(I))}{k(I)} + D cos(\varphi(I)) \right)^2 \qquad (2.28)$$

$$+ 2\sigma_{12}^0 \left(\frac{sin(\varphi(I))}{k(I)} + D cos(\varphi(I)) \right) (cos(\varphi(I)) - k(I)D sin(\varphi(I)))$$

where $\varphi(I) = k(I)L_{eff}$. To illustrate the method and to know what beam RMS size we should expect during quadrupole scan measurements we have calculated the RMS beam size on the view screen for different quadrupole settings and for different beam emittances. For the calculations realistic Courant-Snyder parameters α_T, β_T and, γ_T which PARMELA simulations predicted were used. The results of the calculations are shown in Fig. 2.2, where the beam size is plotted as a function of the quadrupole current.
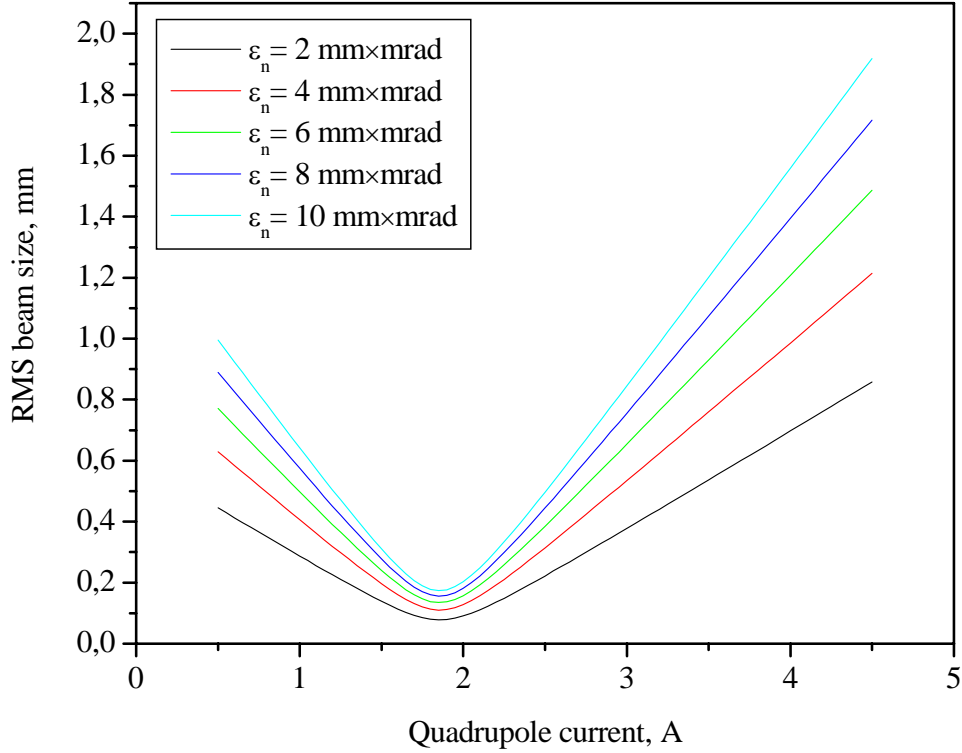
Figure 2.2 Simulations of the quadrupole scan emittance measurements

Note that in this simulation the same initial Courant-Snyder parameters are used for all curves representing beams with different emittance. This condition is not necessarily accomplished in reality. For the measurements' data evaluation one needs some more details about the real parameters of the experimental setup. The quadrupole strength in Eq. (2.25) is $k = \sqrt{\dfrac{B_0}{R_Q} \dfrac{1}{B\rho}}$, B_0 is the magnetic induction on the surface of the magnet pole, R_Q is the quadrupole aperture radius, $B\rho$ is the

magnetic momentum of the quadrupole. There is a practical formula for the $B\rho$ value:

$$B\rho = 33.3564 \cdot P_0, \qquad (2.29)$$

where P_0 is the momentum of the particle measured in *GeV/c* and $B\rho$ is then measured in *kGm* [2.5]. The quadrupole used for the emittance measurements has the following parameters $L_{eff} = 100mm$, $R_Q = 21mm$ and $B_0 = 2.1kG$ at *18.5 A* current in the quadrupole coils. Emittance was measured directly after the accelerating module. The distance between the quadrupole and the view screen measuring the beam profile was $D = 0.475m$. The measurements were done at 12 MeV electron beam energy.

Several beam emittance measurements were performed using the quadrupole scan method. The question that was studied in most detail is the emittance dependence on the bunch charge. In Fig. 2.3 there are several results of quadrupole scan measurements made at different bunch charge. The measured RMS beam size is plotted in dependence with the quadrupole current.
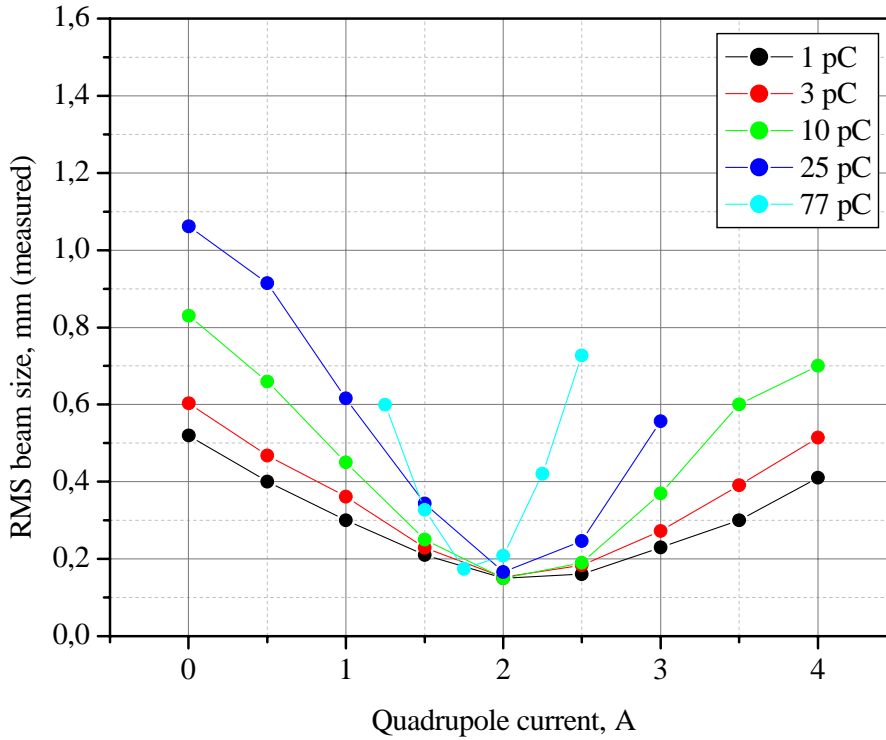
Figure 2.3 Real quadrupole scan emittance measurements

As one can easily see, the picture is somewhat similar to Fig. 2.2. Using the nonlinear least square fit method the experimental data were evaluated as described above. On Fig. 2.4 two examples are shown of the measurements done at 77 pC and 1 pC bunch charge with corresponding NLSF fits. There is a summary of the data evaluation for that plot in Table 2.1. As soon as the beam matrix elements are estimated and the transverse emittance is calculated using Eq. (2.19) one can find the Twiss parameters of the phase space ellipse. There are ellipses shown in Fig. 2.5 corresponding to the measurements presented in Fig. 2.4. It is very evident graphically that the area of the blue ellipse is about four times larger than area of the red one representing a

difference in emittance for 1 pC and 77 pC. Of course the Twiss parameters contain information about the ellipse orientation in the phase space as well.
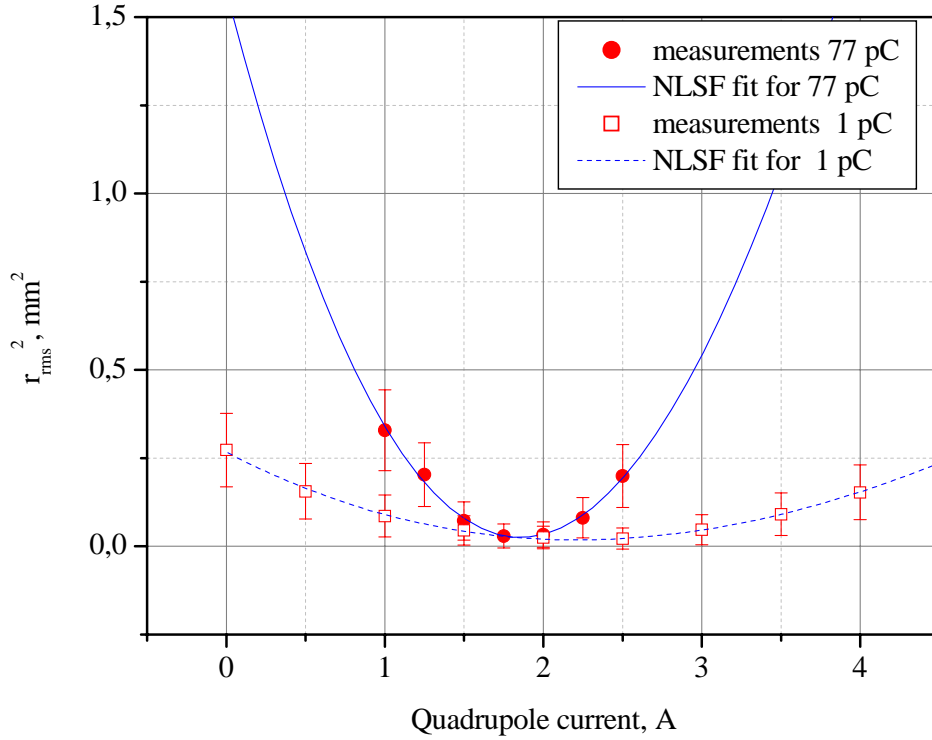
Figure 2.4 Experimental data and corresponding NLSF functions

An important and interesting question is the emittance measurement error arising in the quadrupole scan method. The error of the measurements shown in Fig. 2.4 is presented in Table 2.1 as well. Emittance is not measured directly as if we would measure length of something with the help of a straightedge. Emittance is calculated from three parameters, which in turn are results of a calculation as well. What we do measure practically is the beam profile, length of the drift space, parameters of the quadrupole and the electron beam energy. The quadrupole parameters, length of the drift space and the beam energy are known very precisely and we neglect the measurement errors given from them. Thus our main intention, analyzing the quadrupole scan inaccuracy, is to link the beam profile measurement error, more exactly the RMS beam size inaccuracy, to the final emittance inaccuracy.

	77 pC	1 pC
ε_{RMS}^{n}	7.8 ± 2.9 mm×mrad	2.1 ± 0.25 mm×mrad
σ_{ε}	37 %	12 %
β_{T}	$3.1 + 0.18$ m	$1.2 + 0.03$ m
α_{T}	-1.6 ± 0.08	-1.1 ± 0.03
$\chi 2$	0.1	0.04

Table 2.1 Summary of the NLSF presented in Fig. 2.4
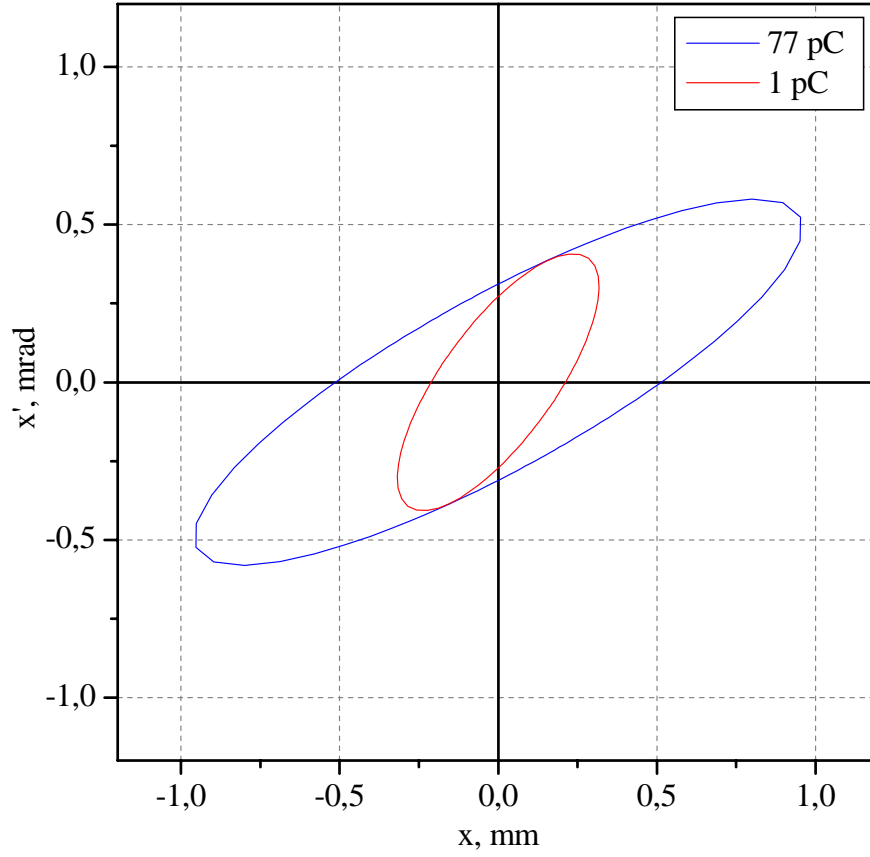
Figure 2.5 Phase space ellipses corresponding to the measurements at 77 pC and 1 pC

Form the error theory we know if a dependent variable y is a function of several independent variables $y = f(x_1, x_2 \ldots x_N)$ and each of the independent variables x_j is known with certain inaccuracy δx_j, then the inaccuracy of the y is $\delta y = \sum_{j=1}^{N} \left| \dfrac{\partial f}{\partial x_j} \right| \delta x_j$. Thus from Eq. (2.22) we have

$$\delta \varepsilon = \frac{1}{2\varepsilon} \left[\sigma_{11} \delta \sigma_3 + \sigma_{22} \delta \sigma_1 + 2 \sigma_{12} \delta \sigma_2 \right], \tag{2.30}$$

where $\delta \sigma_1$, $\delta \sigma_2$, $\delta \sigma_3$ denote respectively $\delta \sigma_{11}$, $\delta \sigma_{12}$, $\delta \sigma_{22}$ and in our case are given by nonlinear least square fit as well as σ_{11}, σ_{12} and σ_{22}. The errors of the least square fit are

$$\delta \sigma_j = \sqrt{\frac{1}{DOF} \sum_i (r_{rms}^2{}_i - f_{fit}(I_i))^2 \cdot C_{jj}}, \tag{2.31}$$

here C_{jj} are the diagonal elements of the variance-covariance matrix, DOF stands for the number of Degrees Of Freedom, which is the difference of measured points number and number of the fit function parameters. The variance-covariance matrix is $C = (J^T \times J)^{-1}$ and J is the Jacobian, $J_{i,j} = \dfrac{\partial f_{fit}(x_i)}{\partial \sigma_j}$. Thus the errors shown in Table

2.1 are calculated using Eqs. (2.30) and (2.31). Now we come back to our main goal, the link between the emittance inaccuracy $\delta\varepsilon$ and the RMS beam size error δr_{rms}. Of course $\delta\varepsilon$ depends on the steepness of the $r_{rms}(I)^2$, i.e., from the fit function, since normally the fit function approximate the experimental data very well. Thus the diagonal elements of the variance-covariance matrix C are involved in $\delta\varepsilon$. In Eq. (2.31) the measure of the fit function deviation from the real data is the value $\dfrac{1}{DOF}\sum_i (r_{rms}^2{}_i - f_{fit}(I_i))^2$. On the other hand, the maximal acceptable deviation of the fit function from the experimental data is the measurement accuracy δr_{rms}. Thus we can substitute in Eq. (2.31) $\dfrac{1}{DOF}\sum_i (r_{rms}^2{}_i - f_{fit}(I_i))^2$ with $\delta r_{rms}{}^2$ which give us a new expression for the beam matrix elements errors

$$\delta\tilde{\sigma}_j = \delta r_{rms}{}^2 \sqrt{C_{jj}} \,. \tag{2.32}$$

This expression links δr_{rms} to $\delta\varepsilon$ if one substitutes $\delta\tilde{\sigma}_j$ into Eq. (2.30). Note that Eq. (2.32) is not an exact solution but is an upper limit, i.e., the worst case. The advantage of this expression is that we can see the error propagation and the error dependence on δr_{rms} and on the steepness of the $r_{rms}(I)$. To demonstrate the error dependence we will do the following numerical experiment. How strong we can focus the beam with the help of a lens depends on the beam size at the entrance of the lens since emittance is a constant. As one can see from Table 2.1 in our measurements at 77 pC bunch charge the β_T function in front of the quadrupole was about 3 m. Imagine that upstream of the quadrupole used for the scan emittance measurements there is another quadrupole placed at some distance from the first one. With the help of this quadrupole we can change size of the beam entering the scanning quadrupole and hence change the β_T function. In Fig. 2.6a it is shown how the phase space ellipse is changing at the entrance of the scanning quadrupole when the upstream quadrupole has different settings. We change the quadrupole current so that the β function has sequentially the values (5 m; 4m; 3m; 2m; 1.5m; 1m; 0.5m; 0.1m). Different β_T functions will cause different steepnesses of the scan function as is shown in Fig. 2.6b. The inaccuracy of the emittance calculation for different initial β_T function is depicted in Fig. 2.6c as a function of the RMS beam size error δr_{rms}. Real inaccuracy in the RMS beam size estimation is about 100 µm. This, together with $\beta=3$ m, gives a reasonable accuracy of about 30 % for the emittance calculation. Nevertheless the accuracy of 30 % can be easily improved by optimization of the initial β_T function. Thus, as follows from the calculations shown in Fig. 2.6c, an optimal initial β_T function for the emittance measurements at 77 pC bunch charge would be about 1 m, which would improve the accuracy by a factor of 3. Another way to make the emittance error better is to increase the number of measured points, thus we have measured the beam size at six different values of the quadrupole current. Doubling of this number would improve the accuracy by a factor of 2.5 according to the simulations.
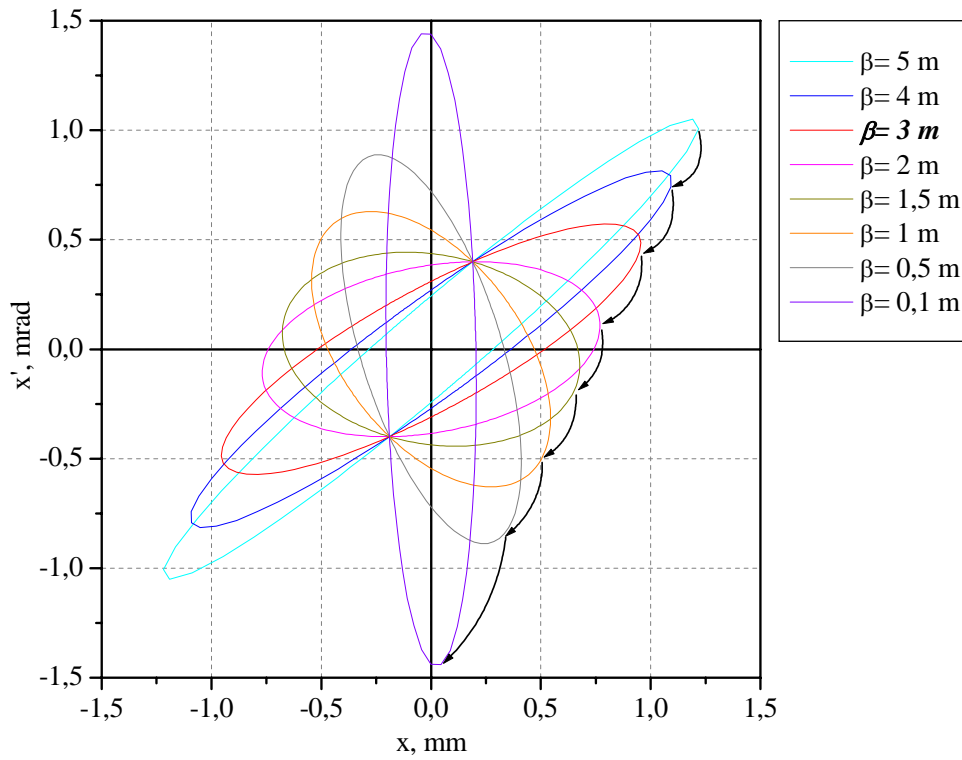
Figure 2.6a Phase space ellipses corresponding to different β function values
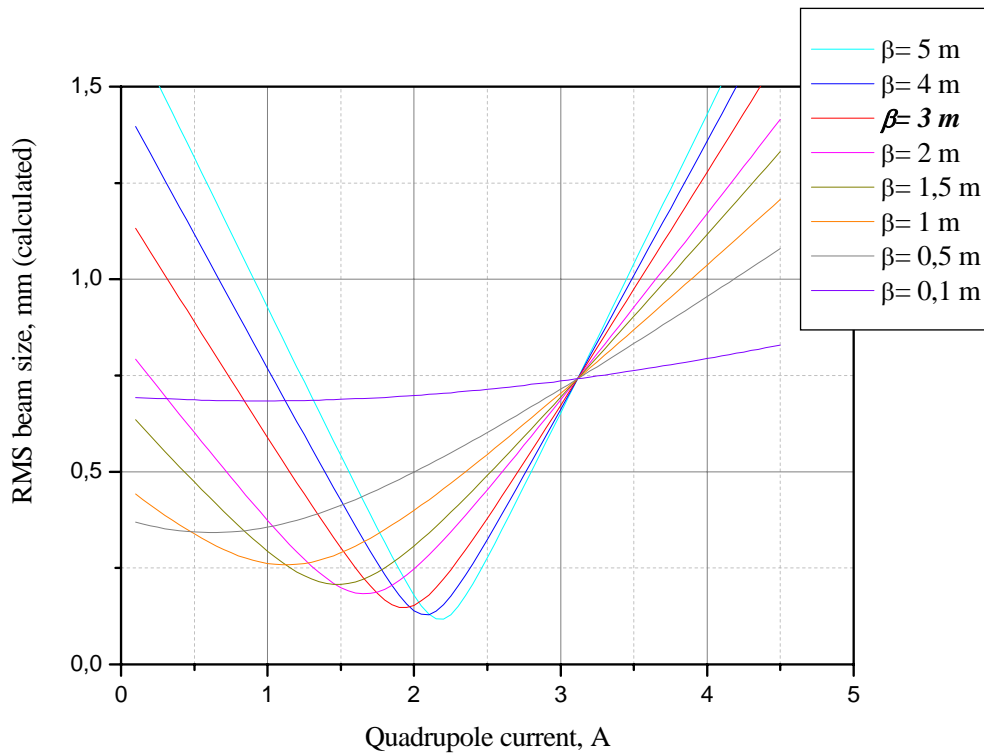
Figure 2.6b Simulated quadrupole scans for different β function values
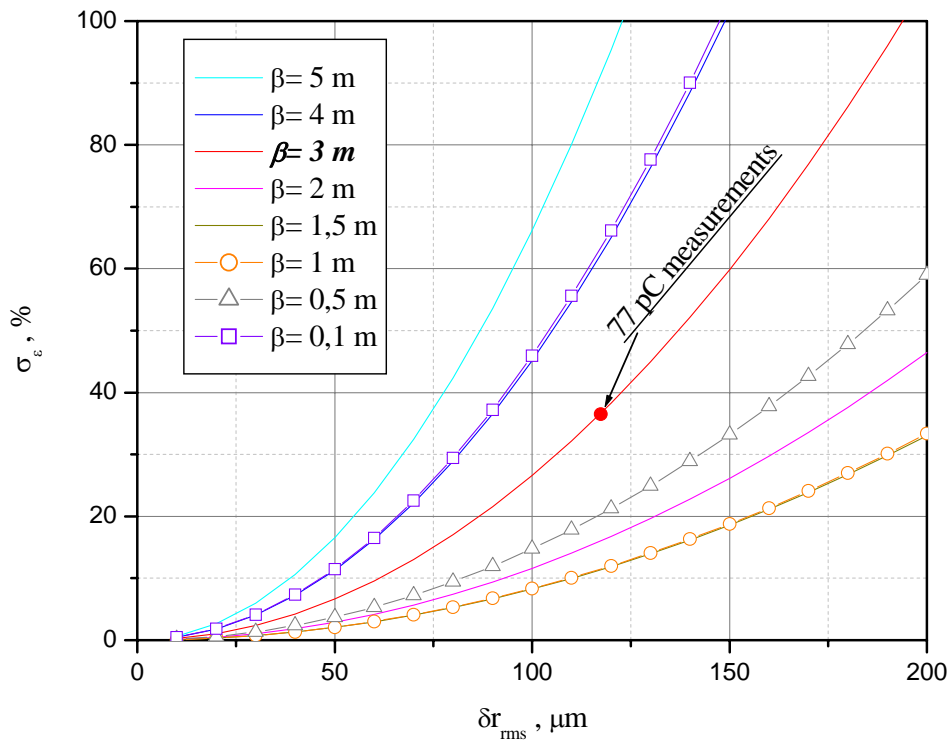
Figure 2.6c Accuracy of the quadrupole scan emittance measurements with different β function values at the entrance of the quadrupole

Summarizing the quadrupole scan emittance measurements we want to note here that for the FEL design bunch charge of 77 pC the normalized transverse emittance of a 12 MeV beam is measured to be 7.8 ± 2.9 mm×mrad. This corresponds to a geometrical emittance of about 0.3 ± 0.1 mm×mrad or just 0.3 μm. The 12 MeV beam energy is about smallest design beam energy for the FEL operation. Increasing the electron beam energy decreases the geometrical emittance as $1/\gamma\beta$. As discussed in Chapter 1, FEL operation requires the geometrical emittance to be less than the FEL wavelength. The 0.3 μm emittance is about one order of magnitude less than the shortest design wavelength of the ELBE FEL and cannot cause any significant FEL gain reduction.

2.5 Beam envelope analysis

The quadrupole scan method is based on the linear matrix formalism of the beam transport where the *R* matrix plays a central role. The *R* matrix originates from single particle consideration of the beam transport without the space charge force of the bunch itself. Hence the linear beam transport and the quadrupole scan method are valid when particle interaction within the beam is negligible. One has to make sure, making the quadrupole scan measurements, that this approximation is valid. To estimate the significance of the space charge force effects for transverse beam dynamics envelope equation [2.6] can be used.

The most general form of a beam envelope equation is

$$\sigma'' + k^2\sigma + \frac{\gamma'}{\beta^2\gamma^2}\sigma' - \frac{2I}{I_A\beta^3\gamma^3}\frac{1}{\sigma} - \frac{\varepsilon^2}{\sigma^3} = 0, \qquad (2.33)$$

here σ stands for the RMS beam radius, I is the beam peak current, $I_A = ec/r_e$ is the non-relativistic Alfen current already introduced in the previous chapter, ε is the beam geometrical emittance, γ and β are the relativistic factors. The second term in this equation represents the external focusing field, the third term is responsible for synchrotron radiation, the fourth one takes into account the self space charge force of the beam and the last one represents the influence of the beam emittance on the beam envelope. In a drift space the external focusing field is zero, therefore the second term in Eq. (2.33) is zero as well as term three, since the beam is not in a bend magnet and there is no synchrotron radiation. Hence, two factors rule the beam envelope in a drift space. These are the beam emittance and the force of the bunch space charge i.e. $\sigma'' = \frac{2I}{I_A\beta^3\gamma^3}\frac{1}{\sigma} + \frac{\varepsilon^2}{\sigma^3}$. Dependent on the dominant term the beam is called emittance dominated or space charge dominated. Following Rosenzweig and Travish [2.7] we introduce the ratio of the space charge term to the emittance term

$$\Re_0 = \frac{2I\sigma^2}{I_A\gamma\beta\varepsilon_n^{2}} \qquad (2.34)$$

where the normalized emittance ε_n is used instead of the geometrical one. If the ratio is much smaller than one, the space charge effects are small and the quadrupole scan method works well. The situation is different for the injector beam and for the accelerated beam, in the sense of the dominant envelope factor. The first reason for that is the big difference in the bunch length and hence the beam peak current. In the ELBE injector the bunch coming out of the gun with a characteristic length of about 500 ps and is compressed down to 10 ps with the help of two buncher cavities. During acceleration in the superconducting cavities the bunch is compressed again and the degree of compression is a function of the first accelerating cavity phase. The bunch length measurements in the injector and downstream of the accelerating module will be discussed detailed in the next chapter. The bunch length measured for a 12 MeV beam has a longitudinal RMS size from 2 up to 4 ps dependent on the first cavity phase. Another difference between the injector beam and the accelerated beam is the transverse size, since the geometrical emittance is reduced by factor of $1/\gamma\beta$. To prove the validity of the quadrupole scan emittance measurements done with the 12 MeV beam we have calculated the ratio 2.34 with a RMS beam size of 1.5 mm. The results of the calculation are shown in Fig. 2.7a. Here the ratio is calculated as the function of the bunch length for three different bunch charges with their realistic emittance values. For the 12 MeV beam the ratio stays well below one for all realistic bunch length. Increasing the beam energy will make the ratio even smaller as follows from 2.34. Consequently the quadrupole scan is a proper method for emittance measurements of accelerated beam. The situation is different in the injector. The calculated space charge term to the emittance term ratio for the injector beam with an RMS beam size of 1.5 mm as a function of the bunch length is plotted in Fig. 2.7b. The ratio is calculated again for the same three values of the bunch charge with realistic emittance values. Because of the bunch compression in the injector, the beam becomes space charge dominated. Certainly the space charge dominance is stronger for a bigger bunch charge, i.e., in the case which is more important for the FEL operation.

E=12 MeV; σ=0,3 mm (accelerator)
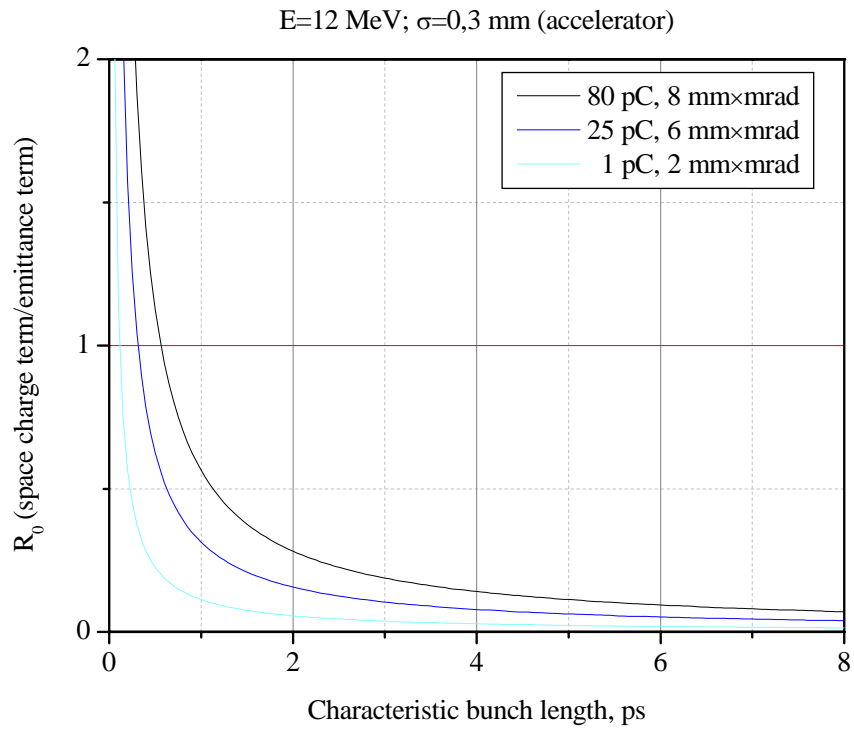
Figure 2.7a Ratio of the space charge term to the emittance term in the beam envelope equation for a 12 MeV beam

E=250 keV; σ=1,5 mm (injector)
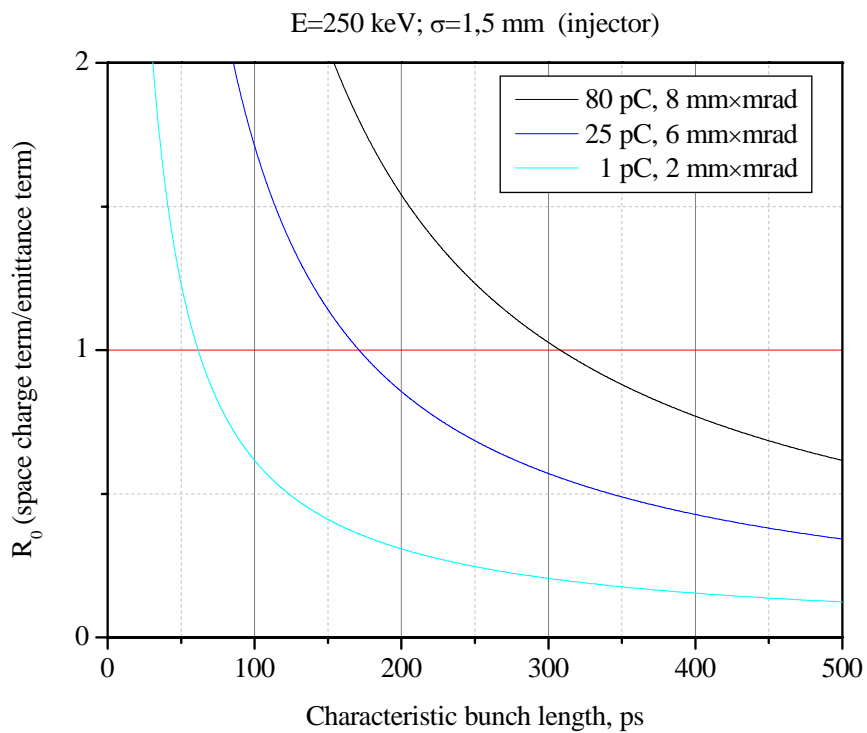
Figure 2.7b Ratio of the space charge term to the emittance term in the beam envelope equation for the ELBE injector beam

The ratio reaches a value of 30 at the entrance of the accelerating module for 80 pC bunch charge with 8 mm×mrad of normalized emittance when the bunch length is about of 10 ps. Obviously the beam is space charge dominated in the injector for almost all relevant beam parameters. This is why a quadrupole scan like method is not appropriate for the emittance measurements without any additional changes in the data evaluation. We have used another method to measure the transverse emittance in the ELBE injector. This is the multislit method, which is the topic of the next section.

2.6 Multislit emittance measurements in the ELBE injector

The basic idea of the method is the following. A space charge dominated beam is intercepted by a set of apertures so that effectively only a small part of the beam is propagating through the intercepting mask. Thus the beam current and consequently influence of its space charge is reduced. After the mask the remaining beamlets propagate in a free from magnetic elements drift space to a place where their profiles are measured. The apertures are designed so that the part of the beam going through is emittance dominated. Hence, in the drift space the transverse momentum of the electrons is not affected by the repulsive Coulomb field and is given only by the particle distribution in the phase plane in front of the mask. Sometimes this technique is called phase space sampling. The principle is illustrated in Fig. 2.8.
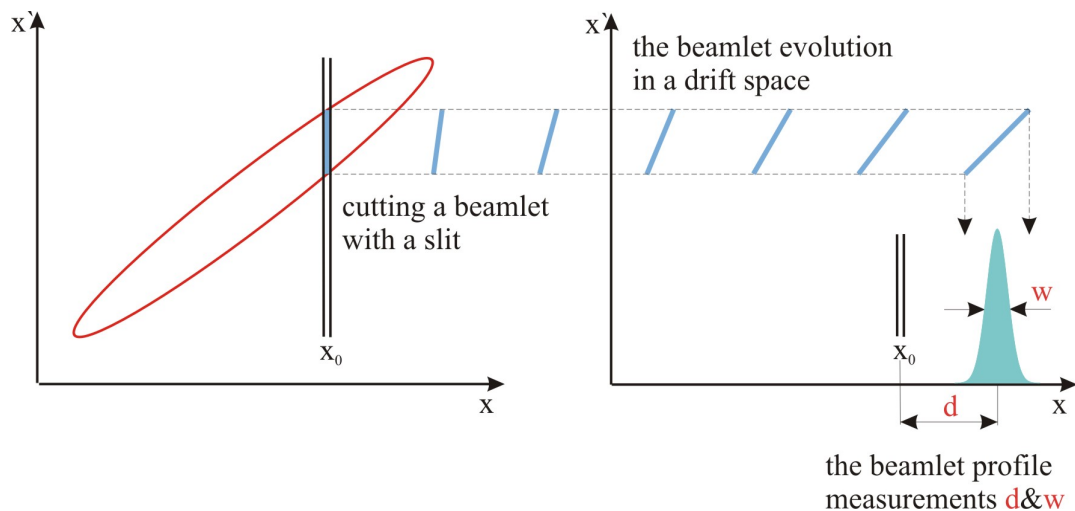
Figure 2.8 The phase space sampling principle

On the left side of Fig. 2.8 the red ellipse depicts the phase space shape of the beam in front of the mask. With the small slit placed at the position x_0 we cut a beamlet oriented vertically in the phase space plane. The beamlet gets tilted during its propagation in the drift space, since its top and bottom have different transverse momentum. Obviously, the degree of the inclination depends on the initial divergence spread $\Delta(x_0')$ and on the drift length as well. At the end of the drift space the beamlet profile, i.e., the beamlet projection to the *x*-axis, is measured. Now the width of the profile *w* contains information about uncorrelated transverse momentum spread in the vicinity of x_0 and the absolute position of the peak, more exactly its displacement *d*

from x_0, carries the information about the correlated beam divergence. The area of the beamlet profile A is proportional to the number of particles passed through the slit. Thus by doing such measurement we will know the phase space distribution around x_0. Repeating the measurement for different positions of the slit we could entirely reconstruct the phase space distribution of the beam and calculate its emittance. The only drawback of such a method would be its time consumption. To speed up the measurements several slits are used simultaneously so that emittance and the phase space distribution are measured in one shot.
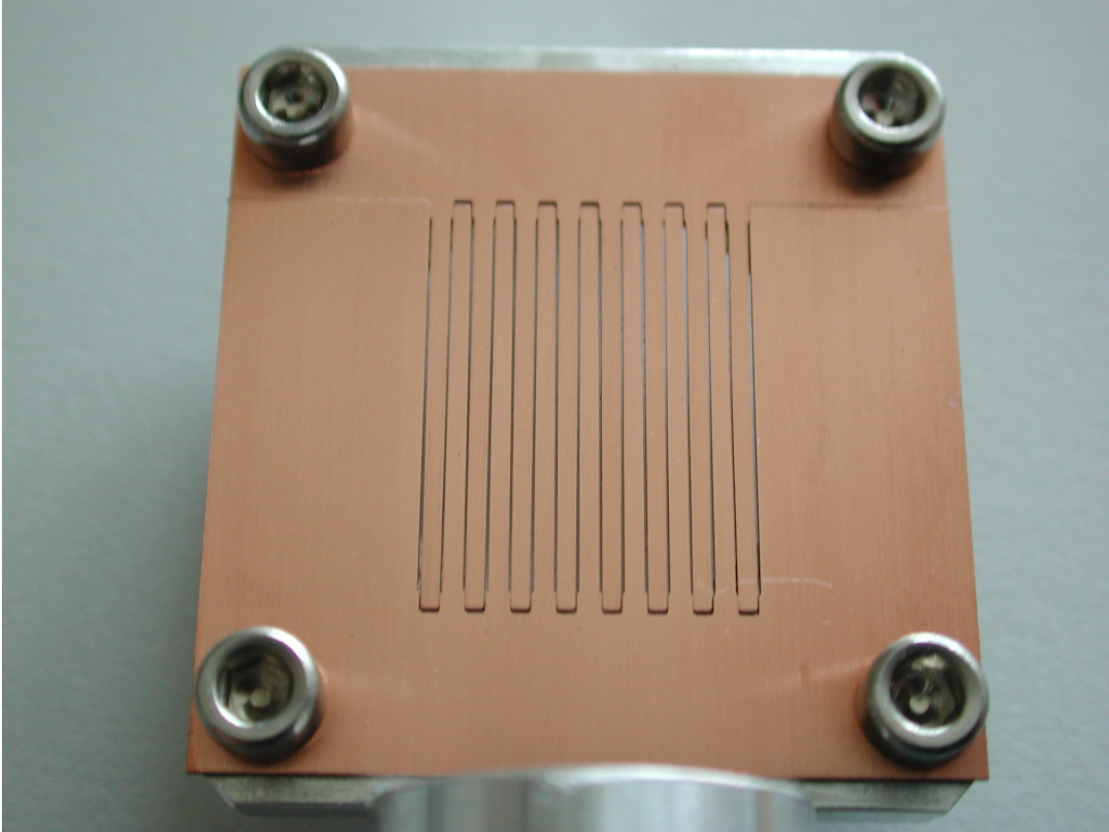
Figure 2.9 The multislit mask used in the emittance measurements

Parameters of the intercepting mask and the drift length have to be optimized for a certain value of the emittance to be measured. We need to fulfill following criteria to make the emittance measurements correct:

- Angular acceptance of the slit must be significantly bigger then the uncorrelated beam divergence, which can be written as

$$\Re_1 = \frac{2D}{d}\frac{\varepsilon}{\sigma} << 1,$$

(2.35)

  where ε is the beam emittance, σ is RMS beam size at the multislit mask, d is the slit width and D is the mask thickness.

- At the end of the drift space the distance from any beamlet to a neighboring has to be bigger than the beamlet width

$$\Re_2 = \frac{L}{w}\frac{\varepsilon}{\sigma} << 1,$$

(2.36)

where L is the drift length and w is the distance between slits. In other words, the separation of the peaks coming from different slits has to be big enough.

- The drift space has to be long enough to let the beamlet expand so that at the end of the drift space its RMS size is much bigger than the slit width, since the slit RMS width is $\dfrac{d}{2\sqrt{3}}$ this condition can be written as

$$\Re_3 = \frac{2\sqrt{3}}{d}\frac{\varepsilon}{\sigma}L \gg 1. \tag{2.37}$$

As a consequence the slit width d is not present in the emittance calculation.

- Residual space charge force between the beamlets has to be negligible, i.e., the beam behind the mask is emittance dominated. According to [2.7] this condition can be written as following

$$\Re_4 = \frac{2I}{I_A\gamma^2\varepsilon_n}\frac{dL}{w} \ll 1. \tag{2.38}$$

Here we present and discuss emittance measurements done at the gun test stand during commissioning of the gun. The experimental setup had following parameters: the drift length L=250 mm, the slit width d=100 μm, distance between the slits w=1.6 mm, the mask thickness D=1 mm. The multislit mask used in the emittance measurements is shown in Fig. 2.9. The mask is made of 1 mm thick copper and manufactured with the help of a wire cut machine. The slit width accuracy is about 5 μm. It is more difficult to satisfy ratios $\Re_1$ and $\Re_2$ with a bigger value of emittance. The opposite ratios $\Re_3$ and $\Re_4$ are more hard to satisfy for low emittance value. Because of this and because of the fact that the RMS beam size on the slit might not be as large as assumed, any setup for the emittance measurements has a certain acceptance range for the emittance value within which it can be measured with good accuracy. Besides that, one always have to make sure during the measurement that the entire beam is coming onto the slit area and that without the mask the whole beam fits on the view screen used for the profile measurements. In table 2.2 the calculated values of the ratios $\Re_1$, $\Re_2$, $\Re_3$ and $\Re_4$ are shown for two different values of the emittance, 8 mm×mrad and 2 mm×mrad. The calculations are done for 70 pC bunch charge, 3 mm RMS beam size on the mask and uncompressed injector beam of 450 ps bunch length. The value of 8 mm×mrad is almost the upper limit of the setup acceptance. Most critical is the ration $\Re_2$ that means with the emittance value bigger than 8 mm×mrad peak separation on the view screen becomes so bad that any reasonable measurements are not possible. Note that here we talk about geometrical emittance.

	must be	8 mm×mrad	2 mm×mrad
$\Re_1$	*<<1*	0.05	0.01
$\Re_2$	*<<1*	0.39	0.09
$\Re_3$	*>>1*	21.5	5.4
$\Re_4$	*<<1*	0.02	0.07

Table 2.2 Calculated values of the ratios $\Re_1$, $\Re_2$, $\Re_3$ and $\Re_4$ for emittance values of 8 mm×mrad and 2 mm×mrad

A typical beam profile measured behind the multislit mask is shown in Fig. 2.10. In this case the horizontal emittance is measured. The projection of the beam profile to the X-axis is calculated and is also shown on the bottom of Fig. 2.10. Then the number and position of the peaks are estimated automatically and the projection is approximated with the help of a nonlinear least square fit by the fit function, which is a sum of Gaussian peaks i.e.

$$F_{fit}(x) = \sum_i \frac{A_i}{\sigma_i \sqrt{2\pi}} exp\left(-\frac{x - x_{0_i}}{\sigma_i \sqrt{2}} \right)^2 . \qquad (2.39)$$

On the bottom part of Fig. 2.10 the projection is depicted by the white curve, the result of the fit is shown by red bold curve, and the individual Gaussian peaks are shown as magenta dashed lines. Once the fit is done we can calculate the RMS emittance defined by Eq. (2.8). To do so we need to calculate the three second momenta of the particles distribution namely $\langle x^2 \rangle$, $\langle x'^2 \rangle$ and $\langle x \cdot x' \rangle$. At first the statistical weight of every beamlet is defined. This is a measure of how many electrons are in the beamlet. The weight is $\omega_i = \dfrac{A_i}{\sum\limits_i A_i}$. Within the average value of a variable we understand average to mean with the statistical weight, for example $\langle a \rangle = \sum\limits_i \omega_i a_i$. The term $\langle x^2 \rangle$ carries information about the RMS beam size at the mask and is calculated as $\langle x^2 \rangle = \sum\limits_i \omega_i (x_i)^2$, where $x_i = i \cdot w - \sum\limits_i \omega_i \cdot i \cdot w$, w is the distance between the slits. The term $\langle x'^2 \rangle$ takes into account both correlated $\dfrac{(x_{0_i} - \langle x_0 \rangle) - x_i)}{L}$ and uncorrelated $\dfrac{\sigma_i}{L}$ beam divergence and it is calculated as $\langle x'^2 \rangle = \sum\limits_i \omega_i \dfrac{\sigma_i^2 + ((x_{0_i} - \langle x_0 \rangle) - x_i)^2}{L^2}$. The last term $\langle x \cdot x' \rangle$ is a measure of the correlation between beam size and the beam divergence. This is why it takes into account only correlated beam divergence and is calculated as $\langle x \cdot x' \rangle = \sum\limits_i x_i \omega_i \dfrac{(x_{0_i} - \langle x_0 \rangle - x_i)}{L}$. Substituting these results into Eq. (2.8) we get the equation for the emittance calculation written as follows

$$\varepsilon_{RMS} = \frac{1}{L} \sqrt{\left(\sum_i x_i^2 \omega_i \right) \left(\sum_i \omega_i \left(\sigma_i^2 + \left(x_{0_i} - \langle x_0 \rangle - x_i \right)^2 \right) \right) - \left(\sum_i x_i \omega_i \left(x_{0_i} - \langle x_0 \rangle - x_i \right) \right)^2} , (2.40)$$

where σ_i and x_{0_i} are parameters of the Gaussian peaks found by the NLSF and i is the slit index and index of the corresponding Gaussian peak. In the upper left corner of Fig. 2.10, the emittance value corresponding to the beam profile is shown.

The next important question is: what is uncertainty of such emittance measurements? The same approach is used here to estimate the measurement inaccuracy as in the case of quadrupole scan method. In fact in the emittance calculation procedure the emittance is the defined function of several independent variables, i.e., $\varepsilon_{RMS} = g(w, L, \sigma_i, x_{0_i}, A_i)$, where g stands for Eq. (2.40). Each of the parameters is known with certain accuracy. The drift length L and the slit period w are known with very good accuracy so we neglect their error contribution to the final
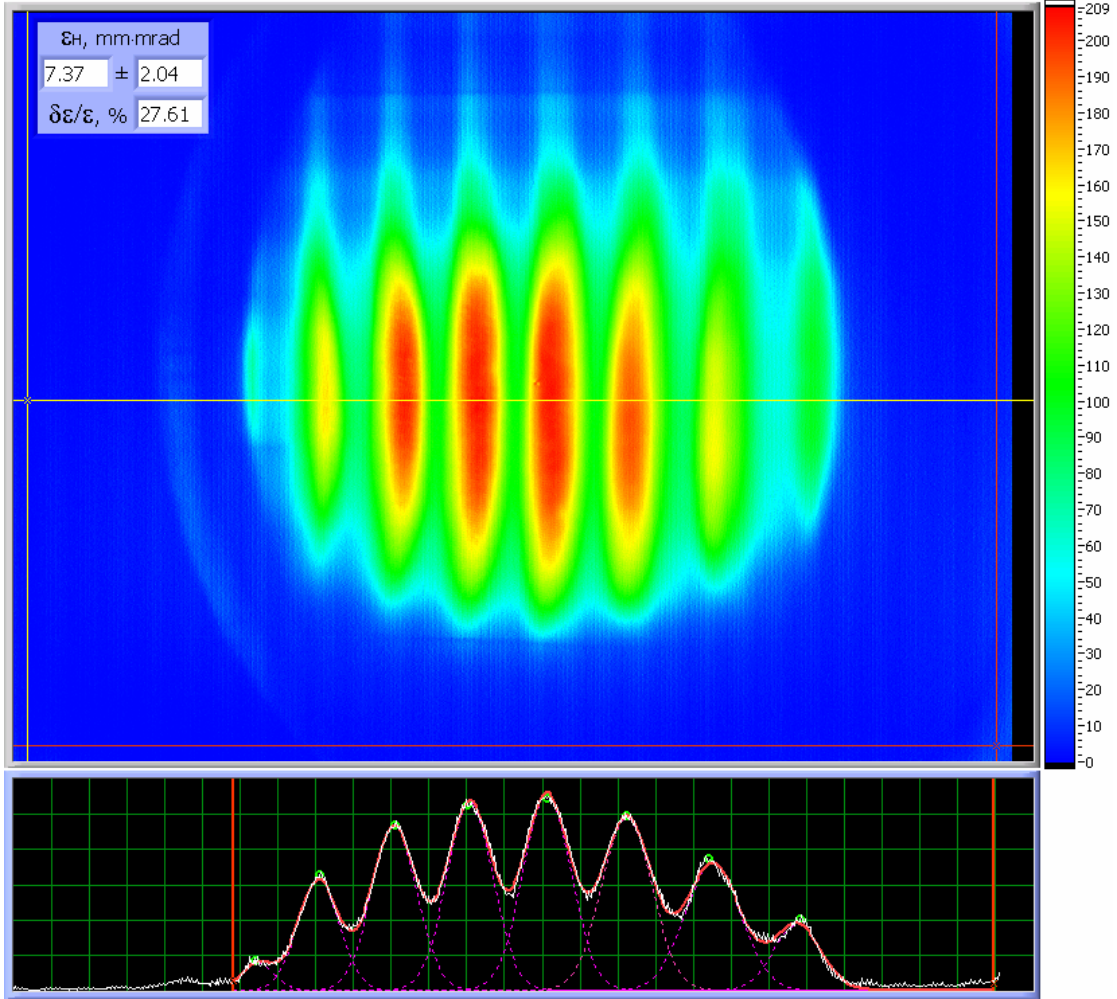
Figure 2.10 Typical beam profile obtained during the emittance measurements

inaccuracy of the emittance. Thus only the inaccuracy of the NLSF or in other words $\delta\sigma_i$, δx_{0i} and δA_i defines the emittance error $\delta\varepsilon_{RMS}$.

Following the principle of error theory, which is described in Section 2.4 we can write

$$\delta\varepsilon_{RMS} = \sum_i \left(\left| \frac{\partial g}{\partial A_i} \right| \delta A_i + \left| \frac{\partial g}{\partial x_{0i}} \right| \delta x_{0i} + \left| \frac{\partial g}{\partial \sigma_i} \right| \delta\sigma_i \right), \tag{2.41}$$

where δA_i, δx_{0i} and $\delta\sigma_i$ are defined by the NLSF over variance-covariance matrix. It was already described in more detail in Section 2.4 regarding the quadrupole scan. The nature of the error is the following. When we calculate emittance using Eq. (2.40) one strong assumption is made that is that the beam profile is really a sum of several Gaussian peaks. In fact there is always difference between the real data and such an approximation and this difference defines the error in the emittance calculation. There is another way to treat the experimental data. One could reject an approximation with the set of Gaussian peaks and calculate position, area and the RMS width of every single observed peak. Then the same formula (2.40) together with parameters obtain from such approximation can be used to calculate the emittance. Since the parameters correspond to real data but not to any approximation function, the accuracy of such data evaluation has to be much better than in the procedure we used. A serious

drawback of this approach is that it can be used only in the case when different peaks are completely separated from each other. This is why the method we used is more flexible and robust in respect to experimental data quality. Furthermore the procedure with Gaussian multi-peak approximation increases the range of the emittance acceptance which can be measured with given experimental setup. In our measurements the relative error increases with increasing bunch charge. If for the small bunch charge of about 0.1 pC the relative error is about of 10 %, for the bunch charge of 60 pC the relative error is about 30 %. We have measured the transverse emittance in both X and Y planes. Results of measurements with the corresponding accuracy are shown in Fig. 2.11. Results of the quadrupole scan measurements are shown in Fig. 2.11 as well.
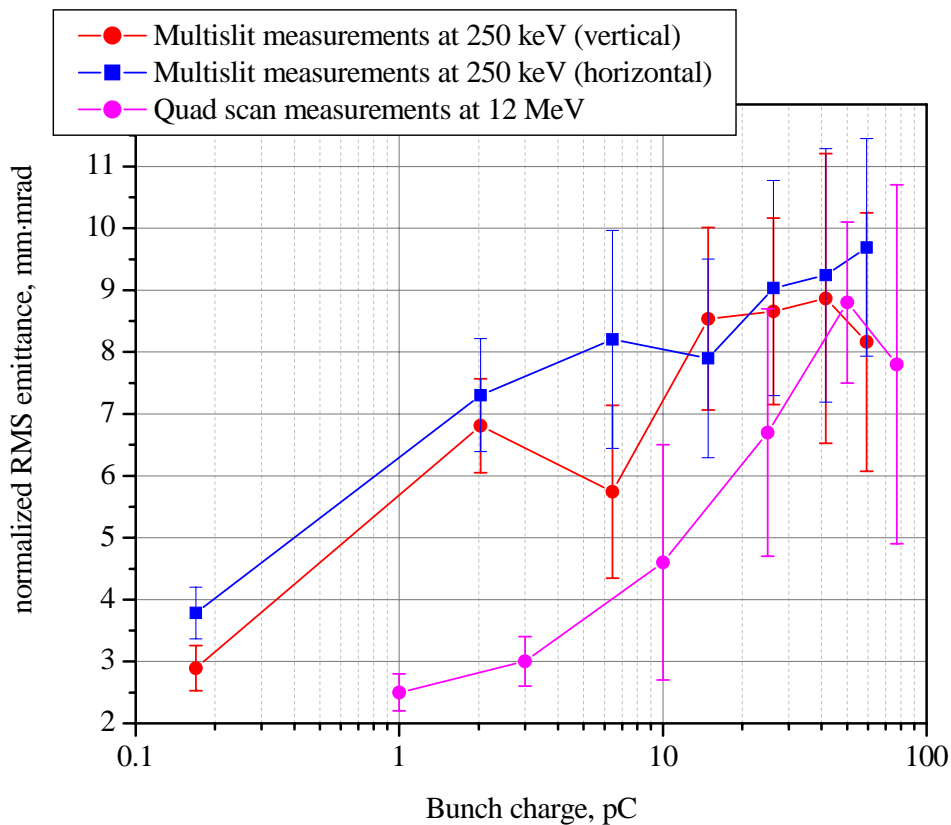
Figure 2.11 Normalized RMS emittance measured in the injector with the multislit method

Summarizing the emittance measurements we have to notice several points. First of all as one can see emittance grows when the bunch charge is increased. It is also clear that the emittance increases already in the injector. The effect was understood and described very well and simulated with computer codes by Jochen Teichert [2.8]. It is interesting that this is not a simple repulsive effect of the bunch space charge as one might first think. The emittance increases beginning in the electron gun. The gun is a thermionic triode delivering electrons with kinetic energy of 250 keV. There is a grid near the gun cathode to make the electron beam pulsed. There are two factors defining the grid electrical potential in respect to the cathode. A pulsed generator with constant amplitude drives the grid. To let a certain charge penetrate through the grid and be accelerated in the gun a variable DC bias is applied to the grid. One can adjust the

bunch charge by changing this bias level. When the gradient of the electrical field is different upstream and downstream the grid, it works as an electrostatic lens. Obviously at different bias values the lens affects the electrons coming through the grid in different ways. At the very beginning the emittance of the beam is defined by the cathode radius and by the focusing effect of the grid. This mechanism is responsible for the emittance increase which has been measured. The next point to notice is that emittance measured with the quadrupole scans downstream of the accelerator is less than emittance in injector. Liouville's theorem [2.2] says that this is not possible. The reason for the difference is the following. The quadrupole scan measurements were performed approximately one year after the measurements in injector. During this time the cathode has changed the efficiency of its emission. The efficiency droped down and, as a consequence, the effective radius of the cathode was reduced. For that reason the emittance of the electron really gets smaller. Later multislit measurements in injector have proved this and are in good agreement with the quadrupole scan measurements shown in Fig. 2.11.

2.7 Conclusion

In this chapter we have discussed the concept of a charged particle beam's transverse emittance. Two different techniques used to measure emittance at ELBE were described including their errors analysis. The emittance was measured in the ELBE injector where the beam energy is 250 keV and downstream of the accelerator module at a beam energy of about 12 MeV. All measurements have reasonable accuracy and are in agreement with each other. At the design bunch charge of the FEL of 77 pC the normalized RMS emittance is measured to be about 8 mm×mrad. An electron beam with such emittance will not cause any significant reduction of the FEL gain.

Chapter 3

Bunch length measurements

3.1 Introduction

As was already pointed out in the first chapter the electron bunch length measurement is an essential part of the FEL electron beam diagnostics. Two main reasons for that are the slippage effect and the strong dependence of the FEL gain on the electron beam peak current.

A simplified layout of the ELBE FEL, with the elements acting on the longitudinal phase space, is shown in Fig. 3.1. In general, the idea of the longitudinal phase space evolution for the ELBE FEL is the following: an electron bunch coming out of the electron gun has a FWHM length of about 450 ps and a longitudinal profile close to Gaussian. In the injector the bunch is compressed longitudinally down to about 10 ps. Two cavity bunchers do the bunch compression. The 10 ps long bunch is injected into the first accelerating module #1. At the module exit the bunch is several picoseconds long, slightly compressed during acceleration. The module also dramatically increases the beam energy spread. The elements influencing the longitudinal phase space on the way from the module #1 exit to the undulator are the magnetic bunch compressor "chicane", the accelerating module #2, and the "S" shaped part of the beam-line. The "S" has a constant R_{56} and rotates the longitudinal phase space clockwise. The chicane has adjustable R_{56} and rotates the longitudinal phase space counterclockwise. The R_{56} is an element of the R matrix introduced in Eq. (2.15). Thus by adjusting the magnetic chicane one can minimize the bunch length at the undulator entrance.

In the frame of this thesis the bunch length, which is in picosecond scale, was measured at the exit of the accelerating module. The measurements were done during commissioning of the ELBE linac as a part of the module characterization. The measurements were performed using a Martin-Puplett interferometer to measure an autocorrelation function of the coherent transition radiation (CTR). Another technique was developed to minimize the bunch length in the injector. The technique utilizes a

BPM placed at the end of the injector. The BPM signal is analyzed in the time and in the frequency domain to find the optimal injector settings.
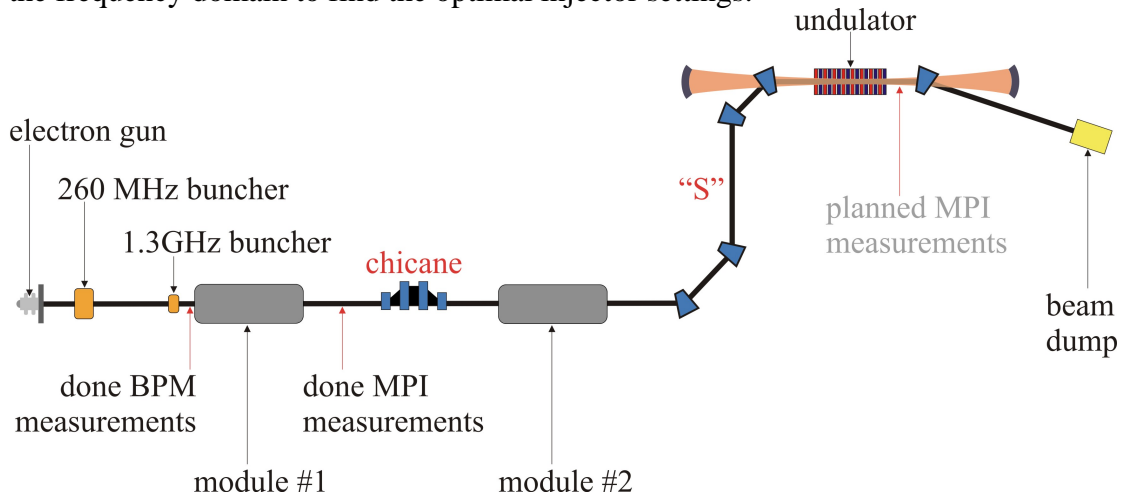
Figure 3.1 Layout of the ELBE FEL; beamline elements acting on the bunch length; positions of the bunch length measurements

3.2 Bunch length evolution at ELBE

Based on the general idea of the longitudinal phase space evolution for the ELBE FEL, a detailed design was made using PARMELA numerical simulations [3.1]. Here we concentrate only on that part of the accelerator where the evolution is essential for the measurements as described below. Figure 3.3 shows some longitudinal phase space shapes and their projections to the energy and the time axes at some key points along the beamline. These are results of a PARMELA run made with 2000 macroparticles with an effective bunch charge of 77 pC.

As was already mentioned in the previous chapters, the ELBE electron gun is a thermionic triode. A constant DC voltage of 250 keV is applied between the cathode and the anode. The average accelerating gradient in the gun is about 1.8 MV/m. The control grid is placed 200 μm from the cathode. An RF circuit based on avalanche diodes drives the grid. The shape of the voltage pulse given to the grid defines the longitudinal shape of the electron bunch coming out of the gun. The pulsed shape measured using a 6 GHz sampling oscilloscope is shown in Fig. 3.2. The starting bunch length depends on the bunch charge as well, since a different offset voltage has to be applied to the grid to produce bunches with a different bunch charge. Here we are interested mainly in the maximum design bunch charge, i.e., 77 pC. The starting FWHM of such a bunch is 450 ps.

The fundamental frequency of the linac is 1.3 GHz. This corresponds to a period of 769 ps. The bunch produced by the gun is too long to be directly accelerated and for this reason is compressed longitudinally in the injector. The compression is done in two stages. First the 260 MHz buncher modulates the energy of the electrons within the bunch so that electrons in the head of the bunch are decelerated, while the electrons in the tail of the bunch are accelerated. The bunch center does not change its energy in the buncher. The buncher is a normal conducting coaxial cavity and is operated in the TM_{010} mode.
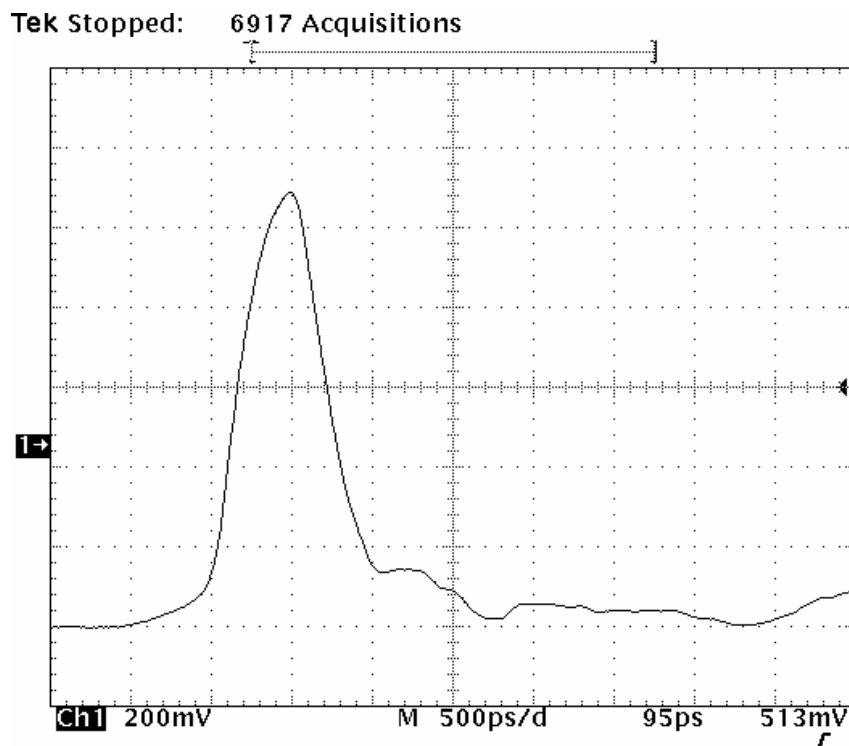
Figure 3.2 Shape of the pulse on the control grid of the electron gun

The 450 ps long bunch fits very well in the range where the 260 MHz field is linear. As a result at the buncher exit the energy of the electrons within the bunch is a linear function of the longitudinal coordinate. The phase space at the buncher exit is shown in Fig. 3.3 (a). It is important that at the energy of 250 keV the electrons are not fully relativistic and, having different energies, have also different velocities. Propagating further in a drift space, the electrons come together and get grouped around the bunch center. The phase space shape after the 3 m long drift space is plotted in Fig. 3.3 (b). This point is the entrance of the second buncher. The effect of the repulsive space charge force can be seen at this point. The force accelerates head of the bunch and decelerates its tail. Accordingly the head and the tail of the phase space distribution become bent, changing the phase space shape from the linear to a sine-like one. The second buncher is also a normal conducting coaxial cavity operating in the TM_{010} mode but at the fundamental frequency of 1.3 GHz. The buncher has the same effect on the longitudinal phase space as the first one and compresses the bunch further so that the longitudinal focal point is at the entrance of the accelerating module. Figure 3.3 (c) shows the phase space distribution at the second buncher exit.

Todd Smith proposed to use the two buncher compression scheme at ELBE. When the bunch is compressed the density of the electrons is increased as well as its electric field strength. The space charge field causes beam emittance growth. To reduce this effect, one has to shrink the time when the bunch electric field badly affects the emittance. That is to say the bunch has to be compressed as fast as possible. On the other hand a very high field gradient in the subharmonic buncher would take too much RF power. Therefore the subharmonic buncher is used to reduce the bunch length so that the fundamental buncher can be used. The last one compresses the bunch as fast as it can. The two buncher scheme is a trade-off between acceptable emittance growth and reasonable RF power required for the bunchers [3.2].

Figure 3.3 Evolution of the longitudinal phase space at ELBE

Bunch length is reduced in the first cells of the cavity #1 of the accelerating module at the same time the energy spread increases dramatically. The most important feature of cavity #1 is that in the cavity the electrons become relativistic. For that reason difference in energy leads to a very small difference in the velocity so that the electron bunch length stays almost constant do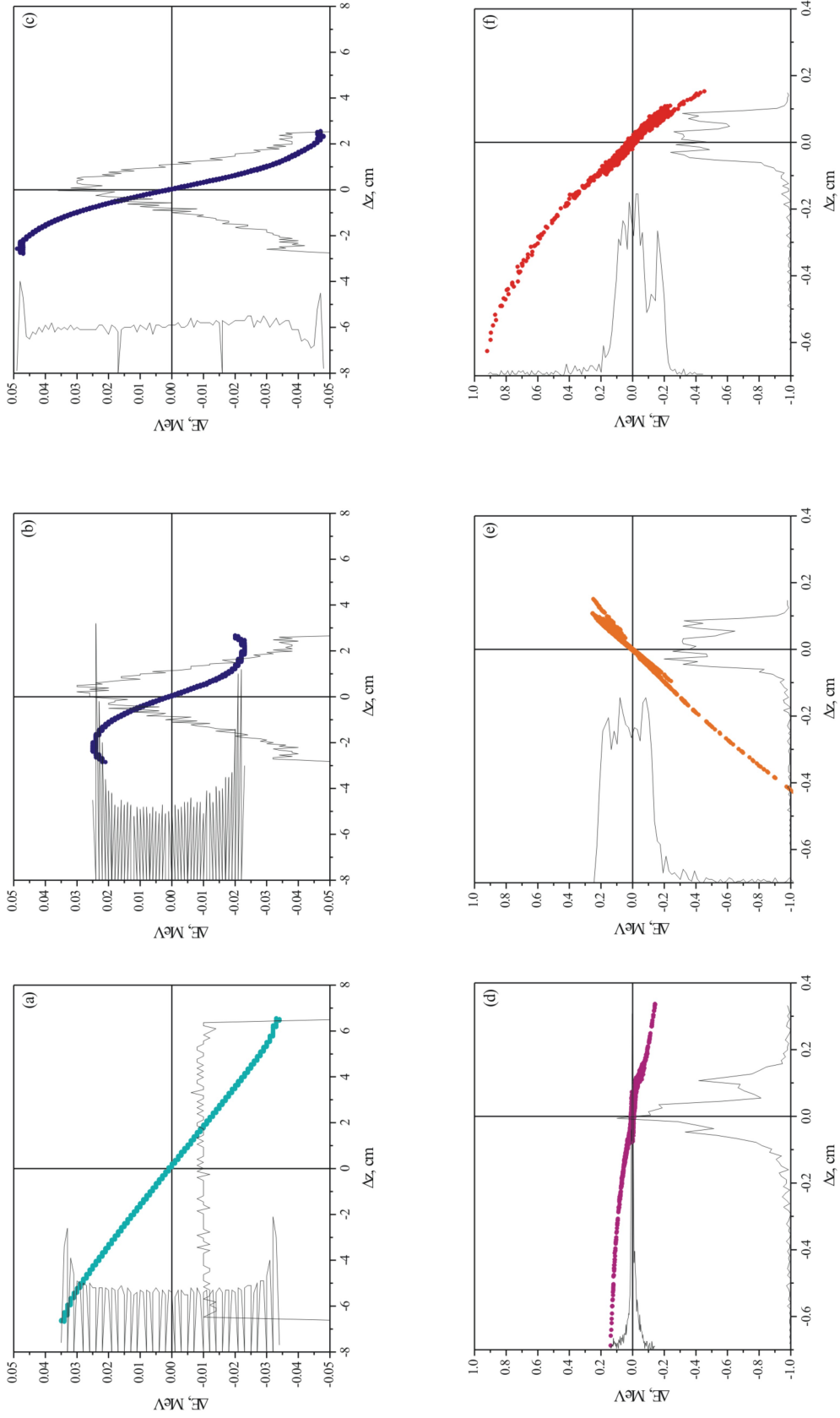wnstream of the cavity #1. Figure 3.3 (d) shows the longitudinal phase space in the first cell of the cavity #1, while Figure 3.3 (e) shows the phase space at the cavity #1 exit. The phase of the RF field at the moment when the electrons come in to cavity #1 is a very critical parameter for the bunch length. Contrarily, the cavity #2 phase variation does not influence the bunch length significantly since the electrons are relativistic already. Running cavity #2 off-crest one can introduce correlated energy dependence from the longitudinal coordinate within the bunch. This has to be done for the further bunch compression by the magnetic chicane in the FEL beamline. The longitudinal phase space at the cavity #2 exit is shown in Fig. 3.3 (f).

During commissioning of the accelerating module we have concentrated our efforts mainly on the bunch length measurements as a function of the cavity #1 phase. The measurements were performed for different values of the bunch charge.

3.3   Bunch length measurements in the injector

To provide optimal evolution of the longitudinal phase space in the accelerating module and between the module and the FEL undulator, the bunch length and the energy spread in the injector have to be optimized. In the early stage of the ELBE injector commissioning the bunch length and the energy spread were measured with the help of a special diagnostic module. The module was installed directly at the injector end at the future location of the accelerating module. The module consists of a dipole and a transversal RF kicker cavity [3.3]. The dipole bends the beam vertically. The RF kicker cavity is running in the dipole TM_{011} mode at 1.3 GHz so that it modulates the horizontal momentum of the electrons within an electron bunch. Therefore in the dispersion region behind the dipole a beam profile, measured with a view screen, carries information about the beam energy spread and the bunch length simultaneously. The injector was commissioned and characterized with the help of the diagnostic module [3.4]. When the accelerating module was installed the diagnostic one could not be used and another technique was necessary for the bunch length measurements.

The idea of the bunch length optimization is very simple. The bandwidth of an electrical signal is inversely proportional to the signal width in the time domain. The bandwidth depends also on the signal shape. Under assumption that the shape of the bunch does not change significantly, a larger amplitude of a higher frequency component corresponds to a shorter bunch. That means that the observation of the beam spectrum can be used for the bunch length diagnostic. Observation of the entire beam spectrum is not the optimal way, since the resolution of any RF measurement depends on the measurement bandwidth. To make the measurements more precise one should reduce the bandwidth. The measurements' central frequency has to be optimized as well. The measurements should be done at high frequencies where the beam signal change is larger. On the other hand, one should remember that at a higher frequency many details of the beam detector design could cause the detector response to be different from the theoretically predicted one.
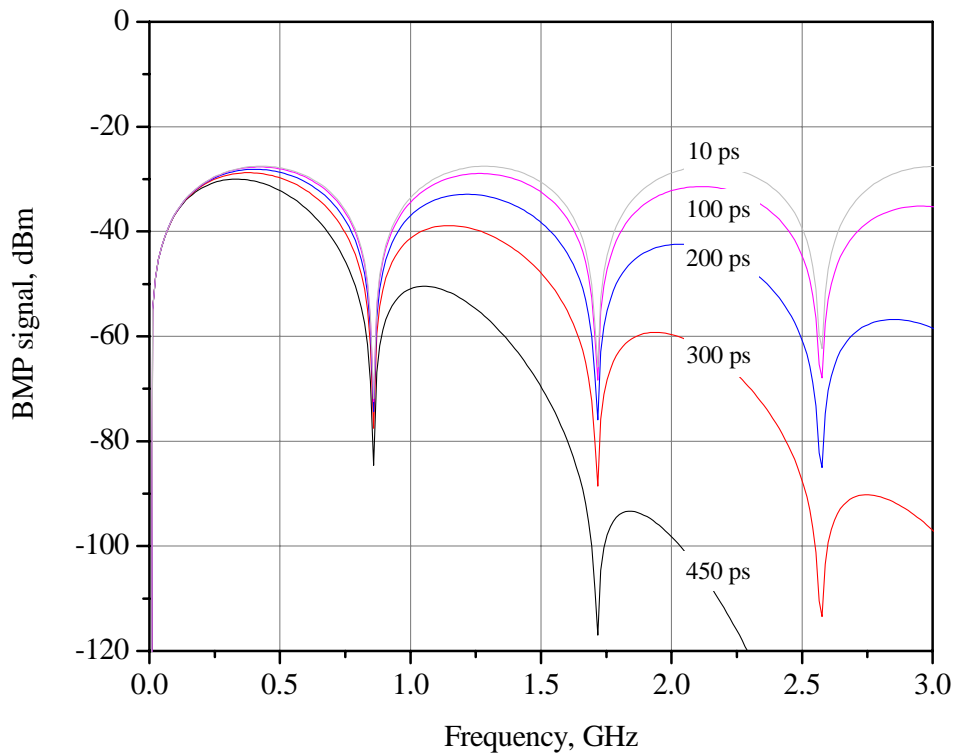
Figure 3.4 The ¾λ BPM signal with different RMS bunch lengths

At the end of the injector a stripline beam position monitor (BPM) is installed. Operation and design of the BPM is described in detail in the next chapter. The BPM is a broadband detector, with bandwidth spreads up to several GHz. The ¾λ BPM signal in the frequency domain, calculated for different values of the RMS bunch length, is shown in Fig. 3.4. The BPM is designed to have the response maximum at 1.3 GHz. This is the second maximum of the BPM response. The calculations are done for a Gaussian longitudinal bunch profile with RMS bunch length of 450 ps, 300 ps, 200 ps, 100 ps and 10 ps. As can be seen in Fig. 3.4 the BPM signal at 1.3 GHz rises about 30 dB when the bunch is compressed from 450 ps down to 10 ps. The BPM is designed to operate mainly at this frequency, so the behavior of the BMP at the 1.3 GHz is well understood and predictable. The frequency of 1.3 GHz is close to the inverse bunch length of 450 ps. This is why it should be easy to distinguish a 450 ps long bunch from the 10 ps one. But the resolution of such measurements depends on the bunch length, so that the method cannot distinguish between the 10 ps bunch and, for example, a 30 ps one. The main point of the optimization of the longitudinal phase space in the injector is minimization of the length of the bunch injected into the accelerating module, since this results in the minimum energy spread of the accelerated beam and therefore the minimum of the longitudinal emittance. There are four knobs to influence the bunch length at the end of the injector. These are the phase and the amplitude of the RF field in the two buncher cavities. Primarily the first subharmonic buncher operating at 260 MHz influences the bunch length. That means it is most important to find the proper phase and amplitude for the buncher.

Figure 3.5 The signal of the stripline BPM placed at the end of the injector as a function of the subharmonic buncher phase

Figure 3.6 The signal of the stripline BPM placed at the end of the injector as a function of the subharmonic buncher incident RF power

The power of the 1.3 GHz component of the BPM signal was measured as a function of the subharmonic buncher phase and the buncher gradient. The maximum of the BPM signal corresponds to the m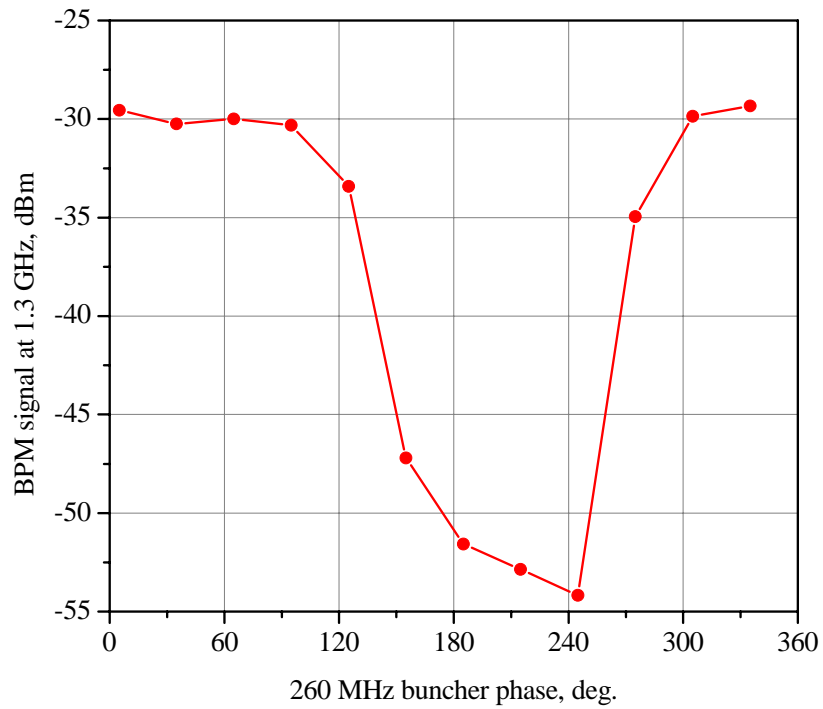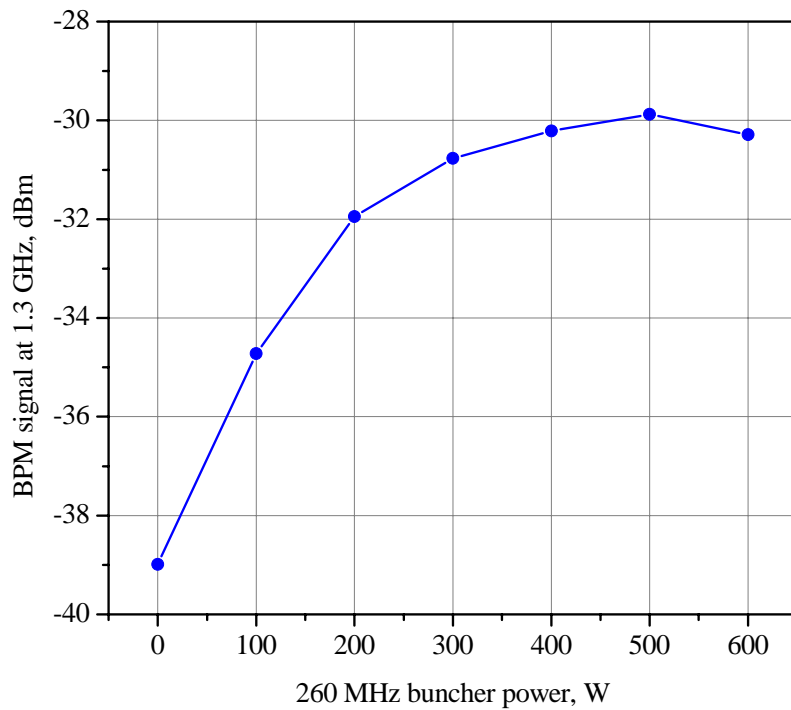inimum bunch length. The first time the measurements at ELBE injector were done when the diagnostic module was not yet removed and the crosscheck measurements were possible. The measurements of the bunch length with the help of the BPM are in very good agreement with the measurements with the transfer kicker cavity. The measured BPM signal as a function of the buncher phase is shown in Fig. 3.5. The dependence of the signal from the buncher incident power is depicted in Fig. 3.6. Thus for those setups the maximal bunch compression was achieved at a buncher phase of 5° and incident RF power of 500 W.

The bunch compression measurements in the injector with the BPM are the first and necessary step in the optimization of the electron beam longitudinal emittance. Final adjustments of the injector elements influencing the longitudinal emittance should be made when the bunch length and the energy spread are measured with the accelerated beam after the module.

3.4   The method of bunch length measurement using coherent transition radiation

3.4.1 Transition radiation from a single charged particle

At first let us consider the phenomena of transition radiation (TR) for a single charged particle. When a charged particle crosses a boundary of two media with different dielectrics or magnetic constants, transition radiation is produced [3.5]. Consider the particular case when an electron crosses the boundary of vacuum and a metal. The metal is thought to be a perfect conductor; this is a very good approximation for frequencies less than the plasma frequency of the metal ω_p. Thus when the electron crosses the surface, conducting electrons in the metal move so that the electrical field of the electron gets screened. For an observer outside the metal this event looks as if the electron "suddenly" disappears. In this case "suddenly" means that the characteristic time of the process $\tau_{transition}$ is much less than the inverse frequency of the emitted radiation $1/\omega_{radiation}$, i.e., $\tau_{transition}\omega_{radiation} << 1$. The characteristic time $\tau_{transition}$ is a measure of how fast the conducting electrons, considered as a collective, can reposition. In fact this is the inverse plasma frequency of the metal. Thus for a radiation with $\omega_{radiation} << \omega_p$ the expression "suddenly" is true, and we can think that the response time of the TR is zero. This is a very important property of the TR which is used for the bunch length measurements. Because of this fact, the longitudinal profile of the transition radiation pulse made by an electron bunch is a copy of the longitudinal bunch profile.

One can describe the process of the TR more rigorously as follows. The electromagnetic field of the electron, approaching the metal surface in vacuum can be described as a sum of the electron's field and the field of its image particle. The image particle moves in the metal so that the boundary conditions on the surface are satisfied. Then the crossing of the boundary looks like annihilation of the electron and the image particle. The generated transition radiation can be described analogically to

the bremsstrahlung radiation [3.6]. The spatial distribution the emitted radiation can be written as

$$\frac{d^2W}{d\Omega\,d\omega} = \frac{e^2}{4\pi^2 c^3}\left|\sum\left(\frac{[\vec{V}_f \times \vec{s}]}{1-\frac{(\vec{s}\cdot\vec{V}_f)}{c}} - \frac{[\vec{V}_i \times \vec{s}]}{1-\frac{(\vec{s}\cdot\vec{V}_i)}{c}}\right)\right|^2,\qquad (3.1)$$

where e is the electron charge, c is the speed of light, $\vec{s} = \dfrac{\vec{k}}{|k|}$ and $\vec{k}$ is the wave vector of the TR, $\vec{V}_f$ and $\vec{V}_i$ are the velocity vectors after and before the event, respectively. The sum in Eq. (3.1) is taken over all particles taking part in the interaction; in our case these are the electron and the image particle. Assume the electron is relativistic; this is normally the case of interest. If the electron hits the surface with an angle ψ_0 in respect to the surface normal, then the generated TR is concentrated around the angle $-\psi_0$ as a double cone with maximum intensity at $-\psi_0 \pm 1/\gamma$, where γ is the relativistic Lorentz factor. A thin metal foil is used very often to generate the TR for electron beam diagnostic purposes. Figure 3.7 shows one of the possibilities. The thin foil is oriented 45° degree with respect to the beam direction. The TR generated on the front surface of the foil propagates perpendicular to the beam direction. The transition radiation is also generated on the rear surface of the foil and propagates collinear with the beam. The radiation distribution calculated according to Eq. (3.1) is also shown in Fig. 3.7. The calculation is made assuming an electron energy of 12 MeV. The same intensity distribution but in more detail is depicted in Fig. 3.8. The radiation is peaked at the angles of 90°±2.44° as was mentioned above. One more point to note is that the total energy of the transition radiation is proportional to γ^2, this fact makes the use of the radiation difficult at low energy. Now we consider the process of the TR not for a single electron but for a very big number of electrons, i.e., an electron bunch.

3.4.2 Transition radiation of an electron bunch

If an electron bunch consisting of N_e electrons crosses the boundary of vacuum and a metal, each electron of the bunch generates the TR. For a wavelength shorter than the bunch length, the radiation power is proportional to N_e, since for every electron there is an electron radiating in opposite phase and the coherent term equals zero. The transition radiation is very broadband; its part that lies in the optical range of spectrum is called optical transition radiation (OTR). The intensity of the OTR is linearly proportional to the current density; this fact makes the OTR a very good instrument for a beam profile measurements. For a wavelength much longer than the bunch length, all electrons radiate almost in one phase and, since the phase difference is constant, the radiation is coherent and therefore the power of the radiation is proportional to N_e^2. This part of the TR radiation is called coherent transition radiation (CTR). Of course, there is a transition region when the spectral power density goes from N_e to N_e^2.
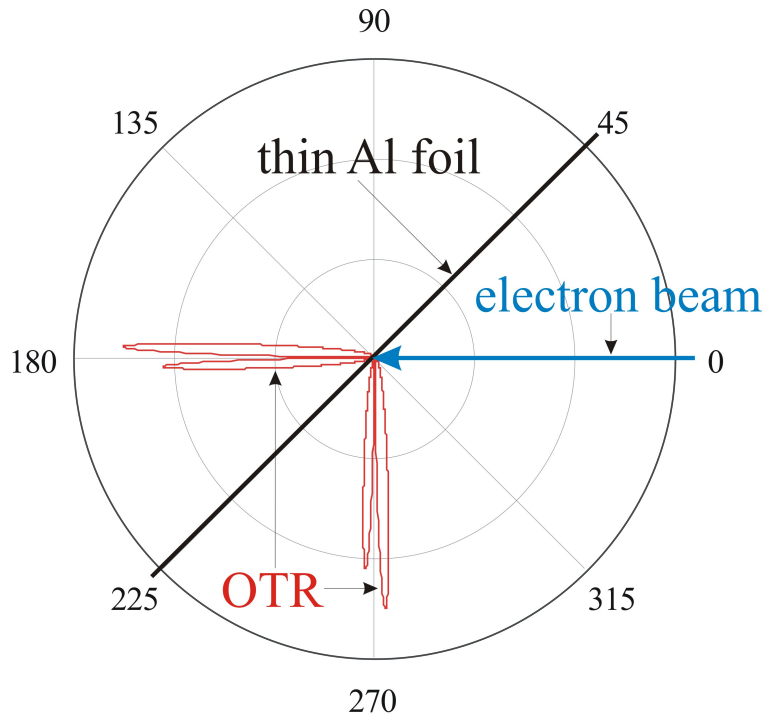
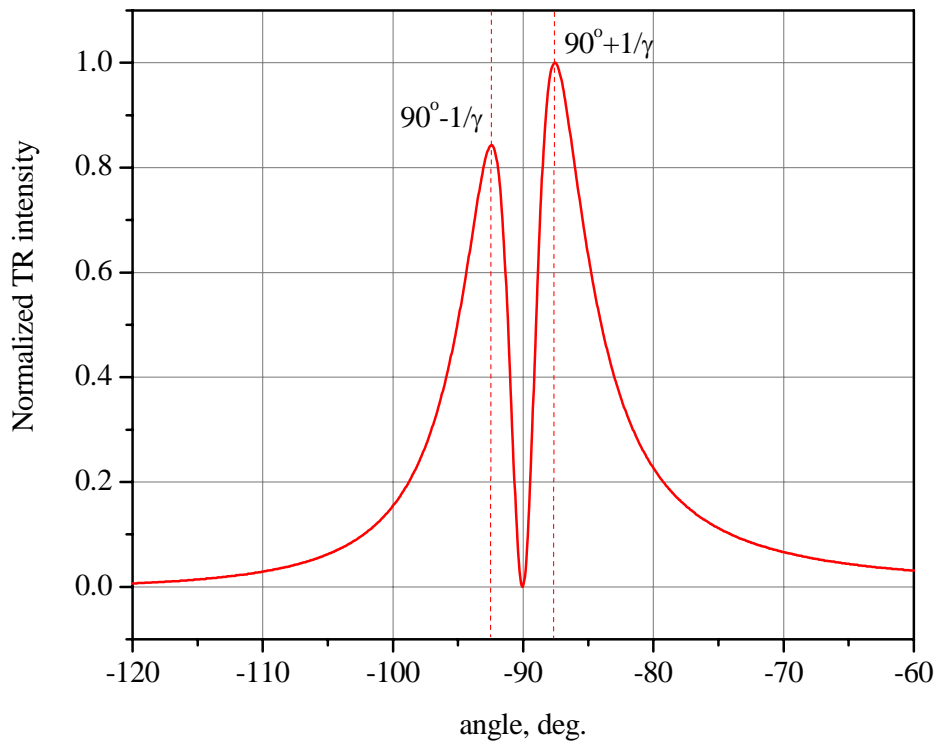*Figure 3.7 Generation of the OTR on a thin aluminum foil*

Figure 3.8 The calculated angular distribution of the TR generated on the foil oriented 45° to the beam direction by 12 MeV electrons

Obviously, the position of this transition depends on the bunch length; hence measurements of the transition radiation spectrum can give information about the bunch length. As was already mentioned in Chapter 1, for the ELBE FEL bunch charge of 77 pC N_e is about 4.8×10^8. As a consequence almost all power of the transition radiation is in the coherent part.

To describe the dependence of the TR spectrum from the bunch length quantitatively one calculates the electrical field of the TR from the entire bunch as a sum of the fields radiated by separate electrons and then calculates the radiation intensity as the square of the field. Following [3.7] we denote the field radiated by a single electron as $E_S(\vec{r},t)$, where dependence on the coordinate is given by Eq. (3.1) and the time dependence is the Dirac delta function related to the temporal moment when the electron passes the surface. Then the field of the bunch is written as

$$E_b(\vec{r},t) = \sum_k E_{Sk}(\vec{r},t - \tau_k)$$ (3.2)

where the sum is taken over all electrons of the bunch and τ_k indicates the time when the kth electron radiates the TR. The Fourier transform of Eq. (3.2) is

$$\tilde{E}_b(\omega) \propto \sum_k \tilde{E}_{Sk}(\omega)e^{i\omega\tau_k} .$$ (3.3)

At this point it is convenient to calculate the power spectrum of the bunch TR, which gives the following

$$P_b(\omega) = \tilde{E}_b(\omega)\tilde{E}_b^*(\omega) = \sum_k \sum_j \tilde{E}_{Sk}(\omega)e^{i\omega\tau_k} \tilde{E}_{S\,j}^*(\omega)e^{-i\omega\tau_j} .$$ (3.4)

Since the power spectrum of a single electron is $P_S(\omega) = \tilde{E}_S(\omega)\tilde{E}_S^*(\omega)$ Eq. (3.4) can be rewritten as following

$$P_b(\omega) = P_s(\omega)\left(N_e + \sum_k \sum_{j \neq k} e^{i\omega(\tau_k - \tau_j)} \right).$$ (3.5)

Because we deal with a very big number of electrons displaced from each other on a distance much smaller than the bunch length, the summation can be replaced by an integral. Introducing a normalized distribution function of the longitudinal bunch density $f_b(t)$, one can rewrite the sum as [3.7]

$$\sum_k e^{i\omega\tau_k} \equiv N_e \int f_b(t)e^{i\omega t}dt = \tilde{f}_b(\omega).$$ (3.6)

Analogously replacing the double summation in Eq. 3.5 one gets the expression showing the dependence of the bunch power spectrum from the bunch length in the following form

$$P_b(\omega) = P_S(\omega)\left[N_e - N_e(N_e + 1)\left|\tilde{f}_b(\omega)\right|^2 \right].$$ (3.7)

For frequencies much higher than the bunch spectrum the second term is zero and the power of the transition radiation is proportional to the number of the electrons in the bunch, i.e., to the beam current. This is the optical transition radiation. For wavelengths longer than the bunch or frequencies small in comparison to the bunch characteristic frequency, the $\left|\tilde{f}_b(\omega)\right|^2$, called *bunch form factor*, is approaching unity so that the spectral power density is proportional to N_e^2 as was expected and is discussed above. Thus from the power spectrum measurements one can gain an information about the electron bunch length.

3.4.3 The Martin-Puplett interferometer

   As we saw in the beginning of this chapter the electron bunch length of an accelerated beam at ELBE is in the picosecond range. One picosecond corresponds to a wavelength of 0.3 mm and to a frequency of one terahertz. Therefore for a bunch length measurement, with a technique utilizing the CTR, the spectral measurements have to be done in the sub-millimeter and millimeter wavelength range.

   The Martin-Puplett interferometer (MPI) [3.8, 3.9] is a modification of the Michelson interferometer. Sometimes it is also referred to as a polarizing version of the Michelson interferometer. In both cases the interference takes place between two beams passed through different optical path lengths. To begin with, we consider operation of two important millimeter-wave optical elements. These are the wire grid and the roof mirror.

   In the listed wavelength range a wire grid can be used very efficiently as a polarizer and as a beam splitter as well. The wire grid is an array of stretched parallel metal wires placed close to each other. The diameter of the wires and the grid period are chosen to be much smaller than the wavelength. The wire length is much longer than the wavelength of the interest. Consider a plane polarized electromagnetic wave coming to the grid with the electrical field oriented along the wires. Such a wave will excite well an image current along the wires as if the grid were a metal mirror. Consequently the grid will reflect the wave. A wave with the electrical field perpendicular to the wires cannot excite the image currents so effectively. For this reason the wave polarized perpendicular to the wires will pass through the grid. Since any wave with arbitrary polarization can always be considered as a sum of two plane polarized waves with orthogonal polarizations and with a proper phase difference, it is clear that the wire grid will act as a polarizer on an electromagnetic wave, i.e., let thought only one component. Of course the wavelength of the wave must be in the listed range. In the case when the incident wave with amplitude E_o is plane polarized so that the angle between the wires and its electrical field is θ_0, the field with the amplitude of $E_o \, sin(\theta_0)$ will be transmitted and the grid will reflect the field with the amplitude of $E_o \, cos(\theta_0)$. If the angle θ_0 is 45° the grid wire transmits and reflects the same amount of the field, that is, $E_o / \sqrt{2}$ and therefore works as a 50-to-50 beam splitter. The power reflectivity for the component polarized parallel to the wires is given as

$$R_{//} = \frac{1}{1 + \left(2S/\lambda\right)^2 ln\left(S/\pi d\right)^2} \tag{3.8}$$

and the transmission for the component polarized perpendicular to the first one as

$$T_{\perp} = \frac{\left(\pi^2 d^2\right)^2}{\left(2\lambda S\right)^2 \left(1 + \left(\pi^2 d^2\right)^2 / \left(2\lambda S\right)^2\right)} \tag{3.9}$$

where d is the wire diameter, S is the wire grid period and λ is the wavelength [3.9].

   Another important element for the MPI operation is the so-called roof mirror. It consists of two plane mirrors assembled so that their surfaces are perpendicular to each other. The line where the mirrors are attached is called the roof line. The most important property of the roof mirror is that it changes the polarization direction upon the reflection. Imagine the roof mirror with the roof line aligned vertically. Let the incident wave be plane polarized and let ϕ be the angle between the polarization

plane and the vertical. The incident and the reflected waves have the electrical field arranged so that they satisfy the boundary conditions on the mirror surface. Thus the vertical component of the electrical field alters for 180° degree under each reflection and since this happens twice in the roof mirror this component has the same direction in the reflected wave. The horizontal component of the electrical field alters by 90° under each reflection and after two of them within the roof mirror alters by 180°. As a result the polarization of the reflected wave will be tilted at angle $-\phi$ to the vertical. Hence, the roof mirror turns the polarization angle for 2ϕ. Choosing ϕ equal to 45° one can manage to have the roof mirror to change the plane polarization to the orthogonal one.

  Figure 3.9 illustrates the operational principle of the Martin-Puplett interferometer. At first, a beam coming into the MPI is polarized. Assume for the sake of discussion, that the vertical polarization is transmitted by the polarizer. Then another grid with wires oriented 45° to the vertical splits the beam in two waves with equal amplitude and with polarizations tilted ±45°. These two beams are reflected back to the beam splitter by two roof mirrors with the vertically oriented roof line. The polarization of the two beams is changed by 90° on the roof mirrors. The component reflected by the splitter earlier now will be transmitted and the transmitted one in the beginning will be reflected. So the beam splitter works as the beam combiner as well. Note that the two beams originated from a single one and, for this reason, are coherent, and we have to add their electrical fields. If the two arms of the interferometer have different path lengths the two beams will be combined with some phase difference. As a consequence the recombined beam has, generally speaking, elliptical polarization. It is interesting that the total beam power detected at this point is the same as we have at the MPI input. The effect of the path length difference of the two beams is the change in the polarization state of the recombined beam. To detect the change, one has to measure independently the power of the orthogonal polarized components. In the MPI it is done using one more polarizer (analyzer), which transmits one polarization to first detector and reflects the orthogonal one to second detector. One of the roof mirrors is moveable so that the path difference is introduced in a controllable way.

  Let $E_{in}(t) = E_0 g(t)$ be the longitudinal profile of the field transmitted by the first polarizer, where E_0 is a constant. The beam splitter reflects to one roof mirror $\sqrt{R_{\parallel}/2}\,E_0 g(t)$ of that field and transmits $\sqrt{T_{\perp}/2}\,E_0 g(t)$ to the second one. The path length difference of ΔL in the two arms of the interferometer corresponds to a time delay of $\tau = \Delta L/c$. It is assumed that the path of the second beam is longer. Then for the recombined beam field one can write

$$E_{out}(\tau) = \sqrt{T_{\perp} R_{\parallel}/2}\, E_0 \big(g(t) + g(t-\tau)\big). \tag{3.10}$$

The detectors used in the Martin-Puplett interferometer sense the radiation intensity. The detector signal as a function of the time delay τ can be written as follows

$$U(\tau) = \left(E_o^{\,2} T_{\perp} R_{\parallel}/2\right)\int\limits_{-\infty}^{+\infty}\left((g(t))^2 + g(t)g(t-\tau)\right)dt \tag{3.11}$$

where we have used the fact that $\int\limits_{-\infty}^{+\infty}(g(t))^2\,dt = \int\limits_{-\infty}^{+\infty}(g(t-\tau))^2\,dt$. The first term under the integral in Eq. (3.11) does not depend on the delay and represents a constant offset, which is actually proportional to the incident power. The second term is the *autocorrelation function* of the longitudinal field profile. The Wiener-Khintchine
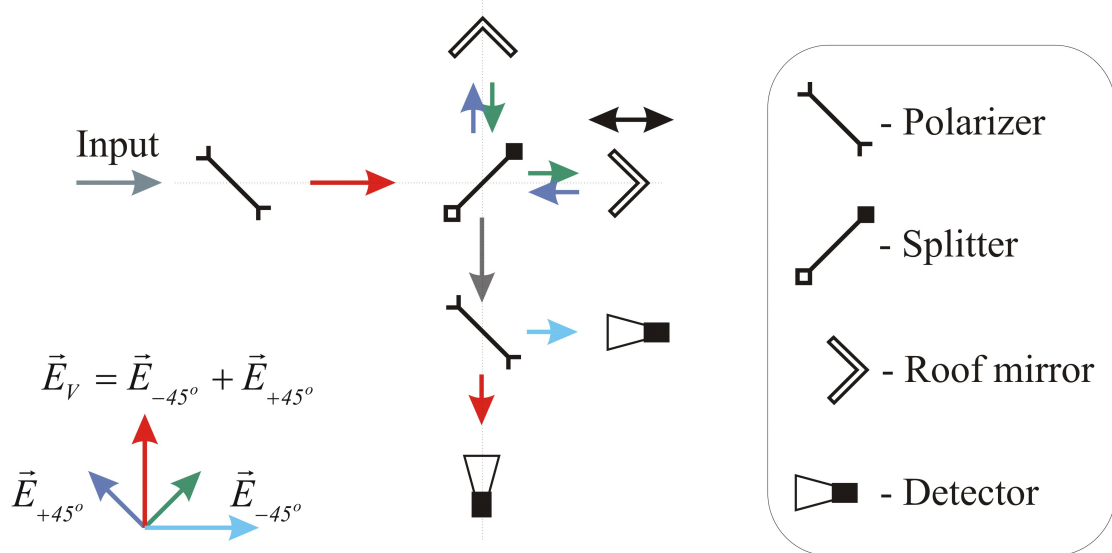
$$\vec{E}_V = \vec{E}_{-45^o} + \vec{E}_{+45^o}$$

$$\vec{E}_{+45^o} \qquad \vec{E}_{-45^o}$$

Figure 3.9 Diagram of a Martin-Puplett interferometer

theorem [3.10, 3.11] states that the Fourier transform of the autocorrelation function is the power spectrum.

The essence of the bunch length measurement technique utilizing coherent transition radiation is the following. Since the response time of the transition radiation is zero, the time profile of the CTR is a copy of the electron bunch longitudinal profile. The Martin-Puplett interferometer is used to measure the autocorrelation function of the CTR pulse. The power spectrum and the bunch length information is obtained by Fourier transforming the measured autocorrelation function. There are different approaches for obtaining the bunch length from the MPI measurements. The data can be evaluated in the time domain [3.12] as well as in the frequency domain [3.7, 3.13]. The method of data evaluation we have used is a frequency domain method; its details are explained in the next sections.

3.5   Experimental setup for the CTR measurements

An aluminum foil as thin as 10 μm, stretched to a frame, was used to generate the CTR. The foil is oriented 45° to the beam direction. Thus the backward CTR part is propagating almost perpendicularly to the electron beam. We have used a z-cut crystal-quartz window for the output of the CTR from the beam line.

A Martin-Puplett interferometer is used to measure the autocorrelation function of the CTR pulses. A parabolic aluminum mirror with a focal distance of 200 mm is used to transform the divergent transition radiation into a quasi-plane wave, which then goes to the interferometer. Wire grids are used as polarizers and as beam splitters in the interferometer. The grids are made of gold covered tungsten wires, with diameter of 20 μm. The grid period is 100 μm. Another parabolic mirror at the output of the interferometer focuses the radiation on the input windows of the detectors. The MPI used at ELBE for the bunch length measurements was built in collaboration of the University of Aachen, the Fraunhofer Institute für Produktionstechnik in Aachen and the physics institute of the RWTH in Aachen. The interferometer is a copy of the interferometer originally built for the TESLA Test Facility (TTF) at DESY. The interferometer at TTF was successfully used for beam characterization [3.14].

Pyroelectric detectors were used for the measurements at TTF. However, it was found that the detector has strong oscillations in its frequency response. This is extremely undesirable, since it has a serious impact on the bunch length reconstruction. For this reason we have modified the MPI and have used two Golay cell detectors for the measurements.

The detector was developed first in 1947 by Golay [3.15, 3.16]. The Golay cell is a pneumatic detector. The main part of the detector is a chamber with compressed gas. One wall of the detector is an infrared transparent window. A flexible membrane is a part of another wall of the chamber. An efficient infrared absorber is placed inside the chamber. Infrared radiation directed into the chamber heats the absorber, which in turn heats the gas in the chamber via convection. Since the volume of the chamber is constant, the rise of the temperature leads to pressure increase, which results in a deformation of the membrane. The deformation is detected by a simple optical system. More details on the Golay cell operational principle can be found in [3.17].

The moveable mirror is mounted on a linear motor stage, driven by a step motor so the mirror position could be controlled very precisely. The minimum step size of the stage is 2.5 μm. Usually, for a bunch length measurement interferometer scans with steps of 25 μm were made. The step motor is computer controlled via the Local Area Network. The two signals from the Golay cells are fed to ADCs with differential inputs. The ADCs are PCI card based and are installed in the same computer. The bunch length measurements with the MPI were automated. The automation software is written in LabVIEW. The results of the measurements are presented and discussed in the next section.

3.6   Experimental results

3.6.1 Linearity of the detectors

The bunch length measurements were made in the diagnostic beam mode, when the electron beam is macropulsed and the average beam current is 1 μA in order of magnitude. We also have used the ability of the RF system to run the accelerator with a reduced bunch frequency with respect to the standard one, which is 13 MHz. The Golay cell is a relatively slow detector with a response time of milliseconds in order of magnitude. The macropulse length in the bunch length measurements was in the same range. Thus the Golay cell works as an integrator measuring the average CTR power within a macropulse. The macropulse period was chosen to be much longer then the Golay cell relaxation time. Figure 3.10 shows the response of the two Golay cells installed on the MPI to a single macropulse. The amplitude of the signal was taken as a measure of the average CTR power. The two Golay cells used in the measurements are not identical. To make sure that the signal amplitude is truly proportional to the incident power, the amplitude was measured as a function of the macropulse length keeping all others beam parameters the same. The results of the measurements are shown in Fig. 3.11 with a linear function best approximating the data. Golay cell #2 has a linear response in the whole range of the measurements. Golay cell #1 has its response linear only up to a macropulse length of 1.5 ms, which corresponds to the Golay cell signal maximum of 1.6 V. Therefore in the all following measurements we kept the incident CTR power in the range where both detectors are linear, i.e., the maximum of the Golay #1 signal may not exceed a level of 1.6 V.
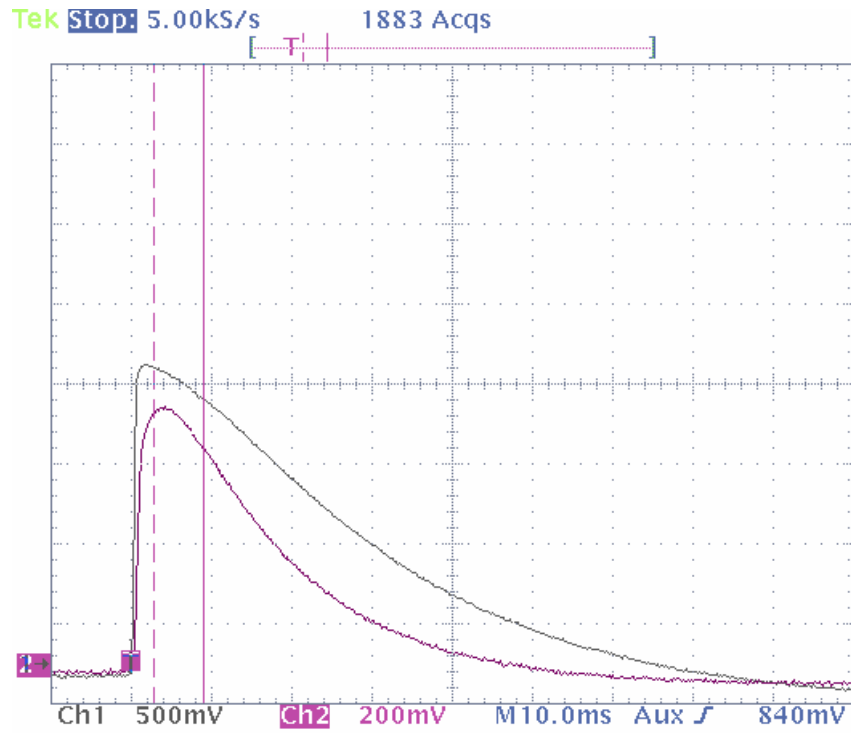
Figure 3.10 The signals of the two Golay cells of the Martin-Puplett interferometer – response to a macropulse
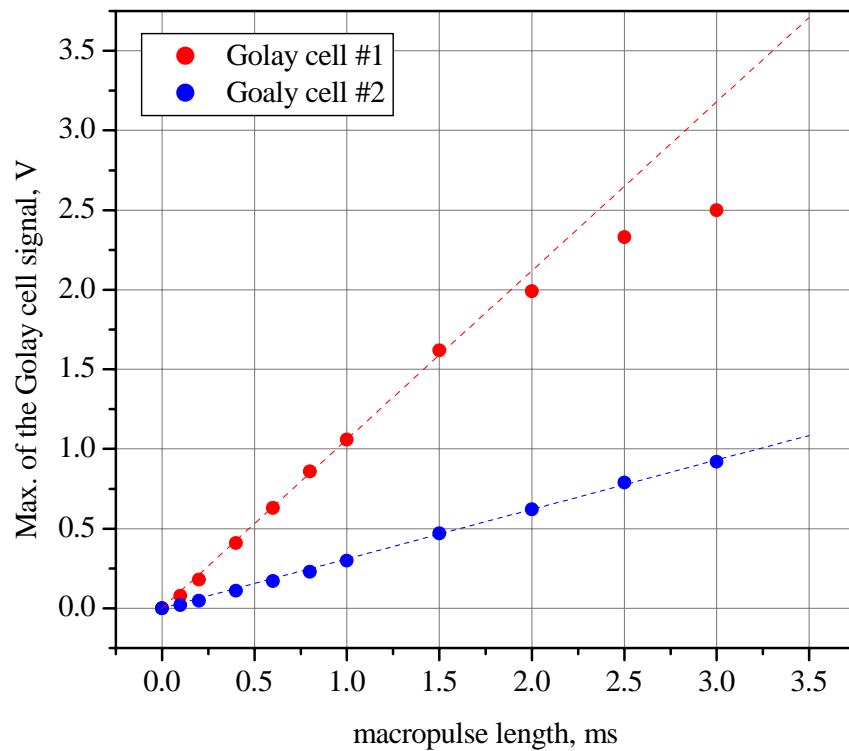

Figure 3.11 Linearity of the Golay cell detectors

3.6.2 Initial data evaluation

A typical result of the interferometer scan is shown in Fig. 3.12. The scan is made with mirror steps of 25 μm and the entire scan range is 5mm. The choice of the scan range is a compromise between a moderate time for measurement and the amount of the data needed for the bunch length reconstruction. We have to use a Fast Fourier Transformation (FFT) to obtain the power spectrum from the measured autocorrelation, since the measurement data is discrete. The power spectrum is also discrete with a frequency resolution of $\varDelta f = \dfrac{f_s}{N_m}$, where f_s is the sampling frequency and N_m is the number of measured points. The mirror step $\varDelta x$ of 25 μm corresponds to the double pass length change of 50 μm and to the sampling frequency of 6 THz. The interferogram contains 200 points giving the spectral resolution $\varDelta f$ of 0.03 THz. The spectrum given by FFT spreads from zero to the sampling frequency but consists of two symmetric parts; one of them stands for the negative frequencies. Thus the meaningful spectrum spreads from zero to $\dfrac{f_s}{2}$, which is 3 THz for our measurements.

The first step in the data procedure is the detector normalization. This is necessary because the detectors are not equal, as was mentioned. The following assumptions were used for the normalization. If the detectors were identical then the mean value of the data taken by the detectors will be equal, this follows from the symmetry of the interferometer with respect to a 90° polarization change. The second assumption is that the modulation depth, i.e., the difference in the maximum and minimum will be equal as well, since the sum of the two signals must be constant. The normalized data contains both the coherent part and the noncoherent part. We understand by coherent here that when one signal goes up the second one goes down. Noncoherent means that both signals either grow or decrease. The noncoherent part can be given by any instability in the experimental setup. In an ideal case taking the difference of the two normalized signals will cancel the noncoherent part. Practically, the noncoherent part is not canceled completely but gets substantially reduced. The normalized difference is depicted in Fig. 3.13 for the raw data shown in Fig. 3.12.

The autocorrelation function of a positive definite function is a positive definite function as well. This follows directly from the definition of the autocorrelation. The longitudinal density of the electrons is, of course, a positive function and one would expect the autocorrelation to be also positive. The two well-seen minima on the interferogram are explained by the low frequency cut off, which comes from the diffraction losses on the Golay cell input window. Symmetry is another feature of the autocorrelation function given by its definition. As one can see the measured interferogram is not symmetric. The interferograms obtained in all our measurements have approximately the same degree of nonsymmetry. A small misalignment of the interferometer is believed to be responsible for that. The Fourier representation of the nonsymmetrical autocorrelation is complex. The imaginary part of the representation comes from the nonsymmetry and is not related to the bunch length or to the bunch shape. For this reason, in calculating the power spectrum of the bunch we have used only the real part of the FFT representation. There are several examples of the calculated bunch spectra shown in Fig. 3.14. The measurement data is represented by dots.
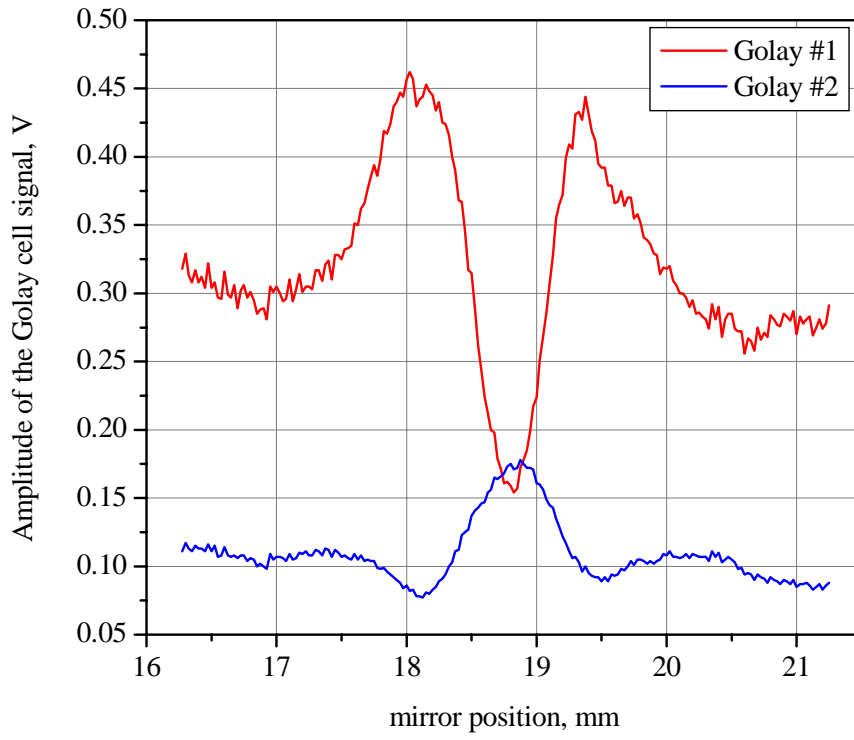
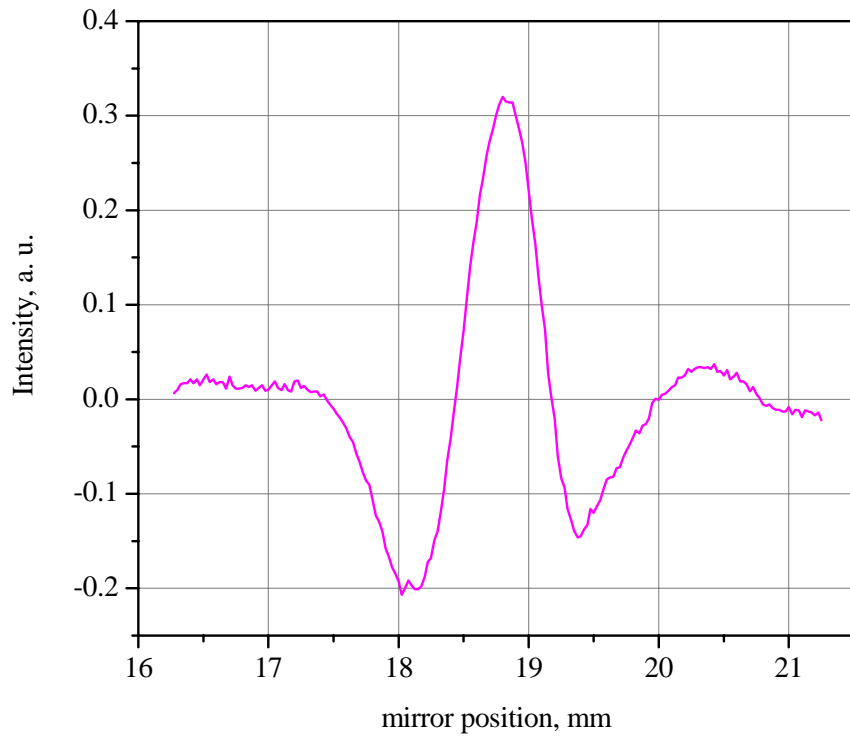*Figure 3.12 The raw data obtained with the Martin-Puplett interferometer*

Figure 3.13 Interferogram – the normalized difference of the detectors signals
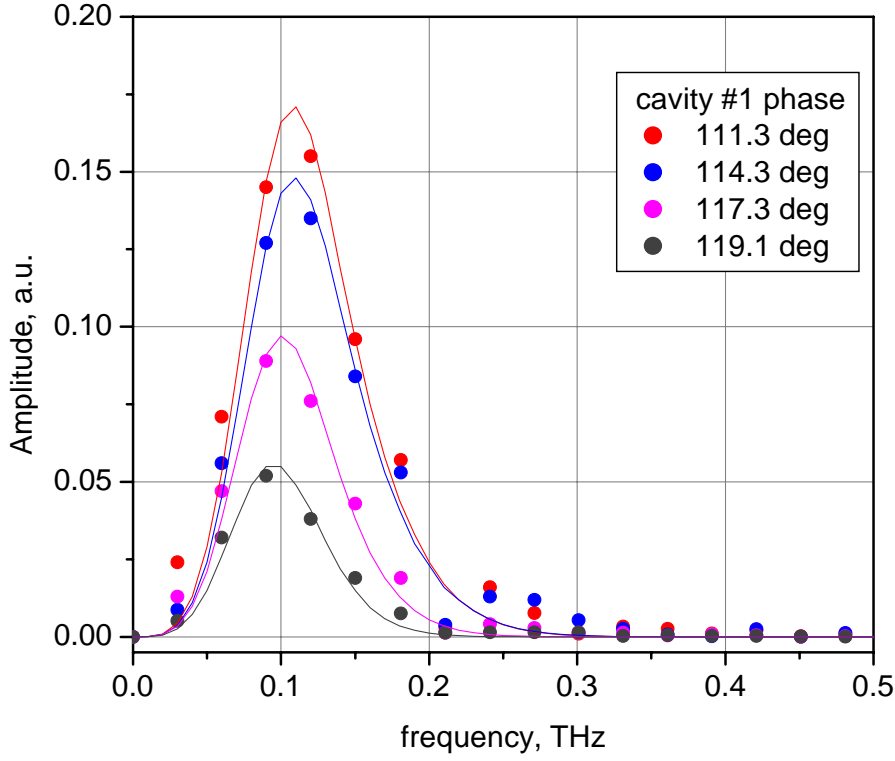
Figure 3.14 The measured beam spectra and the corresponding fit functions to determine the bunch length

3.6.3 Bunch length reconstruction

The power spectrum defines uniquely the amplitude of the components of the frequency domain representation of the pulse. But information about the relative phases of the different components is lost in the interferometric measurement. This is why a direct pulse shape reconstruction from the power spectrum is not possible.

The general idea of obtaining the bunch length information from the MPI measurements is the following. First the power spectrum of the bunch is calculated using only the real part of the FFT representation of the measured interferogram. An assumption is made on the bunch shape and the power spectrum of the hypothetical bunch is calculated. A filter function, responsible for the low frequency cut off, is used in this calculation. Parameters of the hypothetical bunch shape are chosen so that its "filtered" power spectrum fits well to the experimentally measured spectrum. We have assumed the Gaussian shape of the bunch, that is, $n(t) = \dfrac{Q}{c\sigma_t \sqrt{2\pi}} e^{-\left(\frac{t}{\sigma_t \sqrt{2}}\right)^2}$,

where σ_t is the RMS bunch length and Q is the bunch charge. The Fourier transform of the distribution function is also a Gaussian function and is written as

$\tilde{n}(\omega) = \dfrac{Q}{c\sqrt{2\pi}} e^{-\left(\frac{\omega\sigma_t}{\sqrt{2}}\right)^2}$. Thus we can write the Gaussian bunch power spectrum as

$$\tilde{P}(\omega) = C\, e^{-(\omega\sigma_t)^2}, \tag{3.12}$$

where C is a constant.

An analytical form was chosen also for the filter function. As was mentioned above diffraction on the Golay cell input window is responsible for the low frequency cut off. The general Huygens' integral can be used to describe the diffraction losses [3.18]. If an aperture with the radius a is illuminated by a plane electromagnetic wave with the amplitude E_0, the field penetrating through the aperture is given in cylindrical coordinates as follows

$$E(r,k,a) = i2\pi N_F e^{-i\pi N_F \left(\frac{r}{a}\right)^2} \int_0^1 \frac{x}{a} E_0 e^{-i\pi N_F \left(\frac{x}{a}\right)^2} J_0\left(\frac{2\pi N_F r}{a}\frac{x}{a}\right) d\left(\frac{x}{a}\right), \quad (3.13)$$

where $N_F = \dfrac{a^2 k}{D}$ is the Fresnel number, k is the wavenumber, D is the distance from the aperture to the plane of observation and J_0 is the zero order Bessel function of the first kind. The intensity of the penetrating wave within a disk of radius R_0 is written as $2\pi \int_0^{R_0} r|E(r,k,a)|^2 dr$. The transmission of the aperture is the ratio of the penetrated intensity to the intensity of the incident wave power within the aperture, this can be written as:

$$T_A = \frac{2}{a^2 E_0^2} \int_0^{R_0} r|E(r,k,a)|^2 dr. \quad (3.14)$$

The Golay cell has an input window with diameter of 5 mm. Unfortunately, the exact dimensions of the chamber with the infrared absorber are unknown and we can only estimate them in order of magnitude. If we suppose that the infrared absorber has a radius of 4 mm and is placed 10 mm from the window then the numerical integration of the Eq. 3.14 gives the transmission shown in Fig. 3.15 by the black line. It is very desirable to have the filter function in a simple analytical form. One criterion of the filter function quality is that it fits well to the diffraction loss curve. Another criterion is that the final frequency domain fit function approximates well the measured power spectrum. The second criterion is much stronger, since the calculated diffraction losses are only an estimate. We have considered two functions as candidates for the filter function, these are

$$F1_{filter}(\omega) = 1 - e^{-(\omega/\omega_0)^2} \text{ and } F2_{filter}(\omega) = 1 - e^{-(\omega/\omega_0)^4} \quad (3.15 \text{ a, b})$$

where ω_0 is the characteristic cut off frequency. The functions are plotted in Fig. 3.15 with the characteristic cut off frequency of 0.1 THz. The function $F1_{filter}(\omega)$ fits well to the diffraction losses curve, but, as a matter of fact, $F2_{filter}(\omega)$ gives much better fits to the measured spectra as shown in Fig. 3.14. Thus the $F2_{filter}(\omega)$ is used as the filter function in the further bunch length evaluation.

The product of the bunch power spectrum, given by Eq. (3.12), and filter function $F2_{filter}(\omega)$ is the frequency domain fit function

$$f_{fit}(\omega) = \left(1 - e^{-(\omega/\omega_0)^4}\right) C e^{-(\omega\sigma_t)^2}, \quad (3.16)$$

used to determine the RMS bunch length, from the data taken with the MPI. The fit function parameters C and σ_t, best approximating the experimental data, were found by means of a nonlinear least square fit. The parameter σ_t is interpreted as the
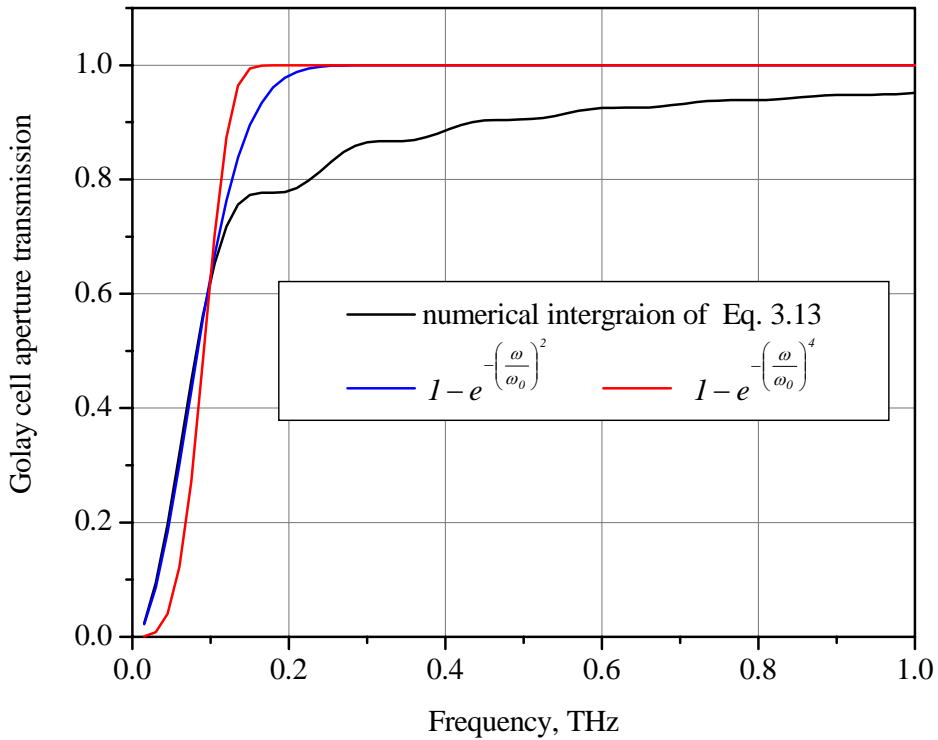
Figure 3.15 Diffraction on the Golay cell aperture and the empirical filter functions

measured RMS bunch length. Figure 3.14 shows the fits corresponding to the data shown on the same figure.

As was already mentioned, the cavity #1 phase plays a very important role in the bunch length evaluation. This is why we have concentrated on the bunch length measurements as a function of the cavity #1 phase. The measurements were done for different bunch charges. The results of the measurements are presented in Fig. 3.16. The measurements are in good agreement with the bunch length predicted by the PARMELA simulations.

3.6.4 Bunch length minimization

One scan with the MPI takes several minutes. We have done about of 20 scans to measure the dependence of the bunch length from the cavity #1 phase for a given bunch charge. Thus the search for a minimal bunch length using this approach takes approximately an hour, even with a fast data evaluation procedure. There is another way to make the bunch length minimization in minutes. The essential principle of this procedure is very close to the one used to minimize the bunch length in the injector and described in Section 3.3. The CTR power within the Golay cell bandwidth is inversely proportional to the bunch length. Thus the maximum of the CTR pulse energy corresponds to the minimum bunch length. The amplitude of the Golay cell signal measured as a function of the cavity #1 phase is depicted in Fig. 3.17. The RSM bunch length measured as explained in this section above is also shown in Fig. 3.17, confirming the above statement.

Observation of the CTR signal gives also the information on the stability of the RF system.
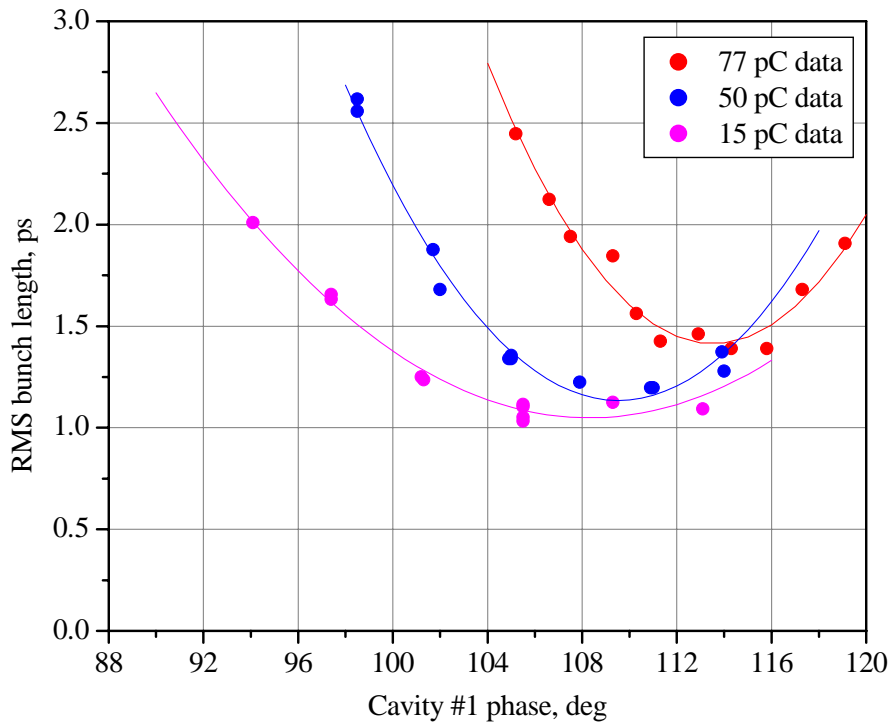
Figure 3.16 The measured dependence of the RMS bunch length on the cavity #1 phase
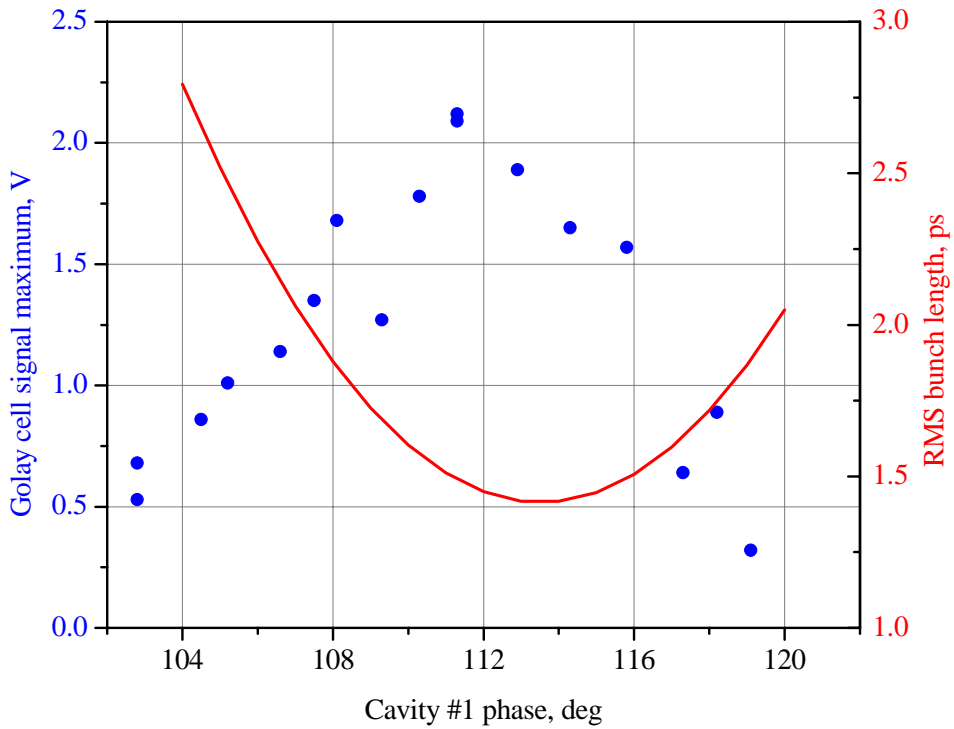

Figure 3.17 The online minimization of the bunch length

In the very first measurements using the Martin-Puplett interferometer, it was detected that the amplitude of the Golay cell signal varies about 20 % from one macropulse to another, when no visible change is made in the accelerator setup. It was found that the reason for the modulation was modulation of the phase of the RF field in the linac. The indication for this was the fact that the Golay signal modulation was correlated somehow to the control signal in the RF phase feedback loop. As the matter of fact, the instability was introduced to the RF system by the noisy environment of the master oscillator [3.19]. The situation was greatly improved by placing the quartz oscillator, first in a heavy lead housing and second in a soft foam-like absorber, which is a good absorber for acoustic waves [3.19].

3.7 Conclusion

The general idea of the electron bunch length evolution for the ELBE FEL was described. The technique of using a beam position monitor to minimize the bunch length in the injector was explained. Results of the bunch length minimization in the ELBE injector using the technique were presented. The measurements are in good agreement with the transverse kicker cavity measurements [3.4]. We have used the Martin-Puplett interferometer to measure the bunch length of an accelerated beam at an electron beam energy of 12 MeV. The method and the experimental setup were described. The procedure proposed for the bunch length derivation from the interferometric measurements in the frequency domain was explained. Results of the measurements with the MPI were presented. The experimental data is in good agreement with the bunch length predicted by PARMELA simulations.

Chapter 4

Beam position monitor system

4.1 Motivation

Overlap of the electron beam and the optical mode of the FEL resonator is a must for FEL operation. Both of them must be placed on the magnetic axis of the undulator. Numerical simulations show [4.1] that the transverse electron beam size in the undulator is about 1 mm. The geometry of the optical resonator, i.e., the curvature radius of its mirrors and the distance between them as well as the FEL wavelength define the size of the optical mode. It is planned to operate the ELBE FEL with the U27 undulator in the wavelength range from 3 μm though 30 μm. The Rayleigh length of the optical resonator is chosen to be 1 m. The size of the optical mode waist in the undulator is given by $W_0 = \sqrt{Z_R \lambda / \pi}$, where Z_R is the Rayleigh length and λ is the wavelength [4.2]. The waist size varies from 0.98 mm to 3.1 mm in the listed wavelength range. Thus one has to make sure that the electron beam position in the undulator is very stable to ensure stable FEL operation. Therefore an accuracy of the electron beam position measurements of 100 μm is required with the assumption that the electron beam and the optical mode have the sizes mentioned above.

There are different sorts of possible beam instabilities. One of them is a long-term drift the others are fast beam oscillations. To be able to detect both of them the beam position measurement system has to be operating online and nondestructive for the electron beam. At the same time beam position measurements should be time resolved. The system has to work in a high average current mode as well as in a diagnostic mode with a macropulsed beam.

We would like to make some remarks on the electron beam position measurements in the undulator. The vacuum chamber in the undulator is very different from the other parts of the beam line. This is done to minimize the undulator gap and by so doing to increase the FEL gain. Because of the special geometry and the space constraints it is very difficult, if possible at all, to place convenient beam position monitors (BPM) inside the undulator. The idea of the beam position control in the undulator is the following. There are two BPMs placed around the undulator, one

upstream and one downstream. One more separate system measures the beam position directly inside the undulator. This is a system of seven precise view screens. The view screens are used for the optical cavity alignment as well, ensuring the overlap of the beam and the optical mode. This system is described in [4.3]. The view screens can be used only in the diagnostic mode when the average current of the beam is very low, 1 μA in order of magnitude. Once the optimal trajectory of the beam in the undulator is found using the diagnostic mode, the two BPMs measure it and use it as a reference. Later when the machine is running in high power mode the two BPMs are used to monitor stability and position of the beam. If the beam is in the reference positions in the two BPMs then its position in the undulator should be the same as in the diagnostic mode.

The electron beam position control in the undulator is not the only reason to develop the BPM system for ELBE. As already discussed in Chapters 1 and 2, the beam transverse emittance is a very important quantity for FEL. There are two items one has to remember to provide the FEL with an electron beam with appropriate emittance. First of all the electron source has to generate the beam with the low emittance. Secondly one has to preserve the emittance during the electron beam transport from the source to the FEL. One of the important conclusions of emittance preservation physics is that one has to minimize the misalignment of the quadrupoles and the accelerating structures to prevent emittance increase [4.4]. In other words an electron beam should be aligned as close as possible to the axes of these elements.

A BPM can be mechanically aligned to the beam line elements with a limited accuracy. It is also important to realize that mechanical center of the BPM can differs from the electrical one. For these reasons, the presence of a BPM system does not lead automatically to an optimal beam transport but once the optimal trajectory is found the BPM system can be used to characterize its stability and to locate an element causing problems, which is the case especially during commissioning. Thus the whole accelerator and not only the FEL surroundings should be equipped with the BPM system.

ELBE is a multi-purpose accelerator dedicated not only to the FEL but also for experiments in nuclear physics, radiation physics and neutron physics. All these applications require stability of the electron beam position and will benefit from the BPM system.

4.2   Design of BPM

4.2.1 Requirements of the BPM system

There are different types of BPM detectors successfully used to measure the position of charged particles beams. When designing a new BPM system, first it has to be decided which kind of BPM detector is most appropriate. The parameters of the beam like average current, its time structure and bunch charge have to be taken into account to make a reasonable choice. From the very beginning it is important to understand what the requirements of the BPM system are. Of course, the most important question is the required resolution of the system. But it is also important to understand if a relative position or an absolute position of the beam is important. In some cases it is necessary to consider a possible negative effect of the BPM detector onto the beam quality.

The following demands were made on the ELBE BPM system. Resolution of the beam position measurements is required to be 100 μm. The beam position should be measured with that resolution for up to 5 mm beam displacement from the beam line center. The system must operate with an average beam current up to 1 mA. Dynamic range of the system has to enable operation of the system in the diagnostic beam mode when the average beam current is several microamperes. The system must support operation with any possible bunch frequency. The nominal bunch frequency for the FEL operation is 13 MHz but for machine diagnostic reasons it can be reduced down to its 128th subharmonic, i.e., 101.5625 kHz. The number of required BPMs is between 20 and 30.

Two types of BPM were considered as candidates for the ELBE BPM system. One of them is the cavity beam position monitor [4.5] another one is the stripline beam position monitor [4.6]. To compare these BPM types and to choose the proper one for EBLE, analytical calculations as well as beam test measurements at the ELBE were performed. We have used the stripline BPM of the JLab FEL [4.7] for the beam measurements in the beginning of our work on the ELBE BPM system. A prototype of a cavity BPM for ELBE was built for beam measurements at Rossendorf [4.8].

4.2.2 Basics of a cavity BPM

There are different configurations of the cavity BPM. The simplest one is a cylindrically symmetric cavity. An off-center beam excites the dipole TM_{110} mode in the cavity. For small beam displacements, the mode amplitude is linearly proportional to the beam displacement from the cavity axis. The orientation of the dipole mode depends on the azimuthal coordinate of the beam as is shown in Fig. 4.1. The amplitude of the TM_{110} mode and its phase relative to an external reference are measured to determine the beam position. The beam also excites the fundamental symmetric mode of the cavity. Since the maximum of the electric field of the fundamental mode is located in the cavity center the mode is excited more efficiently. Usually this is the main limiting factor for the cavity BPM resolution. However, the signal delivered by this type of BPM detector is much higher than the signal of any other BPM, since the cavity is a resonant structure and makes use of its quality factor.

There are two applications where the cavity BPM has strong advantages. First, the cavity type BPM has been successfully used to demonstrate a submicron resolution of position measurements [4.9]. The resolution was demonstrated for a bunch charge of nC in order of magnitude. Second, the cavity BPM can be used for the position measurement of a beam with a very low, nA in order of magnitude, average current [4.10].

Several aspects of this BPM approach can be seen as shortcomings. An electron bunch interacting with the cavity also generates a wakefield [4.11]. The wakefield acts back on the electron beam affecting its quality. There is a very strong correlation between the cavity signal used for the position measurement and the generated wakefield, since both are dependant on the shunt impedance of the cavity. Thus increasing the cavity BPM resolution potentially decreases the beam quality. This should be taken into account very carefully especially in the case when a big number of BPM detectors is required. A high cavity quality factor results in a narrow bandwidth of the resonance. Sometimes the cavity BPM needs temperature stabilization, which takes considerable length on a beam line. It is necessary in making the mechanical design of the BPM to take into account that pumping out the cavity leads to its deformation and thus to a frequency change. Since it is necessary to

deal not only with the RF signal amplitude but also with its phase the corresponding BPM electronics is relatively complicated. Temperature stabilization of the electronics and the transmission line from the BPM to the electronics might be required.
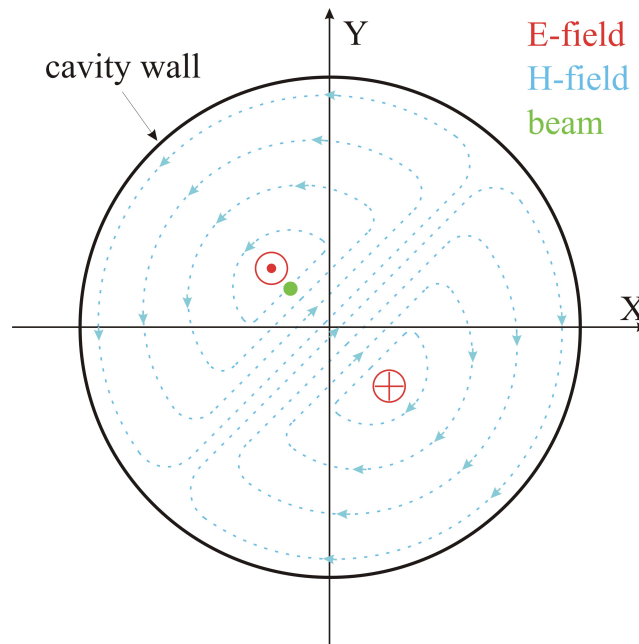

Figure 4.1 Excitation of the TM$_{110}$ mode by an off-center beam in the cavity BPM

The cavity BPM is a very good diagnostics tool that sometimes does a job which cannot be done by any other BPM. The price for that are its relative complexity and the fact that the cavity BPM design is a complicated trade-off. A prototype of a cavity BPM for ELBE was developed, manufactured and tested with beam in Rossendorf [4.8]. Results of the measurements are in good agreement with the expectations. However, we decided to build the ELBE BPM system based on another BPM type. This is the stripline BPM. The reason for the decision was that we found the stripline BPM and the corresponding electronics simpler, while we proved that the stripline BPM based system can meet the system requirements. The design of the stripline BPM is described in the rest of this section.

4.2.3 Image current as a foundation of the stripline BPM operation

Before we consider another type of BPM detector, we recall some basics of electrodynamics. A charged particle beam is always accompanied by electromagnetic field. In the case of a relativistic electron beam, because of the Lorenz transformation the field is compressed in the direction perpendicular to the beam direction. Consider a beam propagating in a tube with ideally conducting walls. The diameter of the beam is much smaller than the tube diameter. There is the required condition that no electrical field is inside the conducting walls. To satisfy this condition, a current flows on the inner surface of the wall. This is the so-called image current. It is intuitively clear that the average value of the current is equal to the average beam current and the direction of the image current is opposite to the beam current direction. The longitudinal current distribution and the time structure of the image current follow the beam structure, because of the relativistic field compression. The most important question is the distribution of the image current on the inner wall surface when we are interested in beam position measurement. It is clear that the distribution depends on

the beam position inside the tube. Using the image current method, one can show [4.12] that the distribution is

$$I_{img}(r,\alpha,\varphi) = \frac{I_0}{2\pi\ R}\frac{R^2 - r^2}{R^2 + r^2 - 2R\ r\cos(\varphi - \alpha)},$$ (4.1)

where I_0 is the beam average current, R is the inner radius of the tube, α and r are the polar coordinates of the beam and φ is the polar coordinate of the point where the current is measured. The polar coordinate system is depicted in Fig. 4.2. The formula is derived with the assumption that the beam radius is much smaller than the tube radius. Since the distribution depends on the beam position, it can be used for beam position measurements. A complete measurement of the distribution function is a difficult experimental task, and as we will show now, it is not necessary to do this to reconstruct the beam position. Imagine that instead of a continuous pipe we have four equal electrodes symmetrically placed on circumference with angular shift of $\pi/2$ between neighbors. Let θ be the angular size of the electrodes. Imagine also that we have found a way to measure the integral current on such electrodes. The angular distribution of the image current can also be expressed in a different way from Eq. 4.1 namely [4.13]

$$I_{img}(r,\alpha,\varphi) = \frac{I_0}{2\pi\ R}\left\{1 + 2\sum_{n=1}^{\infty}\left(\frac{r}{R}\right)^n \cos(n(\varphi - \alpha))\right\}.$$ (4.2)

Note that this equation is totally equivalent to 4.1. We will call electrodes placed right and left "R" and "L". The currents through the electrodes are accordingly

$$I_R(r,\alpha) = \int_{-\theta/2}^{\theta/2} I_{img}(r,\alpha,\varphi)R\ d\varphi$$ (4.3 a)

$$I_L(r,\alpha) = \int_{\pi+\theta/2}^{\pi-\theta/2} I_{img}(r,\alpha,\varphi)R\ d\varphi$$ (4.3 b)

The Eqs. 4.3 can be easily integrated using Eq. 4.2 resulting in the integral current on the electrodes "R" and "L". Accordingly,

$$I_R = \frac{I_0}{2\pi}\left\{\theta + 4\sum_{n=1}^{\infty}\frac{1}{n}\left(\frac{r}{R}\right)^n \sin\left(n\frac{\theta}{2}\right)\cos(n\alpha)\right\},$$ (4.4 a)

$$I_L = \frac{I_0}{2\pi}\left\{\theta + 4\sum_{n=1}^{\infty}\frac{1}{n}\left(\frac{r}{R}\right)^n \sin\left(n\left(\frac{\theta}{2}+\pi\right)\right)\cos(n\alpha)\right\}.$$ (4.4 b)

In all practical cases of interest the electron beam should be placed near the beam line center. For that reason we consider an approximation where $r \ll R$. If we keep in Eqs. 4.4 terms up to first order this will give the following

$$I_R = \frac{I_0}{2\pi}\left(\theta + 4\frac{r}{R}\sin\left(\frac{\theta}{2}\right)\cos(\alpha)\right)$$ (4.5 a)

$$I_L = \frac{I_0}{2\pi}\left(\theta - 4\frac{r}{R}\sin\left(\frac{\theta}{2}\right)\cos(\alpha)\right).$$ (4.5 b)

Making the sum and difference of these two equations and using $x = r\cos(\alpha)$, we can express the horizontal beam position via I_R and I_L. Obviously, the vertical position of the beam can be expressed in the same way through the currents on the top

and the bottom electrodes I_T and I_B. Thus the beam position as a function of the integral currents is written as

$$x = \frac{R}{2} \frac{\theta/2}{sin(\theta/2)} \frac{I_R - I_L}{I_R + I_L} \qquad\qquad y = \frac{R}{2} \frac{\theta/2}{sin(\theta/2)} \frac{I_T - I_B}{I_T + I_B}. \qquad (4.6 \text{ a, b})$$

As was mentioned above it is not necessary to measure the entire distribution function of the image current to estimate the beam position. Four integral measurements are enough. Moreover, one remarkable feature of the approach is that such beam position measurements do not depend on the beam current.
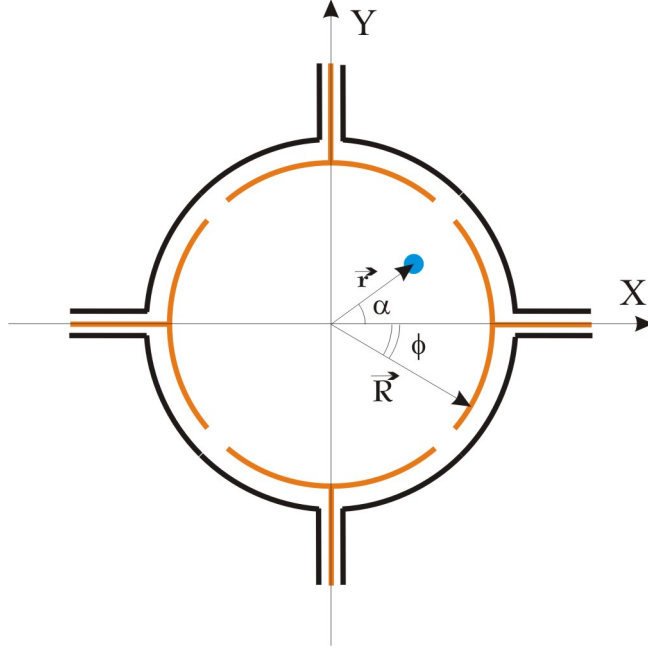
Figure 4.2 Coordinate system for the image current calculations

Consider now dependence on the angular width of the electrodes. The angular size of the electrodes θ can vary in the range from 0 to almost $\pi/2$. The function $\frac{(\theta/2)}{sin(\theta/2)}$ is rather slow one. In the listed angular range the function changes its value from 1.0 to 1.1. This is why one meets very often in the literature Eqs. 4.6 in the following form: $x = \frac{R}{2} \frac{I_R - I_L}{I_R + I_L}$ and $y = \frac{R}{2} \frac{I_T - I_B}{I_T + I_B}$. This leads to a maximum possible error of 10 % and, in practice, it is much smaller. This way to process the BPM data is called "difference over sum" or "normalized difference". There are also some other BPM data processing algorithms. A very good overview with comparisons of the different approaches can be found in [4.14].

The next point one has to note about such position measurements is that, in general, Eqs. 4.4 are not linear functions. We have gotten the linear dependence of the currents on the beam displacement in Eqs. 4.5 only, because we have considered the first-order terms of r/R. That means the linear dependence is true only for a small beam displacements and in practice we should observe the nonlinear response of the BPM to the beam position. One straightforward way to calculate the nonlinearity of the BPM response is to integrate numerically Eqs. 4.3, using the distribution function of the image current in the form given by Eq. 4.1. In the calculation the beam displacement is the input parameter. For a given beam displacement we calculate the

image current distribution and integrate it in the angular range corresponding, for example, to the electrodes "R" and "L" resulting in the integral current flowing over these two electrodes. As a last step we calculate the beam position using Eqs. 4.6. To get the sought after nonlinear dependence, we repeat such procedure for the beam displacements in the range from 0 through R. Results of the calculations are shown in Fig. 4.3 for a beam pipe radius of 18.9 mm, which is the ELBE beamline inner radius, and for an angular electrode's size of 68°. A linear function is shown on the same plot to facilitate judgment on the nonlinearity. As we can see for the beam displacement in the range $\pm 0.25R$, deviation of the BPM response from the linear function is relatively small. In fact, it is less than 2 % in the listed range. However, for a bigger beam displacement, the difference of the BPM function from the linear one grows rapidly and for a beam shift of $0.9R$ the error in the position measurement would be more than 50 %. Recall now that the beam position should be measured with good resolution for up to 5 mm beam displacement from the beam line center. This requirement fits very well to the linear range of the BPM function with $\varDelta r << \pm 0.25R$, since for the ELBE beamline $0.25R = 4.7mm$. Thus we can use the procedure for the beam position measurement described above and summarized in Eq. 4.6 without any corrections for nonlinear BPM response.
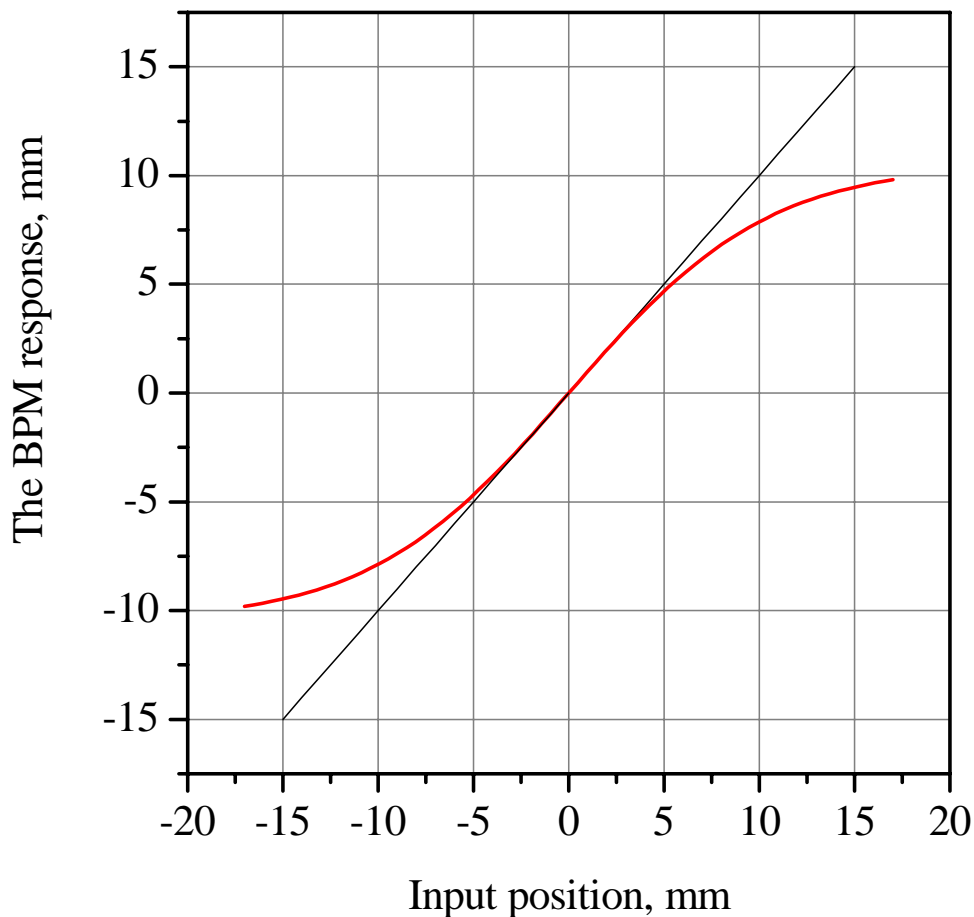

Figure 4.3 Nonlinearity of the BPM response

Using Eqs. 4.5 one can calculate the sensitivity of the BPM to the beam displacement in terms of the signal power difference on the two opposite channels. In the small beam displacement approximation we are looking for a linear function and we can write the power difference in a logarithmic scale as follows

$$x\, C_X = 20\, log_{10}\left(\frac{I_R}{I_L}\right),$$ (4.7)

where C_X is the constant we are looking for. After a simple transformation, keeping only the linear term, we get

$$C_X = \frac{80}{ln\,10}\frac{sin(\,\theta\,/\,2\,)}{(\,\theta\,/\,2\,)}\frac{1}{R}.$$ (4.8)

Substituting in Eq. 4.8 $R = 18.9mm$ and $\theta = 68°$ we get the sensitivity of our BPM equal to 1.8 dB/mm. Note that this is the difference of the signal power of two opposite channels. The change in one channel signal power is naturally half of that, i.e., 0.9 dB/mm.

4.2.4 Microwave concept of the stripline BPM

Several aspects make accurate image current measurements nontrivial in our case. One problem is that the current we need to measure is not a DC current but has a time structure almost copying the time structure of the beam. We consider the beam which will be used to run the ELBE FEL. This is a CW beam of very short, 1 ps in order of magnitude, pulses traveling with a repetition rate of 13 MHz. To do the proper measurements one always has to consider the electromagnetic spectrum of the beam. As any periodic function, the beam current can be represented by its Fourier series. If a function has a fundamental frequency f_0 then its spectrum contains only harmonics of f_0, i.e., all frequencies $f_0 n$, where n is an integer. Thus, if we look at the beam spectrum, we will see a set of spikes each separated from its neighbors by 13 MHz. The envelope of the spectrum corresponds to the Fourier transform of a single bunch. That means in the case of 1 ps bunches the beam spectrum expands, generally speaking, up to the THz range. Of course, in reality it is always limited by the bandwidth and by the sensitivity of the instruments we use. The width of every single spike in the spectrum corresponds to a macropulse length if the beam is macropulsed. In the case of CW beam, the observed spike width is defined by the bunch to bunch time jitter, by the measurement time, or by the resolution bandwidth of the instruments.

Now we consider the microwave concept of the stripline BPM. In general it is very close to a so-called directional coupler widely used in the RF and microwave technology. A stripline BPM consists of two coaxial tubes. The inner tube is cut in a way that forms the four electrodes, which we have discussed above. The outer tube is the vacuum chamber wall. So the electrodes and the outer tube form four transmission lines. The distance between the tubes is chosen so that the impedance of the transmission line is 50 Ω. The inner tube has a longitudinal gap on the upstream side. Near the gap an RF feedthrough is connected to the inner tube. The impedance of the feedthrough is also 50 Ω. The scheme of the stripline BPM is shown in Fig. 4.4. The inside diameter of the inner tube can be made equal to the inside diameter of the beamline. In this case the change of the beamline impedance is minimized. This is important when wakefield effects play a noticeable role and have to be considered in the emittance budget [4.15].
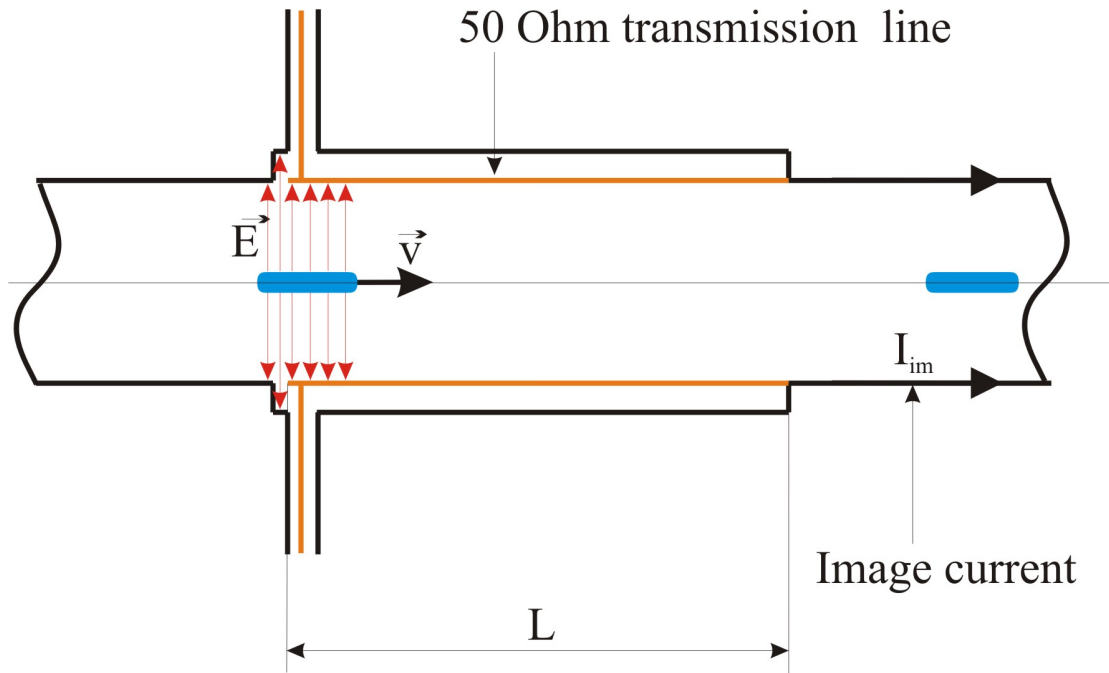
Figure 4.4 The stripline BPM schema

Now we examine the signal formation on this type of electrodes. When an electron bunch passes under the gap, in the inner tube a part of its electromagnetic field is coupled into the transmission line. The field has two ways to propagate. These are the transmission line and the feedthrough. Since the two ways have equal impedances, half of the power coupled in will propagate into the transmission line and the other half goes into the feedthrough. There are different possibilities of the transmission line configuration on the downstream side. We consider the case of the transmission line ended by short circuit. The portion of the RF field propagated in the transmission line is reflected from the short circuit and propagates in the opposite direction with changed polarity. The signal measured on such type of electrodes is a bipolar-doublet, i.e., it consists of two peaks with different polarity and separated in time by $2L/c$, where L is the transmission line length and c is the speed of light.

In the very first measurements with stripline BPM we used a BPM of the JLab FEL which we have had installed at the ELBE injector. The measurements were done with an electron beam energy of 250 keV. An example of the BPM signal in the time domain is shown in Fig. 4.5. This is the response of the BPM to a single bunch.

It is not necessary to have a short circuit at the downstream side of the transmission line. This can ends either with open end or with another RF feedthrough. The second feedthrough can be terminated with 50 Ω and also can be used to pass the signal to BPM electronics. The latter is especially useful for an accelerator with two beams propagating in opposite directions. It is not difficult to prove that on every feedthrough a signal from only one of the beams will show up [4.6].

Let us consider the BPM signal in the frequency domain. There is a boundary condition for the transmission line with a short circuit on one side that any standing wave has a zero of the voltage and maximum of the current on the short. For that reason the BPM has different sensitivities to different frequencies. It has maximum sensitivity for all frequencies corresponding to the wavelengths $\lambda_m = 4L/m$, where m is an odd integer. The first maximum of the sensitivity is at $L = \frac{1}{4}\lambda$, the second one at $L = \frac{3}{4}\lambda$ and so on.
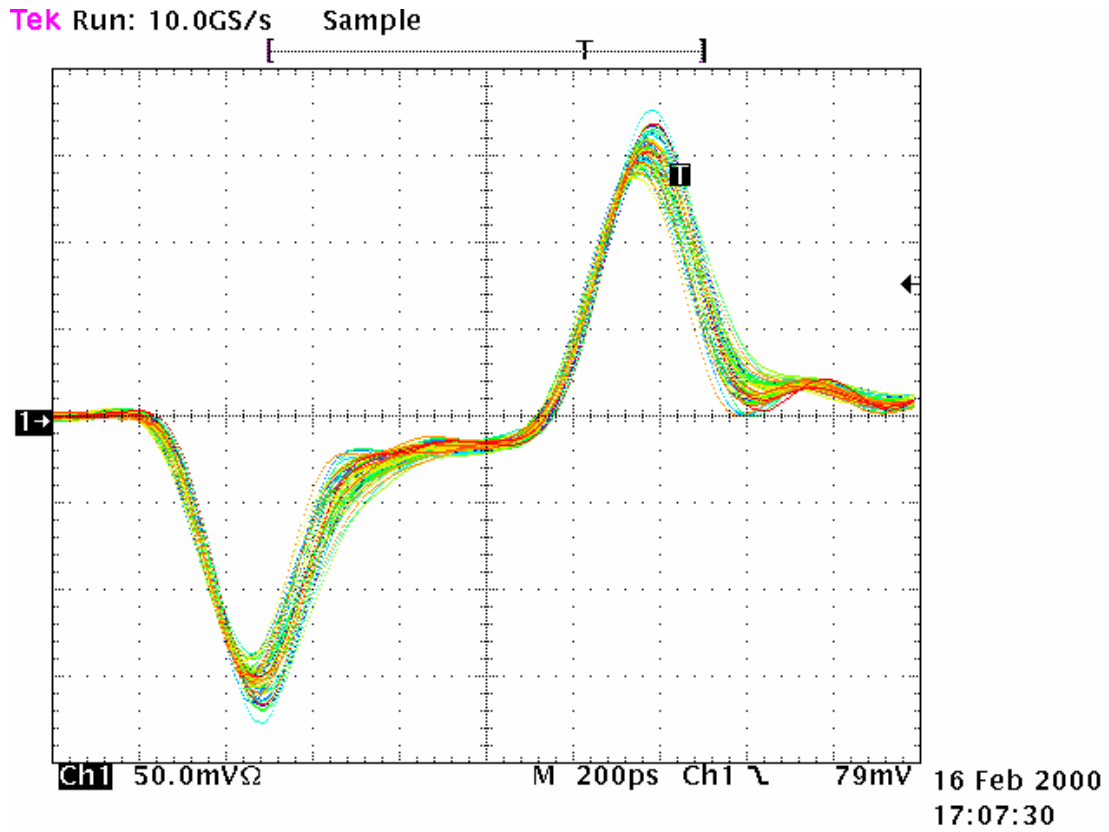
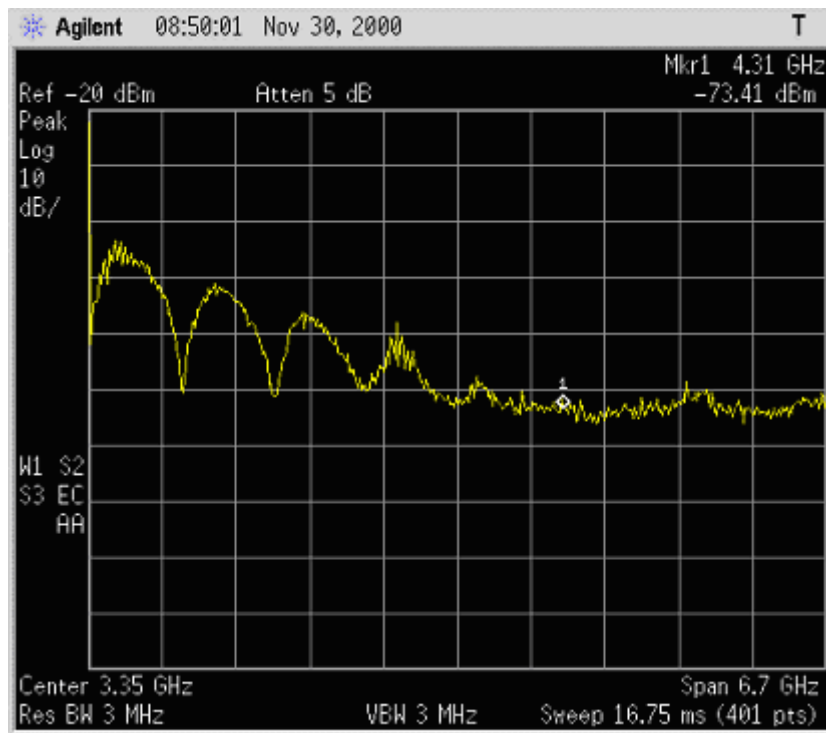*Figure 4.5 Signals of the BPM in the time domain*

Figure 4.6 Signal of the BPM in the frequency domain

One should find the Fourier transform of the BPM signal to show this mathematically. We will use the following simple form of the signal corresponding to a Gaussian bunch

$$V_{BPM}(t) = V_0 e^{-\frac{(t+\tau)^2}{2\sigma^2}} - V_0 e^{-\frac{(t-\tau)^2}{2\sigma^2}} \tag{4.9}$$

where σ stands for the RMS bunch length and $\tau = L/c$ is the half of the distance between the two peaks, V_0 is a constant containing the average beam current and the impedance of the transmission line. The Fourier transform of Eq. 4.7 is

$$V_{BPM}(\omega) = 2V_0\sigma\, e^{-\frac{\omega^2\sigma^2}{2}} \, sin\left(\frac{\omega L}{c}\right). \tag{4.10}$$

As was explained above, the function has its first maximum at $L = \frac{1}{4}\lambda$. An example of the calculated BPM response function is shown in Fig. 3.4. The calculations are done for a BPM with 173 mm long electrodes. The response of the BPM measured with the help of a spectrum analyzer is shown in Fig. 4.6.

The JLab FEL machine BPM was designed to have a maximum response at 1.5 GHz. The fundamental frequency of the JLab linac is 1497 MHz. The BPM was also designed in a way that the sensitivity maximum at 1.5 GHz is the second maximum of the response function. That means the strip length corresponds to $\frac{3}{4}\lambda$, where λ is the wavelength of 1.5 GHz. That was done partly for historical reasons and partly because the length of the BPM is suitable for the accelerator and no problem was found during the BPM manufacturing.

Based on the JLab design, a prototype was build of the stripline BPM adopted for ELBE. The length of the electrodes was chosen to be $\frac{3}{4}\lambda$, that is, 173 mm for 1.3 GHz. The BPM is made of stainless steel and is electron beam welded. It has four SMA type feedthroughs that are also electron beam welded to the BPM. The electrodes are made with an angular size of 68°. The choice of this size is always a trade-off between BPM sensitivity and linearity of the BPM response. A BPM with an electrode size approaching $\pi/2$ would capture the maximum image current and would have maximum possible sensitivity. On the other hand the linearity of the BPM will suffer from such wide electrodes. The big width will also increase the RF coupling of the vertical and horizontal electrodes and this is very undesirable. On the other hand making the electrodes too narrow could cause not only a small sensitivity but also some difficulties for the transmission line impedance calculations.

In our case the width of the electrodes can be considered as much bigger than the distance between the two tubes. In this case simple analytical calculations are enough to find the geometrical parameters resulting in the 50 Ω impedance. The outside diameter d_{in} of the inner tube is known since the beamline tube is given. Then for the electrodes' width θ, the inside diameter d_{out} of the outer tube is calculated. Impedance of the transmission line is inversely proportional to its width for a given distance between electrodes. This can be seen as follows. Impedance is proportional to inductance and inversely proportional to capacitance. Widening the electrodes increases the capacitance and decreases the inductance and as the result decreases the impedance. If the electrode of angular size θ is needed with an impedance of 50 Ω then the coax with the same inner and outer diameters d_{in} and d_{out} must have an impedance of $Z = \left(\frac{\theta}{2\pi}\right)50\Omega$. The impedance of the coaxial line is given as

$$Z = \frac{Z_0}{2\pi}ln\left(\frac{d_{out}}{d_{in}}\right) \tag{4.11}$$

where Z_0 is the impedance of free space and that is 120π Ω. For the inside diameter d_{out} of the outer tube one gets

$$d_{out} = d_{in} e^{\left(\theta \cdot \frac{50}{Z_0}\right)}. \tag{4.12}$$

Substituting in Eq. 4.10 $\theta = 68°$ and $d_{in} = 37.8$ mm we find $d_{out} = 44.2$ mm. These are geometrical parameters of the ELBE stripline BPM. Note if one needs to have very narrow electrodes such simple analytical approach might be not sufficient and more detailed modeling using a computer code will be required.

4.2.5 First beam tests and essential BPM measurements

Two prototypes were manufactured to make a beam test, that is, to measure the BPM response and to compare it with the calculated one. At the time the ELBE injector was operational and that was used to do the measurements. One of the BPMs was installed at the end of the injector beamline. The measurements were done with the help of a spectrum analyzer. There were two HELIAX® type RF cables feeding the BPM signals to the spectrum analyzer. The cables are about 25 m long and can be used for signals up to several GHz. Since the first measurements were the basis for all the following work on the BPM system, we needed precision in the measurements. The attenuation of the cables was measured at 1.3 GHz to be 5.52 dB and 5.93 dB.
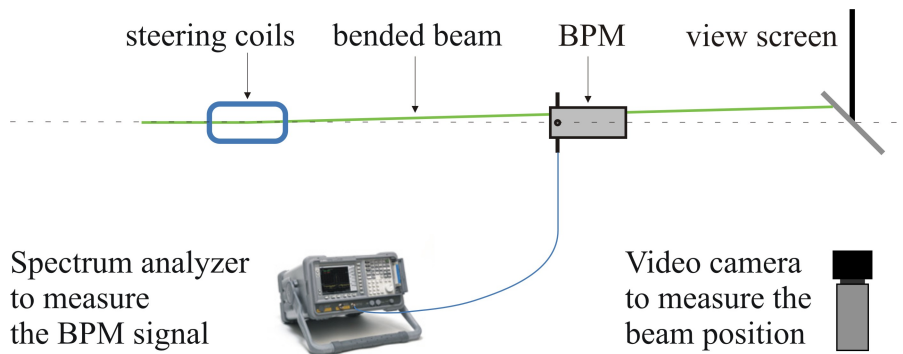
Figure 4.7 Beam line scheme to measure the BPM response; corrector, BPM, view screen

The measurements had two main objectives. The first one was the measurement of the BPM signal versus average current of the beam and the second one was the measurement of the BPM response to the beam displacement. The beam current was measured first at the electron gun or, speaking more precisely, in the high voltage power supply of the gun. An isolated beam dump working as a Faraday cup also measured the beam current. This is necessary to ensure that there is no significant beam loss. At the same time it was a crosscheck on current measurements. For the measurements we needed another independent method to measure the beam position. A view screen installed upstream from the BPM was used for that purpose. Steering coils placed upstream from the view screen and the BPM were used to change the beam position. The configuration of the beamline is shown schematically in Fig. 4.7. As the first step, the steering coils were calibrated. In the very beginning of the measurements we have found settings of the steerer that put the beam in the BPM center. With this settings position of the beam is measured with the view screen and is defined as a zero. Secondly, the beam position was measured with the view screen as a function of the coil current. The distances between the steerer and the view screen

and between the view screen and the BPM are known. Using the data we could calculate the beam displacement in the BPM induced by the steerer as the function of its current.

A very important question for the prime measurement is: what do we measure? The answer arises from an idea of how the future BPM electronics is going to be built. Kevin Jordan from the JLab FEL has proposed to build the BPM electronics for ELBE based on a logarithmic amplifier and to work in the frequency domain. Design, tests, commissioning and performances of the BPM electronics are described in the next section of this chapter. There we will also explain in more detail why the measurement was made the way it was.
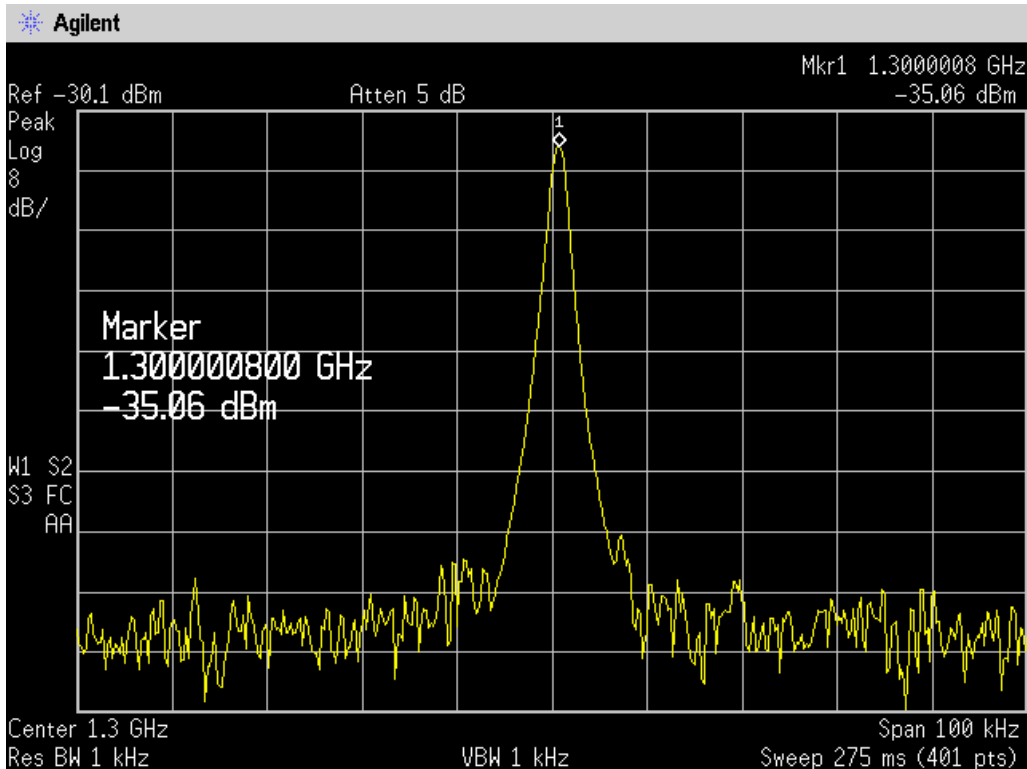
Figure 4.8 Measurements of the 1.3 GHz component of the BPM spectrum

Naturally the measurements were done in the frequency domain. We have measured the power of the 1.3 GHz component of the BPM signal. This component is one of the peaks comprising the BPM signal in the frequency domain as described above. There is an example of one such measurement in Fig. 4.8. The measured dependence of the power the 1.3 GHz component on the average beam current is shown in Fig. 4.9. The measurements are done keeping the beam always in the center of the BPM. To do so the power on two opposite channels was measured and if necessary the beam was steered by the corrector. Results of the measurements are shown in logarithmic and linear scale. The linear scale is used to show that the BPM response to the beam current is linear. The logarithmic scale is used since it is convenient in RF and microwave technology. If one keeps in mind that the BPM delivers about –24 dBm at 1.3 GHz for a beam of 1 mA average current and the response is linear this will be enough to know the BPM signal level at any beam current.
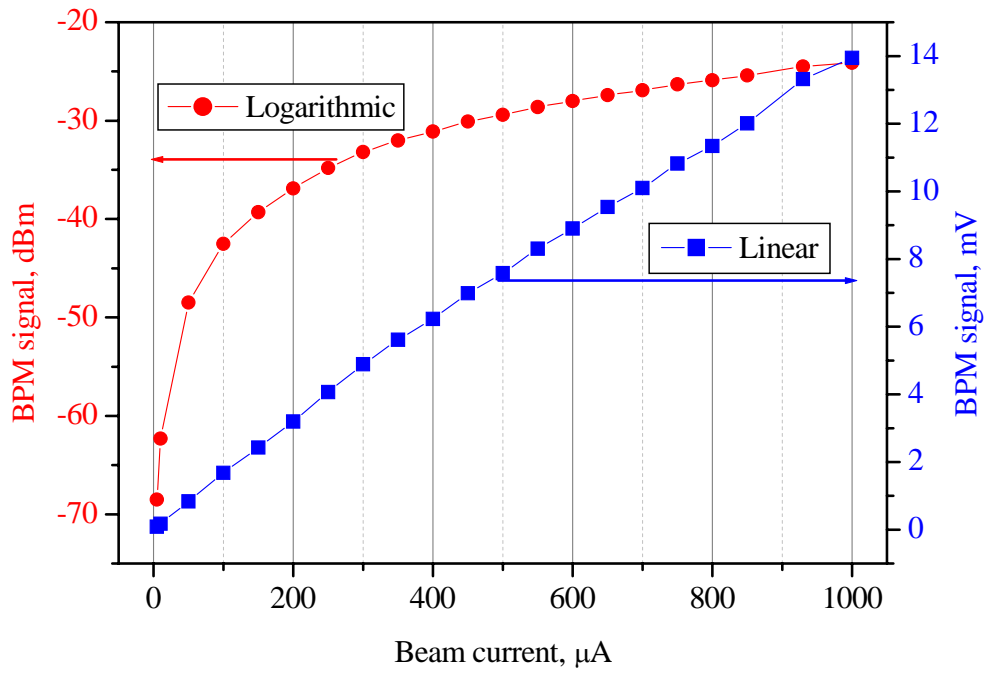
Figure 4.9 The measured dependence of the BPM signal from the average beam current. The measurements are done keeping the beam in the BPM center
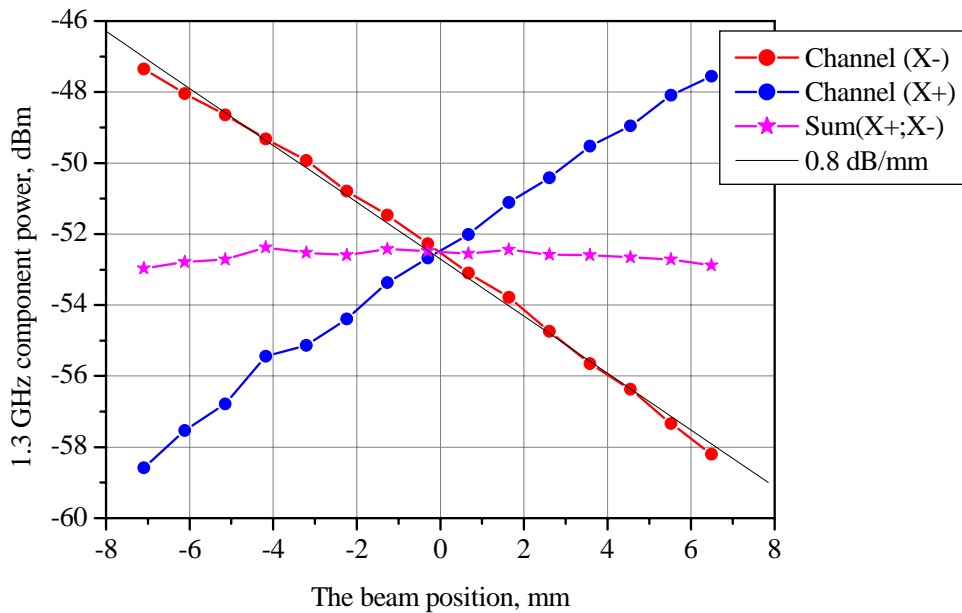

Figure 4.10 Dependence of the BPM signal from the beam position measured at the ELBE injector with a spectrum analyzer. The measurements were done with an average beam current of about 40 μA.

The signal power measured at 1.3 GHz on two opposite channels as a function of the beam position is shown in Fig. 4.10. The signal sum is also presented to show that

there is no significant beam loss when we steer the beam. The measurement data of a single channel are approximated with the linear function that gives the sensitivity of the BPM. The measured sensitivity is 0.8 dB/mm. This is only 2.4 % different from the calculated sensitivity of 0.9 dB/mm.

4.2.6 Potential resolution of the stripline BPM

The measurements of the BPM signal over the beam current are enough to estimate the potential resolution of the position which can be delivered by this type of BPM detector. If we define the resolution as the beam displacement equivalent to the system noise then from Eq. 4.6 follows

$$\sigma_X = \frac{R}{2}\frac{\theta/2}{sin(\theta/2)}\frac{\sqrt{2}\sigma_I}{2I} = \frac{R}{2\sqrt{2}}\frac{\theta/2}{sin(\theta/2)}\sqrt{\frac{P_N}{P_S}} \qquad (4.13)$$

where P_N and P_S are the noise and the signal power respectively. The noise power is

$$P_N = kT_0 B , \qquad (4.14)$$

where T_0 is the temperature, B is the measurement bandwidth and k is the Boltzmann's constant. Sometimes this fact is referred to as the Nyquist's theorem. The noise density kT_0 for a room temperature of 290 K is $4 \cdot 10^{-21}$ W/Hz or -174 dBm/Hz. The signal power was measured and the noise power is calculated assuming the measurement bandwidth of 10 MHz. This choice of the bandwidth will be explained in the next section of this chapter. The resolution of the stripline BPM as given by Eq. 4.13 with the beam measurement data is shown in Fig. 4.11. The resolution delivered by the BPM is better than the required 100 μm for a beam with an average current of more than 6.6 μA. Of course, an entire BPM system has a resolution worse than the detector can provide because any BPM electronics adds some extra noise decreasing the signal-to-noise ratio.

Thus already in the first measurements it was demonstrated that the stripline BPM can be used at ELBE for beam position measurement and can easily deliver the required resolution of 100 μm.

4.2.7 Development of ¼λ BPM

Several problems were found during BPM manufacturing as well as during their practical use at the accelerator. Two BPMs were built to see how reliable is the technology of manufacturing. In fact about 50 % of the RF feedthroughs were broken during the first electron beam welding by the company. That was a very bad result, if one takes into account that the feedthroughs are the most expensive part of the BPM and have a long delivery time. Next we found that the four stripe electrodes were positioned at slightly different distances from the BPM center. Figure 4.12 shows the CAD drawing of the ¾λ BPM. The inside view of the BPM demonstrating the problem is shown in Fig. 4.13. The reason for that was mechanical stress in the tube used to form the electrodes. After the tube was treated on a wire-cut machine the stress bent the electrodes. This leads to different impedances of the transmission lines and also causes some extra shift between the electrical and the mechanical center of the BPM. Besides the bent electrodes cause some additional mechanical stress to the RF feedthrough threatening to break them. One more problem of the BPM with 173 mm long electrodes is that it is not possible to estimate its electrical center. The

procedure of the electrical BPM center estimation will be described later in this section in detail. The next problem of our first BPM was that sometimes it was not possible to put the BPM at desirable position on the beamline because of its length. All these problems motivated us to redesign the stripline BPM.
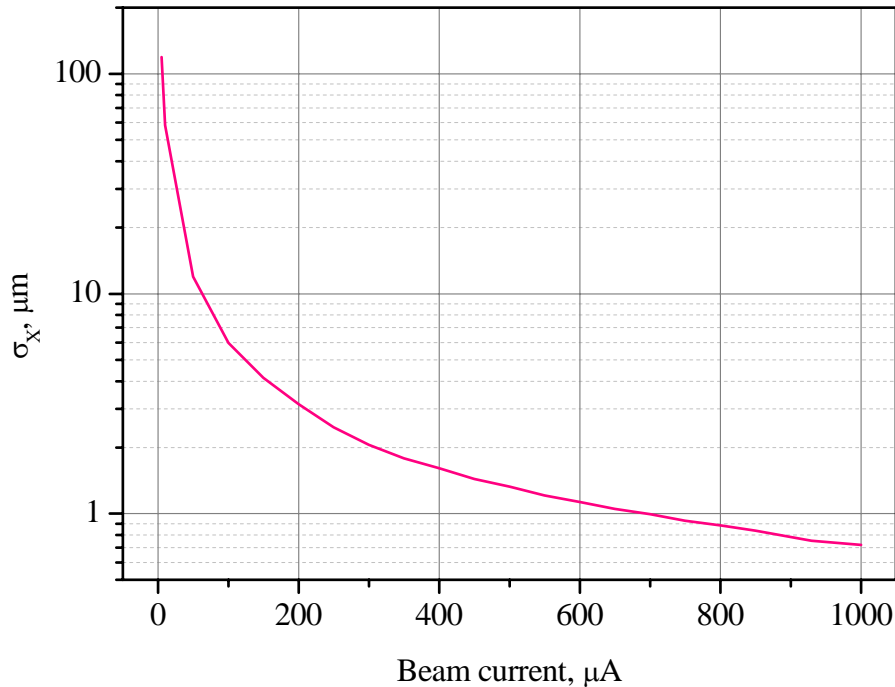

Figure 4.11 Resolution of the stripline BPM calculated using equation 4.13 and the measurement data shown on the Fig. 4.9

The main idea for the new design was to make the stripes only $\frac{1}{4}\lambda$ long instead of $\frac{3}{4}\lambda$. To keep time and money and to be more flexible in the sense of editing the new design we decided at first not to build a real BPM, which could be installed and tested on the beamline, but to build its electrical model. From the microwave point of view the model is exactly the same as a real BPM but it can be manufactured much faster, since there is no welding and different pieces are screwed together. We also have used front-panel-mount SMA connectors instead of vacuum-sealed feedthroughs. Several photographs of the BPM model are shown in Fig. 4.14.

A wire test bench was used to evaluate the $\frac{1}{4}\lambda$ BPM model. In these experiments a thin conducting wire is stretched through the BPM. The wire forms a coaxial transmission line with the grounded BPM. An RF generator was used to excite a TEM-wave in the BPM. The field of the wave simulates the beam field. We have mounted our test bench on an optical table to reduce undesirable wire vibrations. So the wire with 1 mm diameter was fixed always in one position. The BPM model was mounted on a linear motor stage. Driven by a stepping motor, the stage has a resolution of 2.5 μm. The system was aligned so that the wire was in the mid plane of the BPM model. The BPM model was moved by the stage horizontally. We discovered that any motion of a person in the room with the equipment causes a parasitic signal much bigger than the system noise.
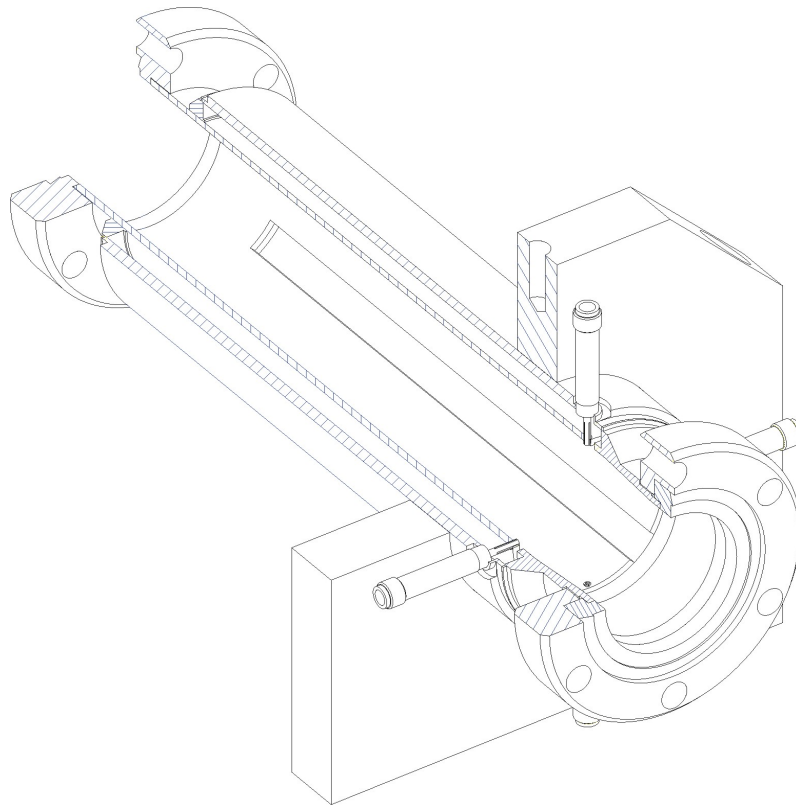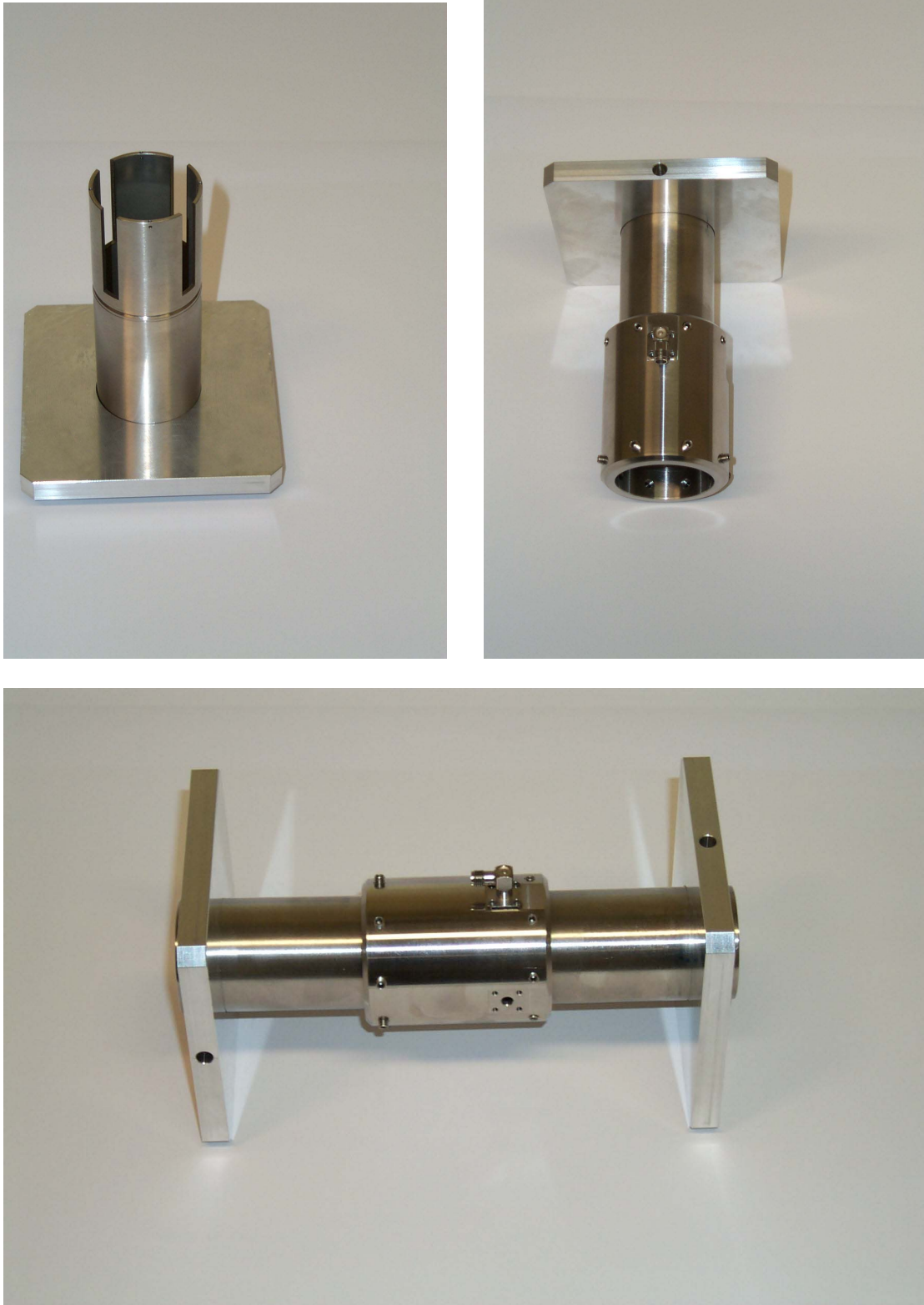
Figure 4.12 ¾λ BPM CAD drawing
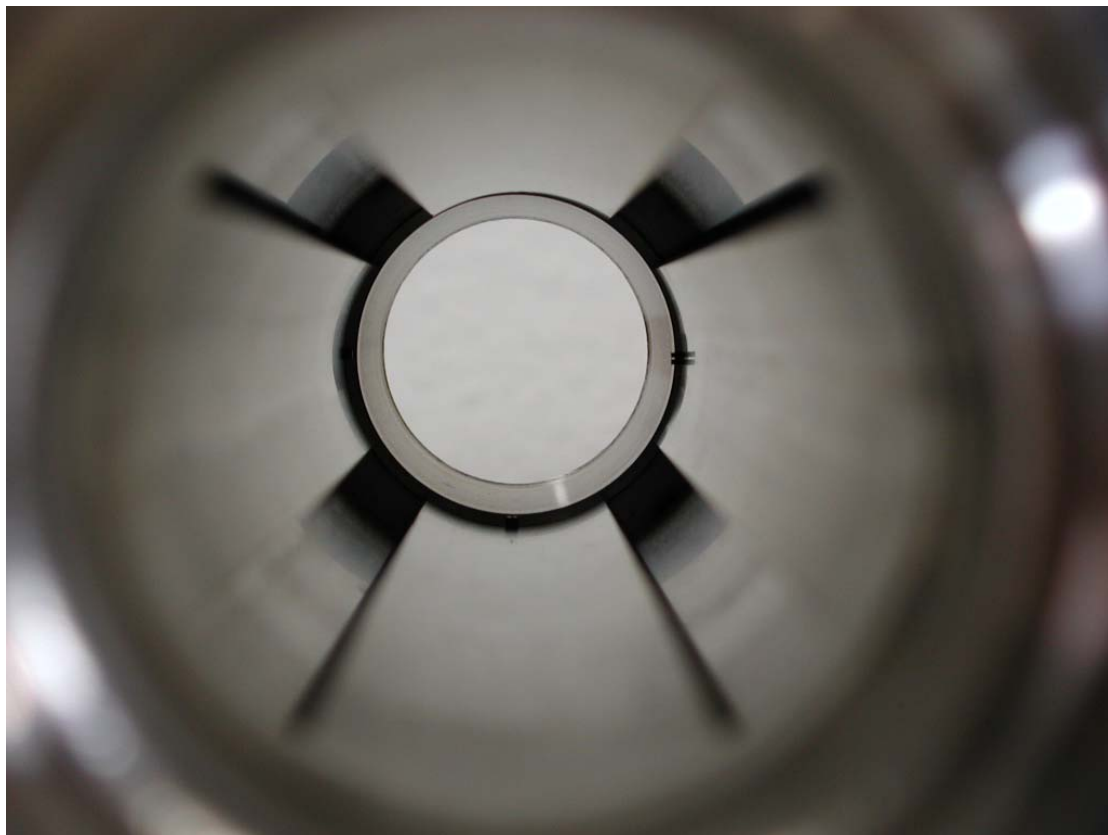
Figure 4.13 Inside photograph of the BPM with a different position of the stripes

Figure 4.14 Electrical model of the λ/4 BPM. The technique of electrical prototyping is a very time efficient and cost efficient way to prove correctness of the general design idea.

For that reason the test bench was placed in a separate room and was completely remote controlled over the Ethernet. In this experiment we have used some of the first prototype versions of our BPM electronics based on the AD8313 logarithmic amplifier.

First the $\frac{3}{4}\lambda$ BPM was installed on the test bench to calibrate the RF generator. The dependence of the BPM signal on the beam current had been already measured, namely 1 mA of average current corresponds to about –24 dBm on the BPM output at 1.3 GHz. To calibrate the generator with the installed long BPM we found the power level of the generator which results in –24 dBm at the BPM output. Once the long BPM was installed at the wire test bench we also tested the ability of the test bench to simulate the beam. The wire powered by the RF generator was moved precisely in the BPM and the BPM response was measured exactly in the way we did with the beam. Doing so we could compare the calculated response function, the one measured with the injector beam, and the response function measured on the test bench. Results of these measurements are shown in Fig. 4.15. As one can see, the measured response of both the $\frac{3}{4}\lambda$ BPM and the $\frac{1}{4}\lambda$ BPM model are extremely close to each other and to the calculated response function.

We also attempted to measure the cross-talk function of the BPM on the wire test bench. The question is: will we see any change in the measured vertical position if we move the wire horizontally? The measured vertical position as a function of the horizontal wire position is shown in Fig. 4.16. Interpolation of the data with linear function gives the cross-talk coefficient of $21.6 \cdot 10^{-3}$ μm/mm. This is acceptably small in our case. There is one problem in the interpretation of the measurements, namely the alignment of the entire system. The cross-talk coefficient corresponds to 1.2° of tilting with respect to the wire motion plane. The accuracy of the alignment is on the same order of magnitude. This is why it is more correct to take the measured cross-talk coefficient as a possible upper limit. Since the value is small enough and it was not easy to improve the alignment in a short time we decided not to invest time in a more accurate cross-talk measurement.

Obviously, the measurement results shown in Fig. 4.15 demonstrate that the wire test bench can be successfully used for new BPM tests. The signal amplitude of the $\frac{1}{4}\lambda$ BPM model was measured as a function of the RF generator power level. The measurements show the same dependence as for the $\frac{3}{4}\lambda$ BPM. Thus one can affirm that the coupling of the short BPM to the beam is the same as for the long one. As a consequence the BPM resolution is the same, assuming an identical measurement bandwidth. The most important result is that the $\frac{1}{4}\lambda$ BPM has no disadvantages in comparison to the long $\frac{3}{4}\lambda$ BPM. When those measurements were completed the real $\frac{1}{4}\lambda$ BPM was designed and built.

Besides the short electrodes some new technological solutions are used in the design. The BPM is not electron beam welded but brazed. This makes the BPM much cheaper, since for the brazing one can put a very big number of the BPMs in an oven and make them all at once. In the case of electron beam welding every BPM has to be welded individually. Feedthroughs of another type are used for the new BPM. The feedthrough is not welded to the BPM but connected via a Conflat® flange. The connection of the feedthrough inner contact to the electrode is made more flexible than before. This is done using an intermediate piece working as a clamp. Using the feedthrough with the Conflat® flanges makes possible an exchange of the feedthrough, for instance if one is broken, on the BPM without removing it from the beamline. This solution potentially can save a lot of time, especially in the case of a superconducting accelerator. The total length of the BPM is 85 mm.
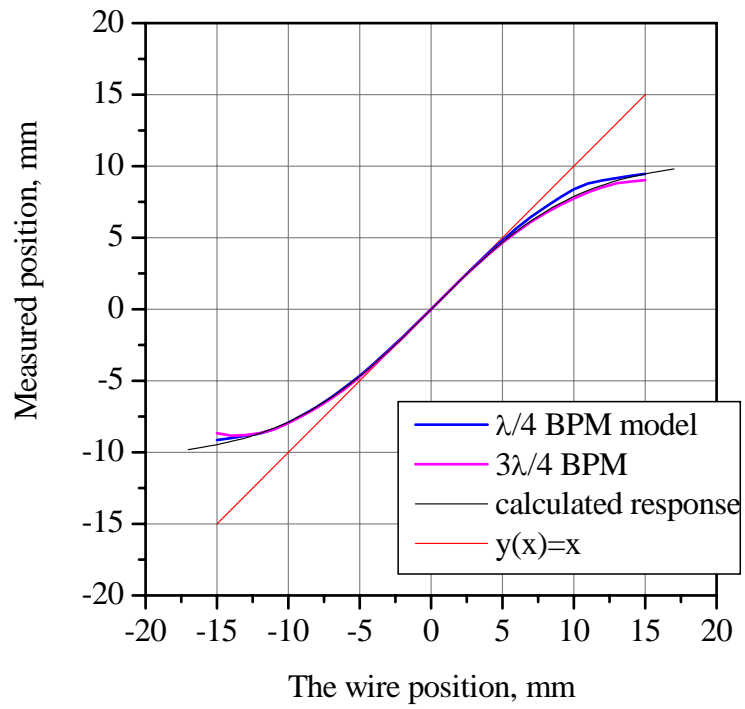
Figure 4.15 Results of the measurements on the wire test bench. Comparison of the ¾λ BPM, the ¼λ BPM model, and the calculated BPM response.
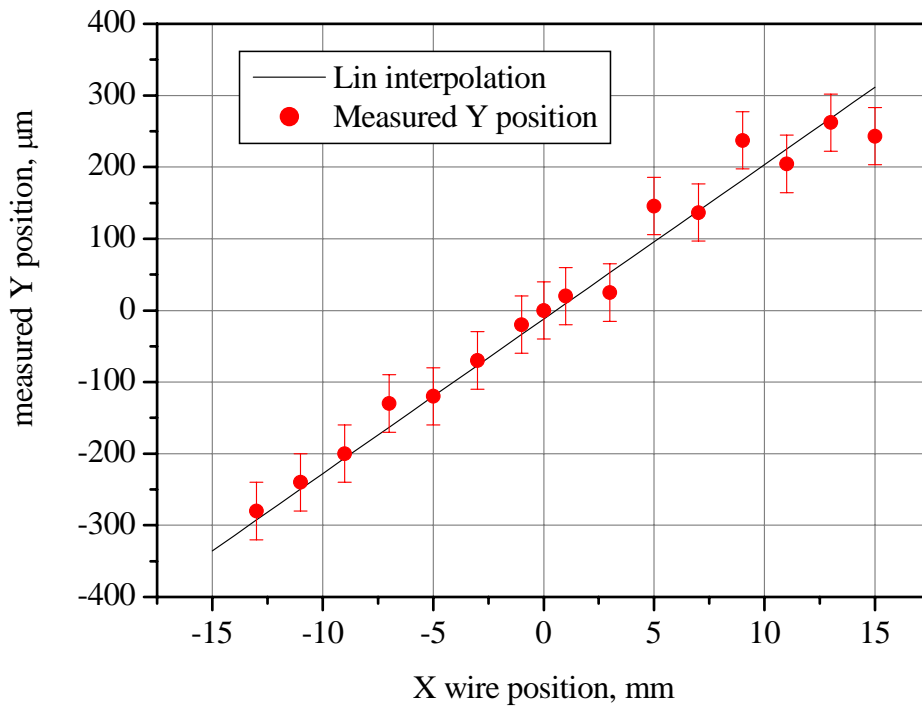

Figure 4.16 Cross-talk measurements on the wire test bench

A CAD drawing of the BPM with a cutaway view is shown in Fig. 4.17. A photograph of the ¼λ BPM together with the ¾λ BPM is presented in Fig. 4.18.

4.2.8 BPM offset

It might be surprising that the electrode length of the compact BPM is not exactly ¼λ, which is 57.7 mm for 1.3 GHz. As a matter of fact the antenna length is 40 mm. The reason for that is the following. As was already mentioned, different electrodes of one BPM can be at a different distance from the mechanical center of the BPM. Note it is much easier to bend the electrode in the radial direction than in the angular one; this is illustrated in Fig. 4.19. So the electrodes Y+ and Y– could be displaced vertically but not horizontally and the X+ and X– could be displaced mainly horizontally. The displacement introduces certain offsets of the electrical BPM center from the mechanical one. The electrical center of the BPM is defined as a point equidistant from all four antennas. The RF cables connecting the BPM to the electronics could also have slightly different lengths and as a consequence different attenuations. This fact also adds to the offset. We would like to measure the offset and to take it into account so that measuring the zero beam position we will know for sure that the beam is in the mechanical center of the BPM. It does not solve the problem of the absolute beam position measurements, since the mechanical center of the BPM is aligned to other beamline elements also with an accuracy that is 100 μm in order of magnitude, but it does reduce the degree of uncertainty. Besides that, the absolute position measurement by the BPMs is not required.

For the offset measurements the electrode length is made different from ¼λ. One can use the antennas not only to pick-up the beam signal, but also to inject some RF power into the BPM. The horizontal displacement of the Y electrodes from the mechanical center is negligible. Thus any of Y electrodes would be a very symmetric RF source with respect to the vertical symmetry plane of the BPM. That is to say a Y electrode excites a field in the BPM symmetric to the mechanical center. If the X electrodes are equidistant from the mechanical center we will sense equal signals on X+ and X– electrodes. Any radial displacement of the X electrodes will result in a difference in the X+ and X– signals. So measurements of the S_{21} parameters from a Y electrode to the X+ and X– ones contain information about the horizontal displacement of the electrical BPM center from the mechanical one. We would like to do the S_{21} measurements at 1.3 GHz to take into account the RF cable differences and to use our BPM electronics for the calibration. If the antennas' length is $(2n+1)\lambda/4$, i.e., ¼λ or ¾λ then the S_{21} has a minimum at 1.3 GHz. For our very first BPM we have built with a strip length of 173 mm (¾λ for 1.3 GHz) the measured S_{21} from Y to X electrodes is plotted in Fig. 4.20. The frequency dependence of the S_{21} parameter in the vicinity of 1.3 GHz is very steep. This would lead to a very large error in the offset measurements. But as one can see the maximum of the function is very broad. To make the offset measurements reliable one has to design the BPM in a way that the electrodes have a good coupling to the 1.3 GHz component of the electron beam and the S_{21} parameter measured from the Y electrodes to the X ones has its maximum in vicinity of 1.3 GHz. For this reason the electrodes on our ¼λ BPM are 40 mm long. The S_{21} parameter of the BPM is shown in Fig. 4.21. The spectrum of the beam measured with the same BPM at the ELBE injector is shown in Fig. 4.22. The design meets both requirements namely the response function of the BPM to the beam and the S_{21} have maxima near 1.3 GHz.
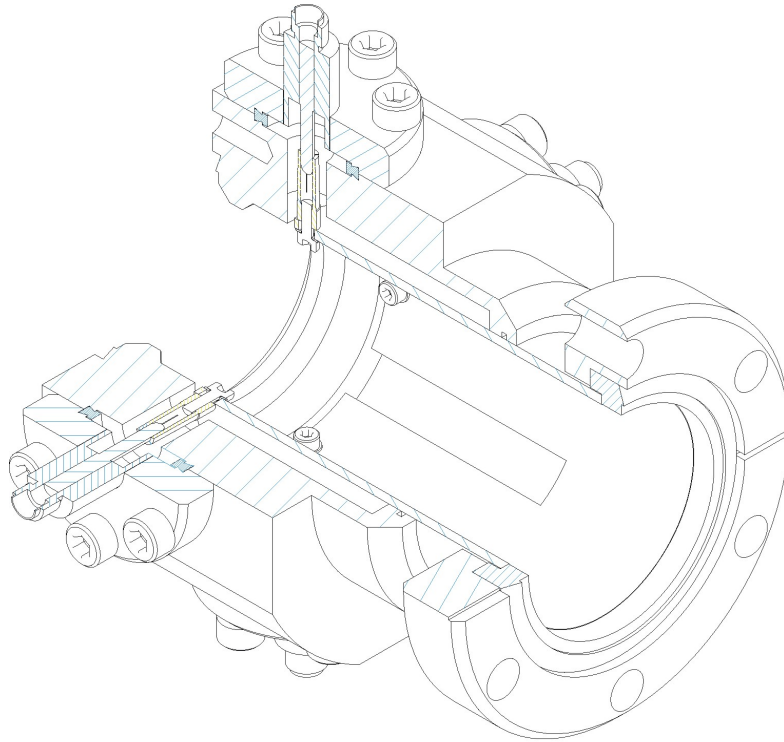
Figure 4.17 CAD drawing of the ¼λ BPM

Figure 4.18 Photograph of the ¼λ BPM and the ¾λ BPM

Further measurements with the beam have confirmed that there is no any significant difference in the new BPM response at 1.3 GHz from the response of the ¾λ BPM with 173 mm long electrodes. Afterwards it was decided to equip ELBE with the new

compact BPMs. Up to now 20 BPMs with design shown in Fig. 4.17 were manufactured and have been installed at ELBE. The BPMs are also used for the beam current difference measurements as a part of the machine protection system [4.16]. The BPM detectors are only one part of the BPM system developed and installed at ELBE. Another essential part is the BPM electronics which is described in the next section.
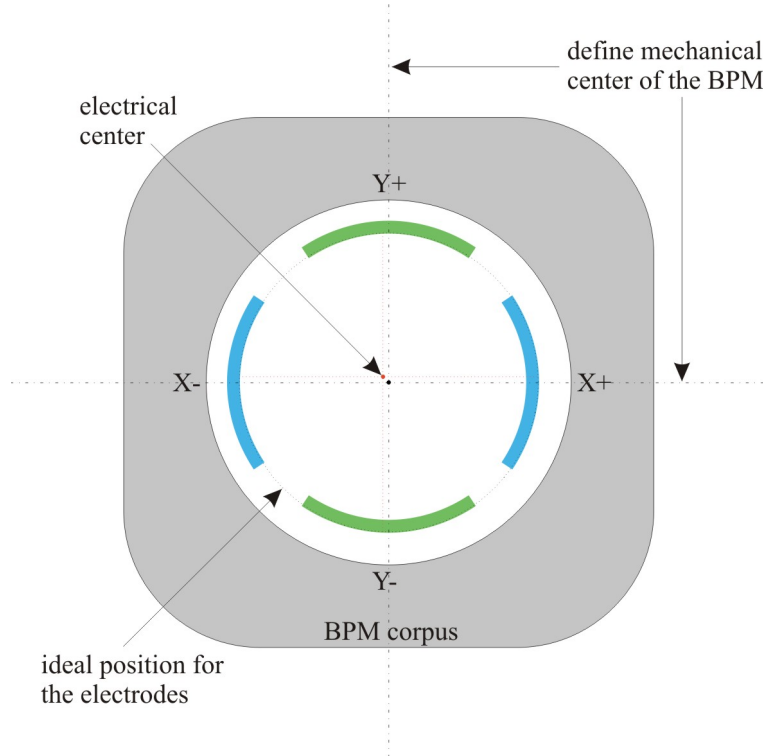
Figure 4.19 Difference between the mechanical center of the BPM from electrical one
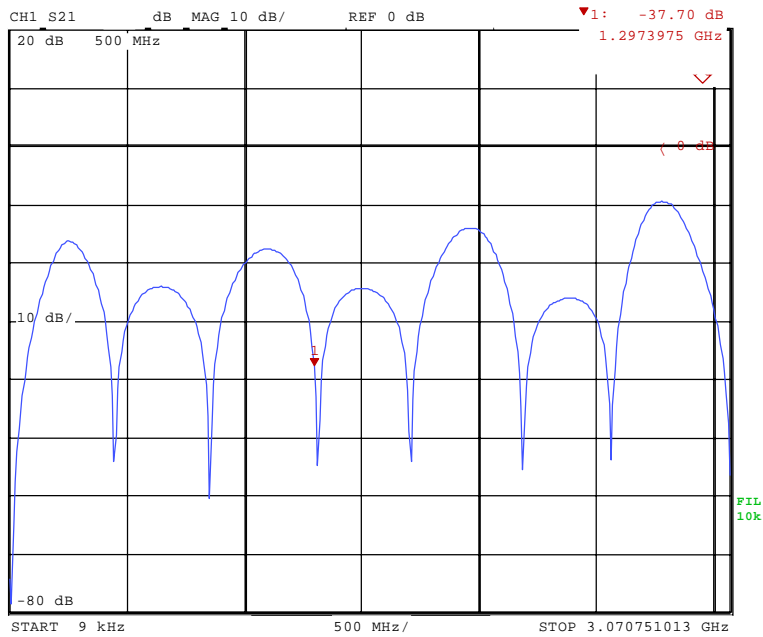
Figure 4.20 Measured S$_{21}$ from Y to X for the ¾λ (175 mm) BPM
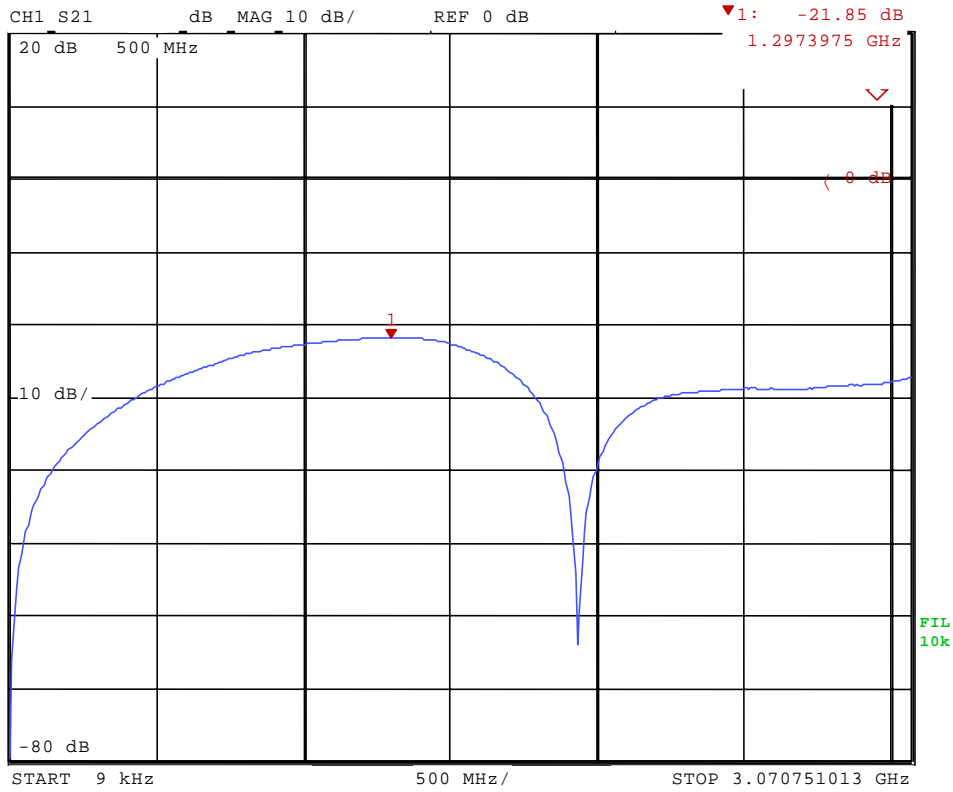
Figure 4.21 Measured S$_{21}$ from Y to X for the ¼λ (40 mm) BPM
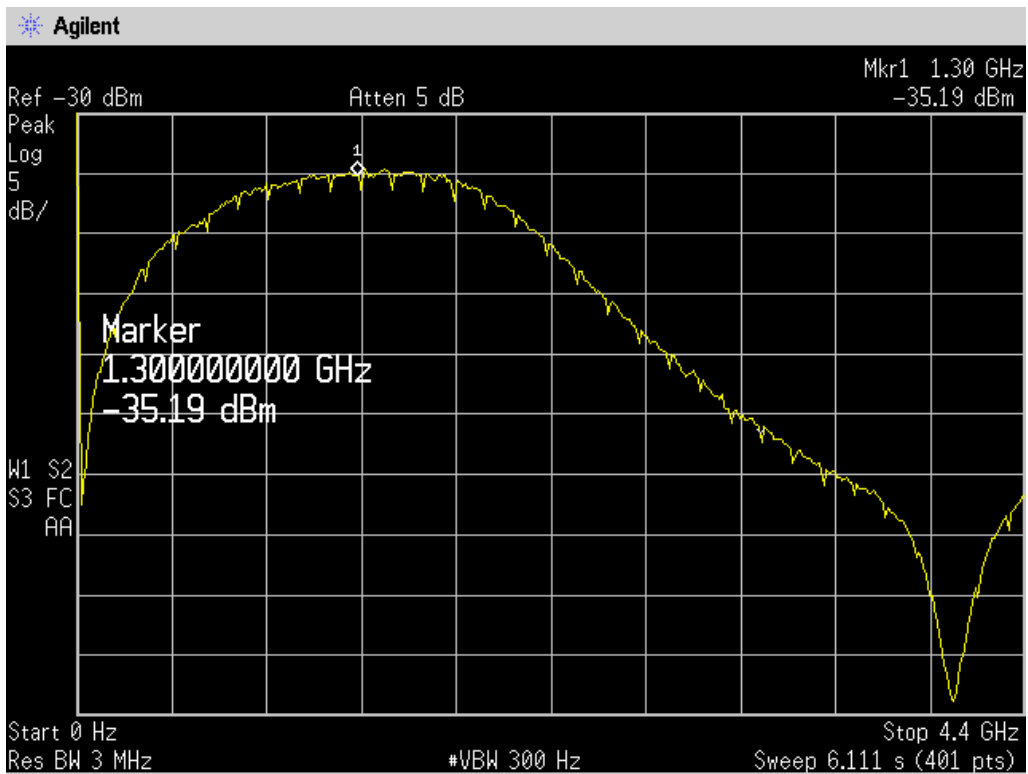
Figure 4.22 Beam spectrum measured with the ¼λ BPM at the ELBE injector

4.3   BPM electronics

4.3.1   The structural design

   In essence there are two different ways to build BPM electronics. These are operation in the time domain and operation in the frequency domain. The BPM electronics for ELBE is operating in the frequency domain. There are several reasons for that. First of all, as equation 4.13 clearly shows, the signal-to-noise ration (SNR) is a key parameter for the resolution of a BPM system. The noise power is proportional to the measurement bandwidth. The beam signal has a discrete spectrum. This is why choosing properly the central frequency and making the measurement bandwidth as narrow as possible give a significant increase in the signal-to-noise ratio thus improving the resolution. This is why the prime beam measurements with the BPM were done in the frequency domain. The fundamental linac frequency of 1.3 GHz was chosen as the BPM electronics operational frequency, since the beam spectrum has the 1.3 GHz component at any bunch repetition rate.
   The BPM electronics schematic is shown in Fig. 4.23. The core element of the BPM electronics is the logarithmic detector AD8313 made by Analog Devices Inc. [4.17]. The AD8313 was introduced in early 1998. This is a direct RF to DC converter rated up to 2.5 GHz originally intended for mobile communication technology. The response of the logarithmic detector measured at 1.3 GHz is shown in Fig. 4.24. The detector has an enormous linear dynamic range going from –65 dBm up to –5 dBm. The dynamic range of 60 dB corresponds to a three orders of magnitude of beam current. That means the BPM electronics based on the detector and designed for the maximum beam current of 1 mA in will be still operational with a beam current of 1 μA in order of magnitude. The BPM electronics is placed outside of the accelerator hall for radiation damage reasons. Long HELIAX$^®$ type RF cables connect the BPMs to the electronics. The cables have attenuation in the range from 5 dB to 6 dB at 1.3 GHz. The inter-digital finger filter is placed in front of the BPM electronics. The filter rejects all BPM signal components except the one at 1.3 GHz. The S_{21} parameter of the filter is shown in Fig. 4.25. The filter has a 3 dB bandwidth of 10 MHz. This is the 10 MHz we used to calculate the possible BPM resolution in Section 4.2.6.
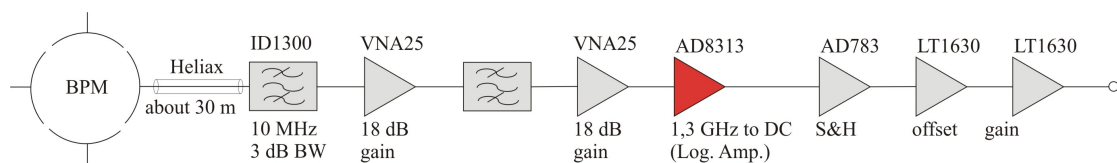

Figure 4.23 The BPM electronics schematic

   The BPM signal needs some gain to be matched to the linear range of the logarithmic amplifier. This is done with two constant gain MMIC amplifiers (Monolithic Microwave Integrated Circuit) VNA-25 from Mini-Circuits [4.18]. According to the data sheet the amplifiers have a gain of 18 dB at 1.3 GHz and are rated up to 2.5 GHz just like the logarithmic detector. There is a band-pass filter between the amplifiers. Otherwise the second amplifier will amplify noise of the first one. To demonstrate the function of the filter, the S_{21} parameter of this group is measured once with the filter and once without one. Results of the measurements are shown in Fig. 4.26. Thus the group of the amplifiers with the filter in between has a

constant gain of 22 dB. The bandwidth of the filter defines the bandwidth of the group and is about of 50 MHz.
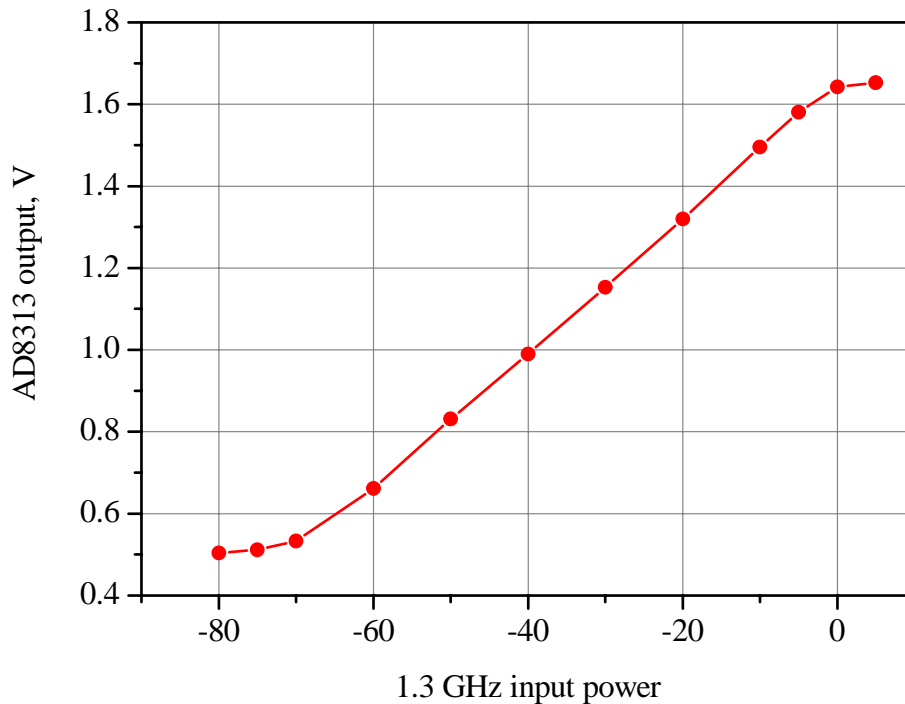
Figure 4.24 Characteristic of the AD8313 logarithmic detector measured at 1.3 GHz

The logarithmic detector is the border between the RF part of the electronics and the DC part. The output of the logarithmic detector varies from 0.5 V to 1.5 V. The ADC we use measures signals in the range ±5V so the output of the log amp has to be matched to the ADC range. It is done using two operational amplifiers. One of them is responsible for the log amp output offset and the other one for its amplification. The gain and the offset are adjustable so we can adjust different channels very precisely making them almost equivalent.

The logarithmic detector has a bandwidth of about 10 MHz. With a bunch repetition rate of 13 MHz the AD8313 provide a DC output which can be simply amplified and sampled by an ADC. When the bunch repetition rate becomes less than a certain value the logarithmic detector output shows the pulsed structure as well. Such a situation is demonstrated in Fig. 4.27. A short pulse generator is used to simulate the beam signal. The generator signal is shown on channel #1 of the oscilloscope. Output of the AD8313 evaluation board is connected to channel #3. On the upper oscillogram the generator frequency is high enough to make the AD8313 output a DC signal. On the lower oscillogram the generator frequency is reduced and is less than the logarithmic detector bandwidth. As one can see in this case every pulse of the generator is transformed by AD8313 into another broader pulse but not into a DC signal. In the case of beam signal from the BPM the width of the logarithmic detector pulsed output is defined by the band-pass filter bandwidth or in anther words by its quality factor. The real signal has 100 ns of almost flat top. The ADC used for the data acquisition has a sampling time of 400 ns. Obviously even with proper timing the ADC does not have enough time to measure the signal correctly.
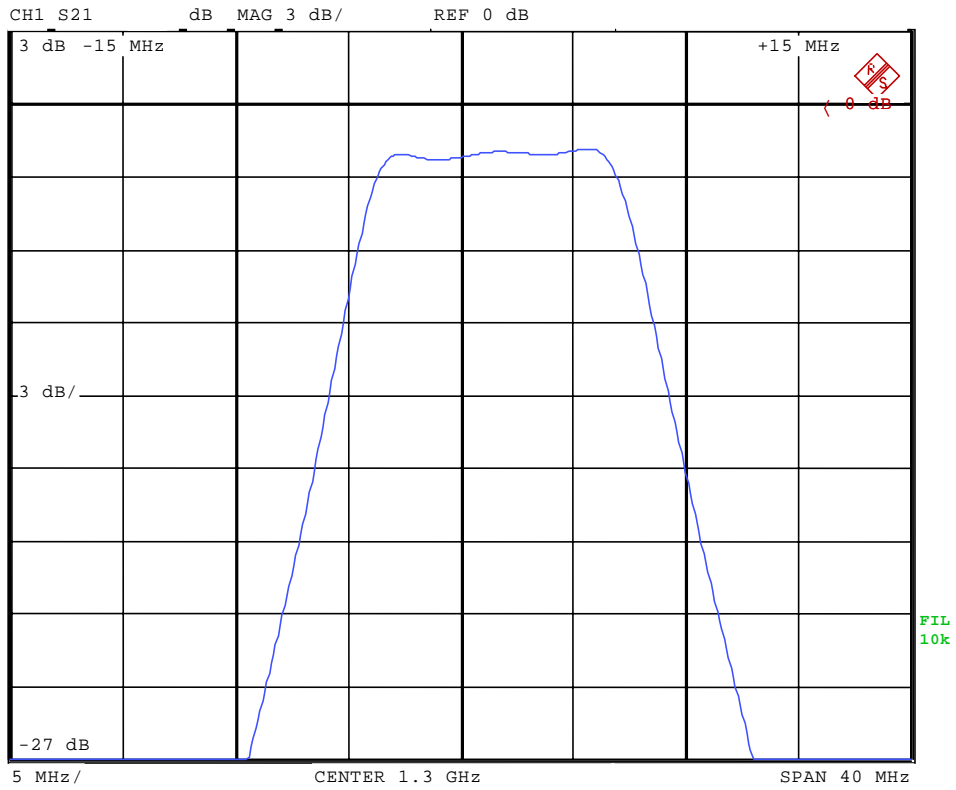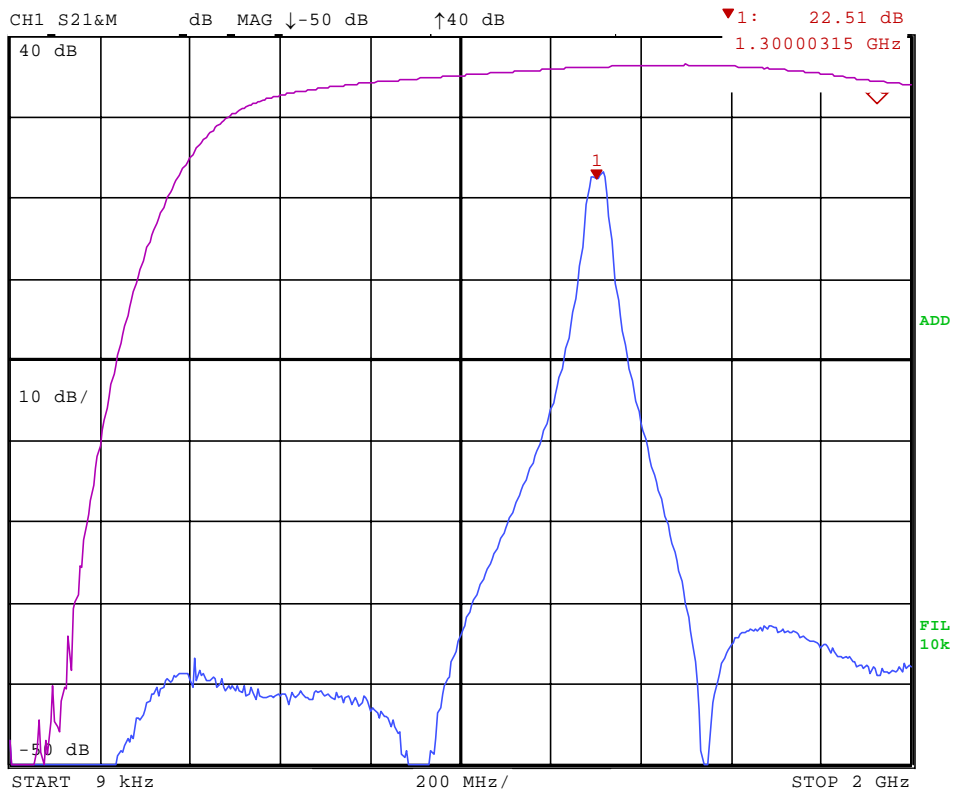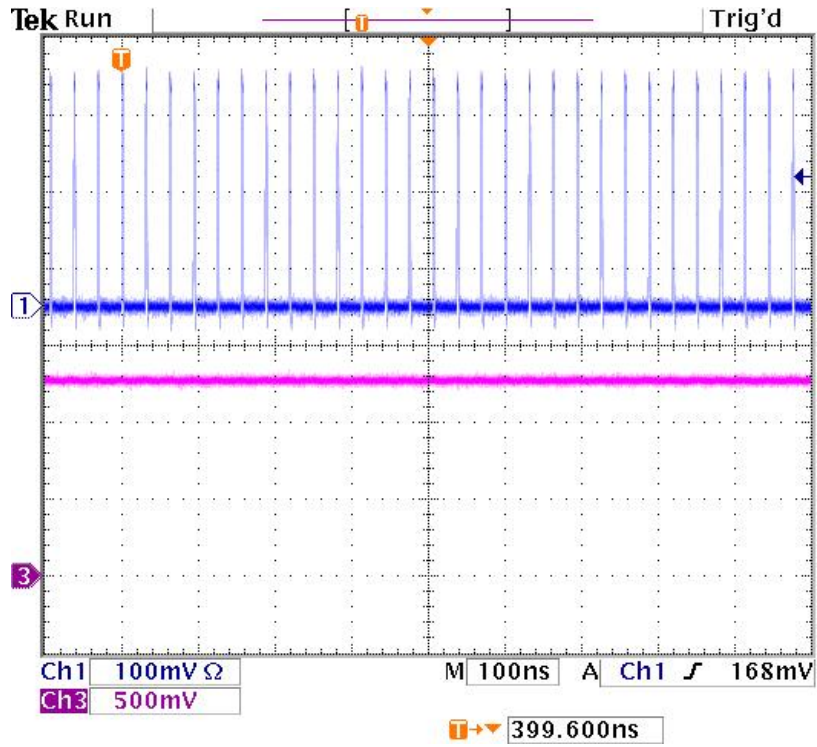
Figure 4.25 The band-pass filter characteristic

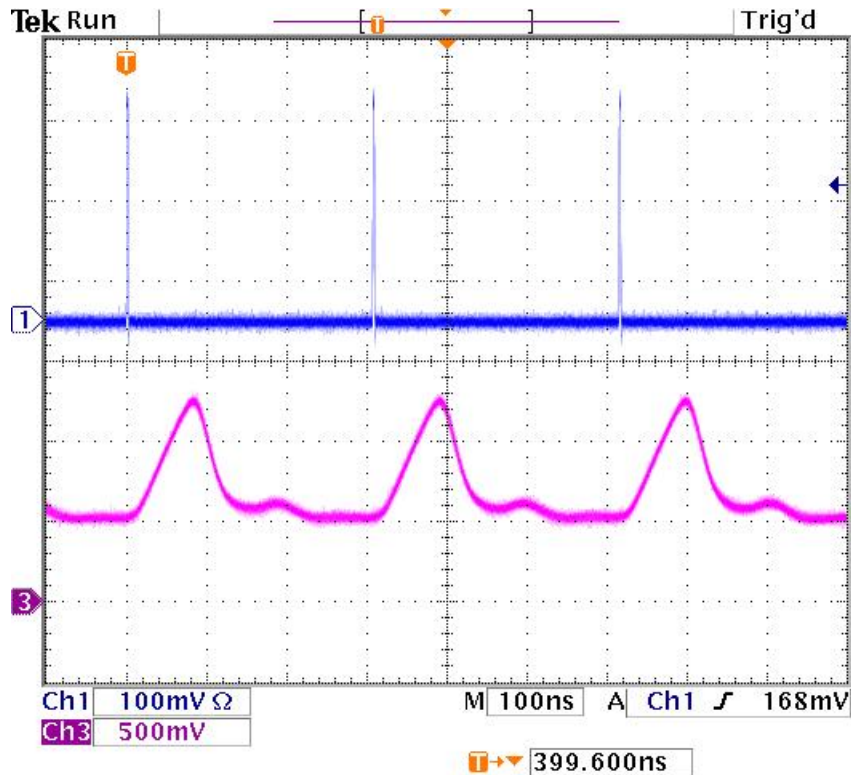*Figure 4.26 S$_{21}$ of the two MMIC amplifiers with (blue) and without (red) the filter in between*

(a) The input signal frequency is high enough to make the log amp output to a DC signal.

(b) When the input signal frequency is not high enough the log amp output becomes pulsed as well

Figure 4.27 Log amp response at different input signal frequency channel #1 shows the log amp input; channel #3 shows the log amp output

For that reason a sample and hold (S&H) amplifier is built in between the logarithmic detector and the first trim gain operational amplifier. There is a logical trigger which is derived from the bunch frequency and the macropulse signal to control the S&H. Every BPM board has a delay line to compensate for a different arriving time of an electron bunch to different BPMs. The accurate S&H timing allows holding the maximum of the AD8313 signal providing enough time for the ADC sampling. Certainly the ADC uses an external clock linked to the bunch frequency. The sampling frequency of the ADC is constant and equals 101.5625 kHz.

4.3.2 BPM system accuracy

To measure the BPM accuracy one has to supply an "ideal beam", in other words, the beam used for such measurements has to have a stability much better than the assumed accuracy. Otherwise one could not distinguish between the beam motion and the electronics noise. All BPM electronics prototypes have demonstrated an accuracy in the range between 10 μm and 30 μm. Since it is not easy to make a beam stable to better than 10 μm we have measured the BPM accuracy with the help of a stable RF generator. For these measurements the generator was connected to the RF cables via a two-way splitter, which normally connects two opposite BPM channels, for instance X+ and X–, to the RF front end. Because of the band-pass filter the front end sees only one 1.3 GHz component of the broadband BPM signal. Thus the generator operating at 1.3 GHz was representing the ideal beam. The dependence of the 1.3 GHz component power of the BPM signal from the average beam current is known very well. Thus, adjusting the generator power level, we could simulate different currents of the beam. The BPM DAQ system was used in the measurements as well. There is a LabVIEW application which uses data from the DAQ and calculates the position of the electron beam as a function of time within the macropulse. These are real time measurements of the "beam position" with a sampling rate of 101.5625 kHz. The noise in the position signal is caused by the electronics noise only. Thus we know which beam displacement corresponds to the electronics noise. The position signal was measured for several milliseconds at different RF power levels of the generator. For every measurement standard deviation from the mean a value was calculated. The standard deviation is the accuracy of a single position measurement. Results of the measurements are shown in Fig. 4.28. The measured accuracy is plotted together with the one calculated for the BPM with the 10 MHz band-pass filter. There is a difference because the BPM electronics introduces extra noise, i.e., the signal-to-noise ratio actually gets worse.

4.3.3 Understanding the system accuracy

For a better understanding of the difference between the resolution provided by the BPM itself and the entire BPM system some additional measurements were done. The BPM electronics has two parts. These are the RF part and the DC part. A convenient way to characterize the evolution of the signal-to-noise ratio in an RF technology is the noise figure approach. By definition the noise figure of a network is the ratio of the signal-to-noise power ratio at the input to the signal-to-noise power ratio at the output of the network

$$F = \frac{S_{in}/N_{in}}{S_{out}/N_{out}} \ . \tag{4.15}$$
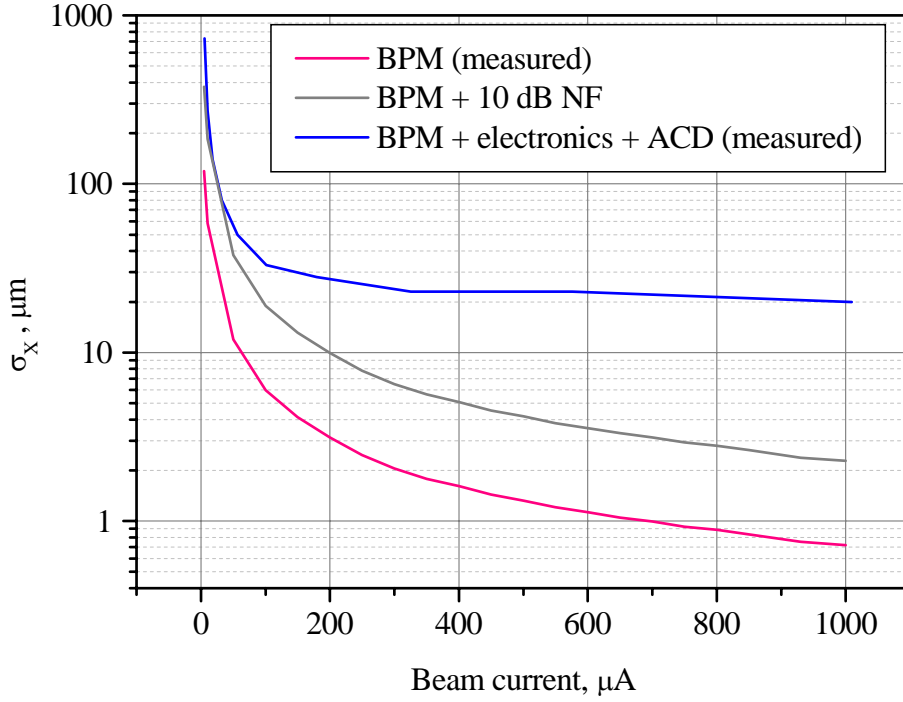
Figure 4.28 Accuracy of the beam position measurement

However, the value F is more often called "noise factor" or "noise figure in linear terms". So the name "noise figure" is reserved for the same quantity expressed in decibels, that is

$$NF = 10\log(F). \qquad (4.16)$$

The noise factor of a multistage system is written as follows [4.19]

$$F_{sys} = F_1 + \frac{F_2 - 1}{G_1} + \frac{F_3 - 1}{G_1 G_2} + ... + \frac{F_n - 1}{G_1 G_2 ... G_{n-1}}, \qquad (4.17)$$

where F_i and G_i are noise factor and gain of a ith stage respectively. The RF part of the electronics can be considered as if it consists of groups. The first one is the long RF cable with the band-pass filter connecting the BPM to the electronics. The second one consists of two MMIC amplifiers with another band-pass filter in between. The reason for such grouping is that the first group has no active gain and its noise factor is equal to its loss factor. The noise factor of the second group can be measured so that there is no need to measure the noise factors and gains of every element. The noise figure of the second group was measured with the help of a 2075 Noise-gain Analyzer made by Advanced Electronics. The noise figure is measured to be 5.9 dB. The loss factor of the cable with the band-pass filter is typically about 5 dB. Thus using Eq. 4.17 we calculate the noise figure of the RF part of the BPM electronics equal to 10.9 dB. As soon as the noise figure is found we know the signal-to-noise ratio at the output of the RF stage of the electronics. The resolution with this signal-to-noise ratio is calculated using Eq. 4.13 and is also shown in Fig. 4.28. As one can see the noise figure of 10 dB defines the resolution of the BPM system for an average beam current of up to 30 μA. Nevertheless, the noise figure of 10 dB of the RF part of the electronics does not explain the system resolution at an average beam current of more then 30 μA.
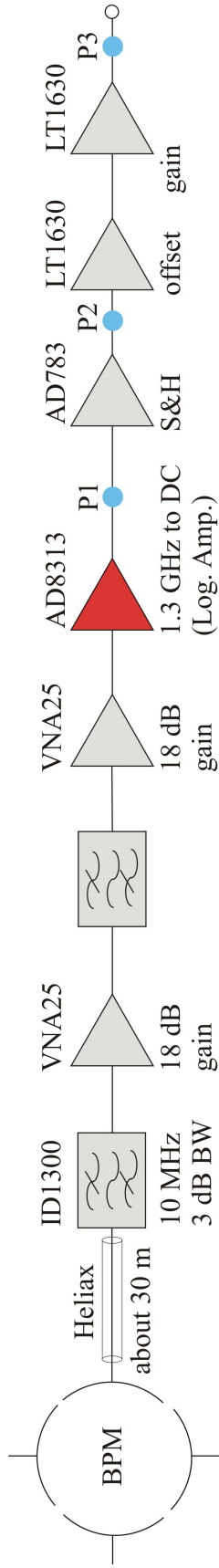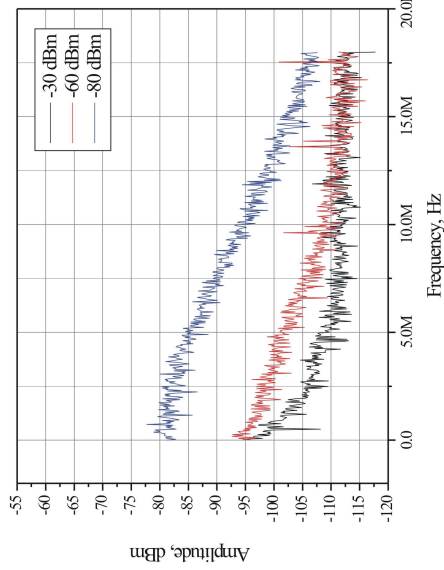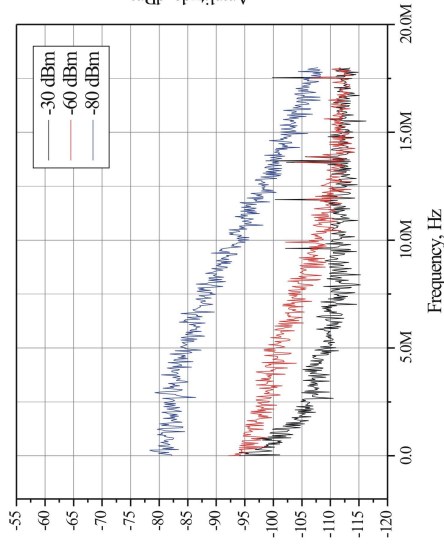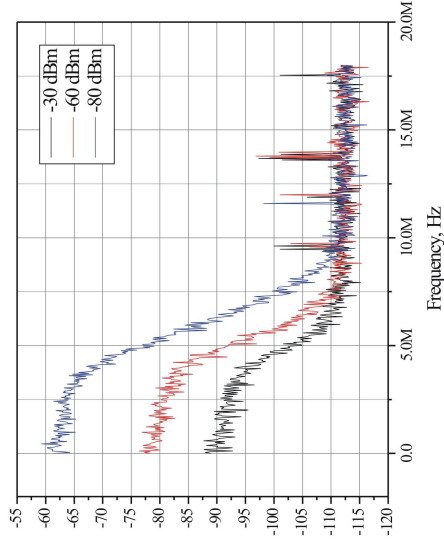
Figure 4.29 Noise evolution in the DC part of the BPM electronics with different input signal levels
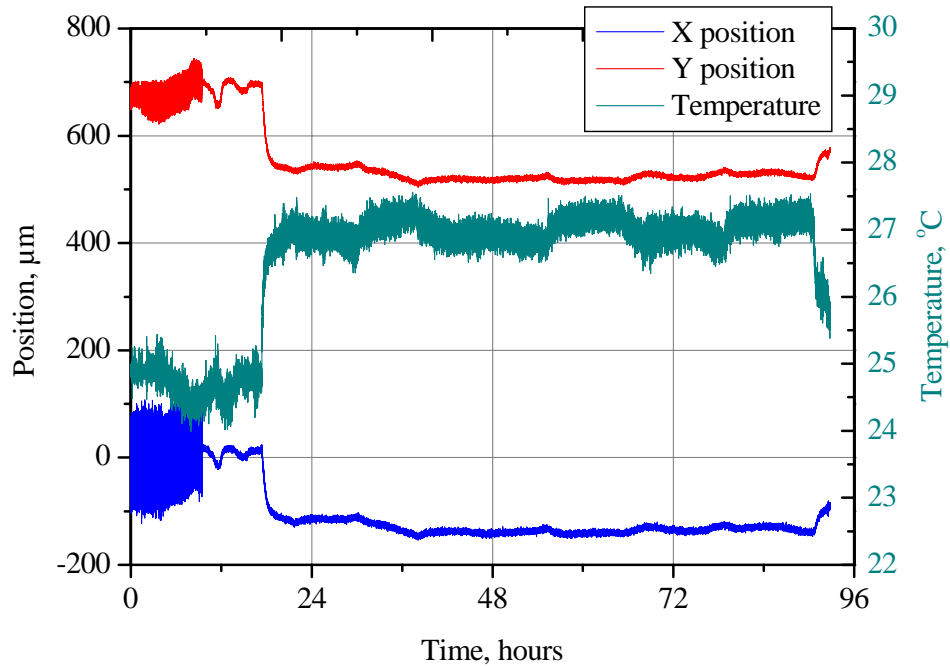

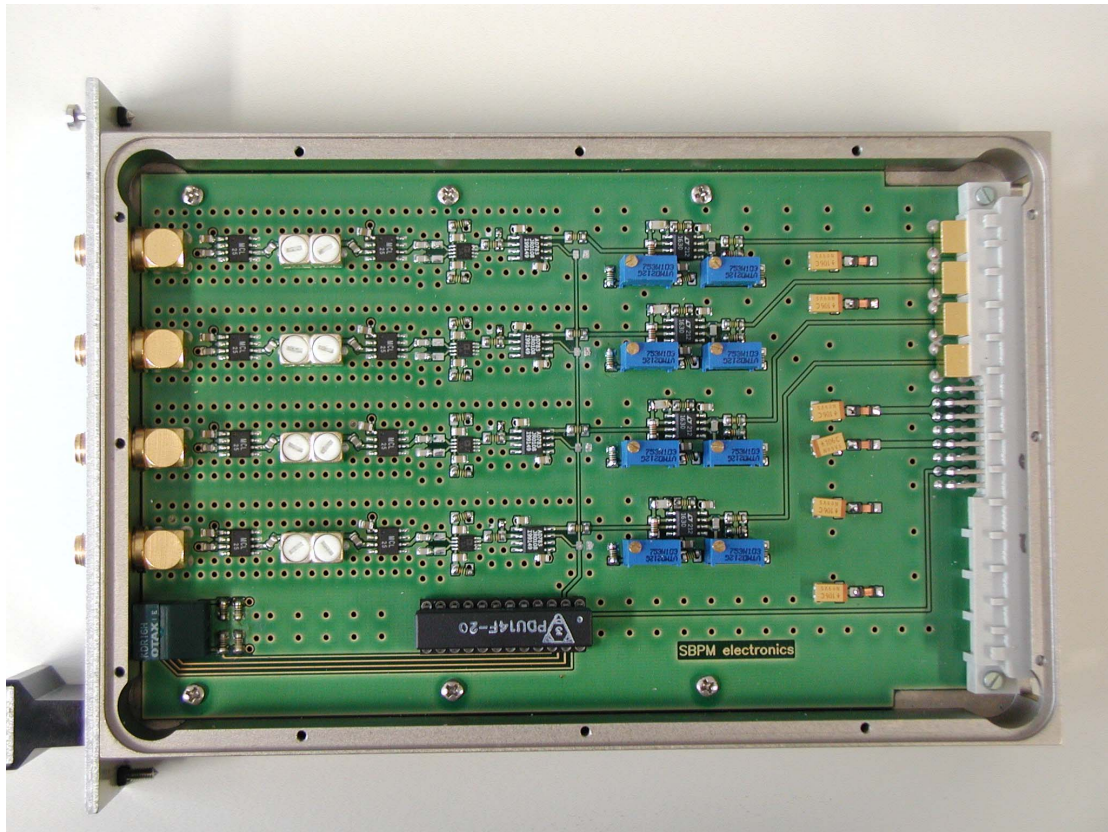*Figure 4.30 Long-term drift of the BPM electronics and the room temperature*

Figure 4.31 Photograph of the BPM electronics board

The DC part also introduces some extra noise. The level of the noise introduced by the DC part depends on the input signal level and defines the BPM system resolution at an average beam current of more than 30 µA. To track the noise evolution in the DC part or in other words to see the contribution to the noise from every element additional measurements were done in laboratory. The noise spectrum was measured at three different points of the circuit with a spectrum analyzer using an active probe. The measurement points are: the logarithmic amplifier output, the sample-and-hold amplifier output and the trim gain operational amplifier output. The measurements were done at three different levels of the input signal. The level of –30 dBm (black spectra) corresponds to an average beam current of 1 mA. The levels of –60 dBm (red spectra) and –80 dBm (blue spectra) correspond to a beam with average currents of 30 µA and 3 µA, respectively. Positions of the measurement points as well as the measurement results are shown in Fig. 4.29. One can make the following conclusions from the measurements. The noise level of the logarithmic amplifier decreases when the input signal increases, as expected. The sample-and-hold amplifier does not introduce significant noise. Confirmation of this is that the spectrum measured at point #2 is almost the same as the spectrum measured at point #1 regardless the input level. The trim gain operational amplifiers amplify the noise as well as the signal. The operational amplifiers modify the noise spectrum. That is explained by the amplifiers' bandwidth, which is in turn defined by the gain and GBP (gain bandwidth product). Since the trim gain is needed anyway, the main conclusion is that the BPM resolution for a beam current of more than 30 µA is predetermined by the logarithmic amplifier noise. We would like to note here that an improvement of the noise figure of the preamplifier stage will improve the BPM resolution only for a beam with an average current less than 30 µA.

The accuracy of the position measurement is better than 100 µm when the average beam current exceeds 25 µA. Note that the resolution of 100 µm was required and generally the resolution is better than the accuracy. Another important point is that if we are interested first in stable accelerator operation and second in measuring the average position of a macropulse, then the accuracy and the resolution are better by a factor of $1/\sqrt{N}$, where N is the number of measurements within the macropulse. If the sampling rate of the BPM ADC is about 10 µs and we measure the beam position, for example, for 10 ms, which is the typical time in our case then we measure 1000 points and that improves the measurement accuracy by a factor of 30.

4.3.4 Long-term stability

Some measurements were done to investigate the long-term stability of the BPM electronics. An RF generator with a four-way splitter was used as a stable source of 1.3 GHz signal. The position calculated by the BPM software from that signal was measured for several days and logged. The measurement has identified a position variation of about 200 µm from the daytime to the night time. The idea proposed as the reason for this variation is the room temperature change. In a second measurement the position was measured and logged together with the room temperature. The measurement shows a very good correlation between the position and the room temperature. A temperature change of about 2 °C was measured. The result of the measurement is plotted in Fig. 4.30. In the first measurement the BPM electronics, the RF generator, and the BPM ADC were placed together in one room and there were

still some questions open. The main one is: is it the BPM electronics drifting with temperature or is it the ADC or is it the RF generator? In the next measurement the RF generator was placed in a separate room where the temperature is stable. The electronics and the ADC were left on the same place. The result of the measurement was the same value of the position change correlated with the temperature. So the generator was not drifting. In the last measurement the BPM electronics were placed in the room with the RF generator to keep it at a stable temperature. The measurements did not show any position drift, while the temperature in the room with the ADC was still drifting. That means the ADC works stably as well as the RF generator. Hence the reason for the measured position drift is the temperature dependence of the BPM electronics. The correlation factors measured for the X plane and the Y plane are –71.3 μm/°C and –62.2 μm/°C respectively. Probably an additional temperature stabilization will be necessary for the BPM electronics serving the BPMs around the FEL undulator.

Figure 4.31 shows a photograph of the BPM electronics board. There are four channels on the board so that one such a board corresponds to a single BPM. The cross-talk coefficient from one channel to another one on the board was measured to be better than the isolation of the different antennas in the BPM, so that the interference of the different chains is negligible.

4.4 Software of the BPM system

4.4.1 BPM data acquisition

One can split the BPM software in two main parts. The first one is the data acquisition (DAQ) part. The second one is the operator interface. The software schematic is depicted in Fig.4.32. The BPM software is completed in LabVIEW, which is an object oriented graphic programming language.
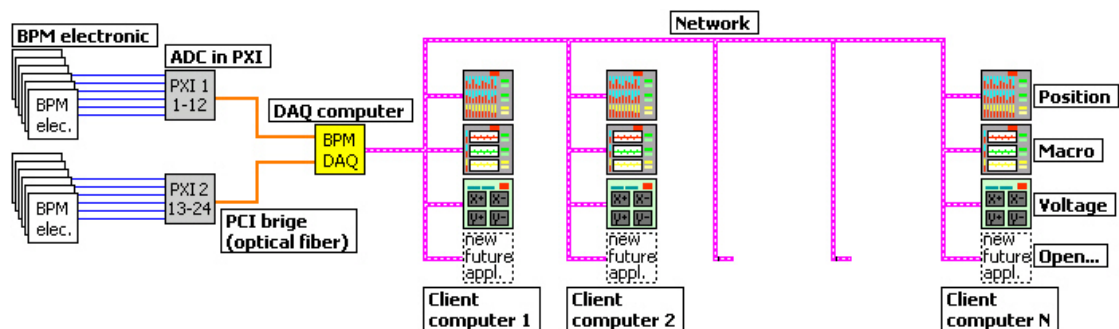

Figure 4.32 The BPM software schematic

Every BPM provides four broadband RF signals to the BPM electronics. The electronics have an individual electrical chain for every BPM channel. Thus there are four DC signals corresponding to a BPM. These signals are fed to an ADC. The DAQ system consists of six DATEL® CPCI-510L boards in the CompactPCI standard with 16 ADC each. The total number of ADC channels in the BPM DAQ system is 96. The resolution of the ADC is 12-bit. To reduce the RF cable length from the BPM to the BPM electronics the electronics are placed in two different 19`` chassis around the accelerator outside the accelerator hall. Two PXI chassis with ADC are located near

the BPM electronics. Both PXI chassis are connected to a DAQ computer via an optical fiber using the so-called MXI-3 (Multisystem Extension Interface for PXI and CompactPCI) interface. The distance between the DAQ computer and PIX module can be very long without introducing extra noise in the measurement data even in high noise environments. In fact all ADC boards work like one single PCI bus of the DAQ computer. The advantages of the PCI bus are the high possible data transfer rate, which can be practically up to ~130 MB/s and the relatively low cost. A chart comparing different buses used for a data acquisition is shown in Fig. 4.33 [4.20]. The ADC samples the BPM signals with a frequency of 101.5625 kHz, which is on one hand a subharmonic of 13 MHz and on the other hand is the smallest possible repetition rate. Thus the ADC sampling is always synchronized with the micropulse repetition rate of the accelerator. The DAQ LabVIEW program accomplishes the next functions: monitor if all ADCs are operating properly, configure ADCs, combine data from ADCs after acquisition, and publish the measurement data on the network. A screenshot of the BPM DAQ program in shown in the Fig. 4.34. The program gets information about macropulse length and about the beam mode (CW or pulsed) from the main ELBE control system to configure the ADCs. The total acquisition rate is about 20 MB/s with a maximum acquisition time of about 40 ms. In Fig. 4.32 the program is represented by the "BPM DAQ" element.
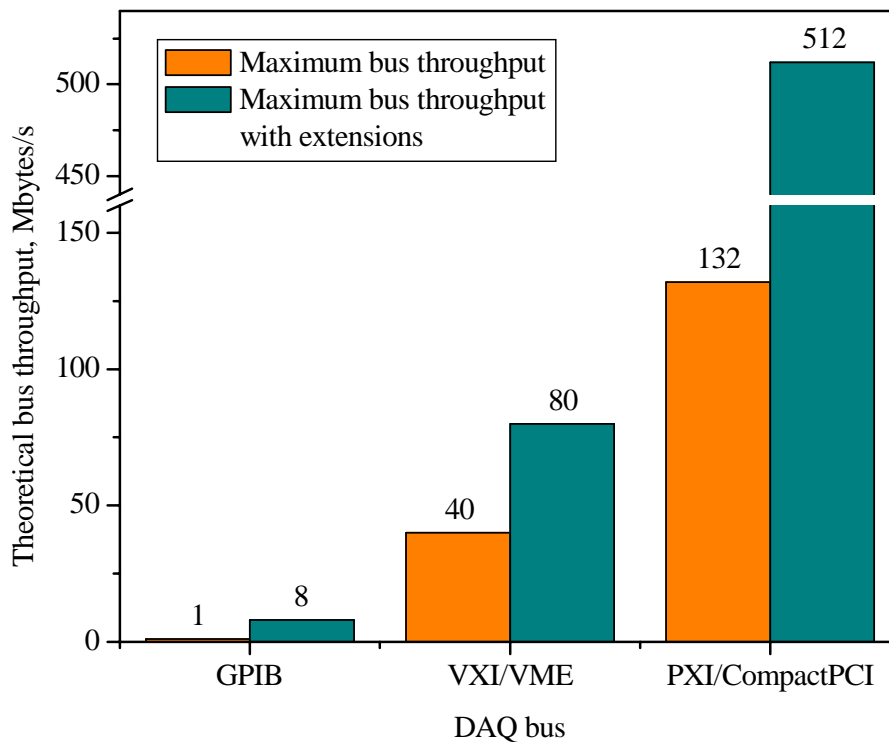

Figure 4.33 Comparison of the different DAQ buses

4.4.2 Operator interface

The second part of the BPM software is the operator interface. This is a set of programs which provide an accelerator operators with the information obtained from the BPM measurements. The data exchange between the DAQ program and the operator interface programs is realized using the DataSocket technology [4.21].

Basically the data are transferred from the DAQ computer to any client computer over a Local Area Network (LAN). This solution makes the system very flexible. The number of computers using the BPM measurements is almost unlimited. It is also possible to share the data over the Internet and to monitor the machine state as soon as one has an Internet access. Once the format of the data published by DAQ is known everyone can write his own application and use the measurement data.
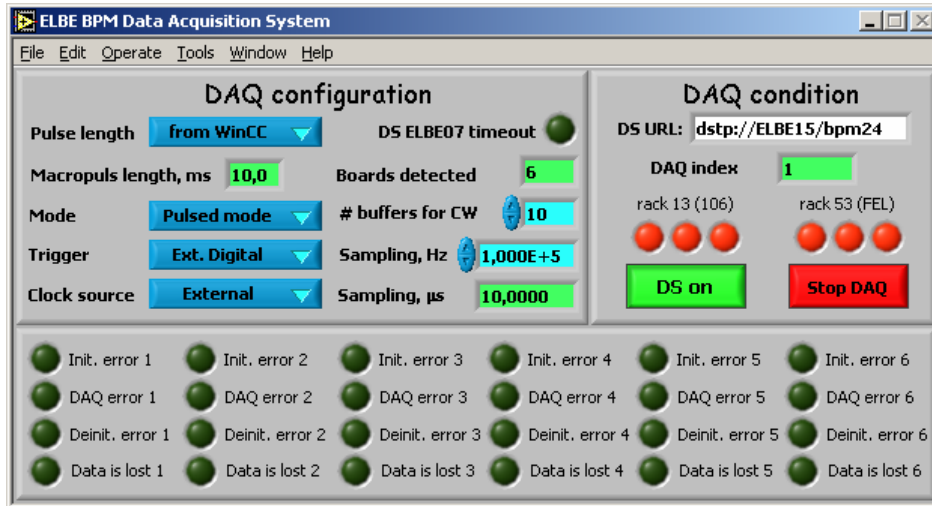

Figure 4.34 Screenshot of the BPM DAQ program
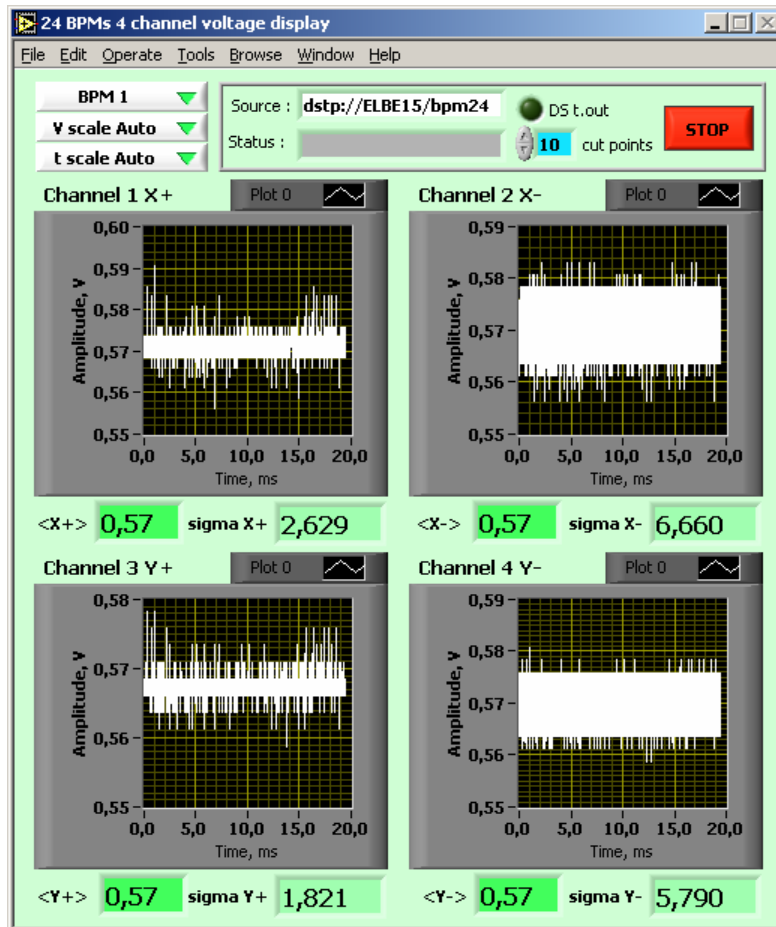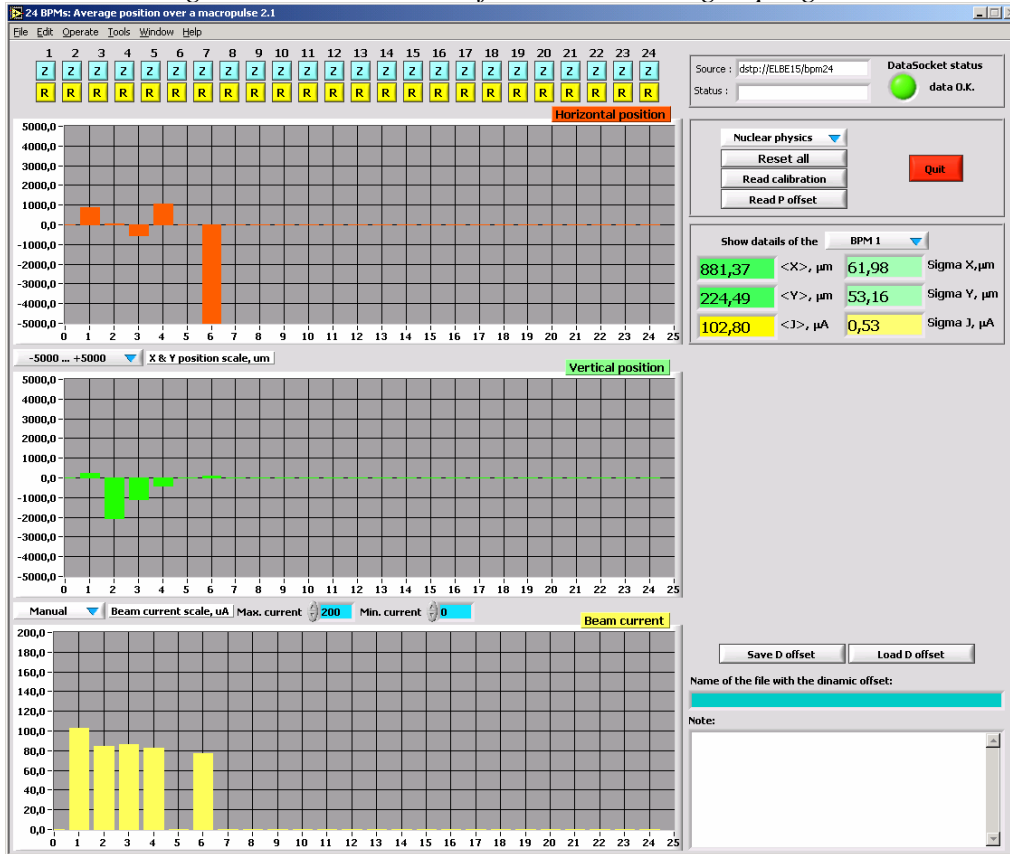
Figure 4.35 Screenshot of the "BPM voltage" program

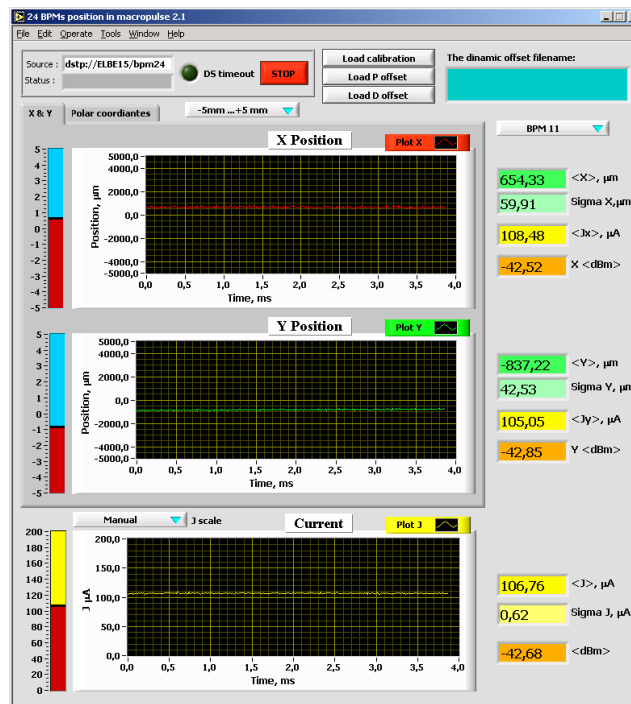*Figure 4.36 "BPM Position" screenshot*

Figure 4.37 "BPM Macro" screenshot

A set of such applications was written in LabVIEW for routine beam observation during machine operation. First, the most simple program is used to display the raw BPM data, namely the output voltage of the BPM electronics. That is just like a

simple digital 96 channel oscilloscope. The application is very useful and used mostly for setting of the BPM electronics, its tuning, debugging and troubleshooting. The user interface of the program is shown in Fig. 4.35. The second of the programs calculates and displays the beam position and intensity averaged over a macropulse, or over 20 ms in the case of CW operation, for all BPMs simultaneously. A screen shot of the program is shown in Fig. 4.36. One more program provides more detailed information but only for a single BPM. This program shows the position of the beam and the beam current as a function of time within a data acquisition. There is a screenshot of the program in Fig. 4.37.

All the programs need some information in addition to the ADC data to calculate the beam position and current. This is the calibration data. Every individual BPM electronics board is calibrated together with the RF cables delivering signals from the BPM to the electronics. The results of the calibrations of all boards are stored in one single ASCI file on the BPM DAQ computer. The BPM users program reads the calibration data during initialization. The BPM by itself, the long RF cables between the BPM and the electronics, and the small difference of the electronics channels introduce certain offsets in the position measurements. The offset is always the same for a given set of BPM, its cables, and electronics. Let us call it a "permanent offset". The offset is measured and the data are also stored on the BPM DAQ computer. For initialization the BPM user programs read the data as well. The optimal electron beam trajectory does not go always through an electrical center of a BPM. Hence once the optimal beam trajectory is found we still see a non-zero position of the beam in the BPMs. There is a software option that makes monitoring easier and gives a good reference for watching the actual beam trajectory. The optimal position of the beam can be set to be zero by introducing an artificial offset in the beam position calculation. Since the offset can be different we call it the "dynamical offset". For every optimal setting of the accelerator a set of the dynamical offsets is generated and stored so that when we call another setting of the accelerator we also can call the proper "dynamical offset" set. This option is also important for understanding the machine reproducibility.

As was mentioned, the applications can be installed at any computer, that means at the client station of the ELBE main control system (WinCC) as well. To prevent any interference between the WinCC and a BPM application every application is tested in the sense of CPU usage. The usage depends on the acquisition time length, but is not more than 30 %. The test is performed on a standard WinCC client computer.

4.5 Conclusion

The system of stripline beam position monitors was developed for the ELBE accelerator. The system makes possible a nondestructive time-resolved online observation of the electron beam position. Using the BPM of the JLab FEL as a starting point, a new compact BPM was developed. The technology of the BPM manufacturing is very reliable as well as the BPM itself during its use at the accelerator. At the present time 20 BPMs are manufactured, installed at the accelerator, and operational. The BPM is also used by a separate system for beam current measurements as a part of the machine protection system. The BPM electronics based on a logarithmic amplifier was developed, manufactured and operated at the accelerator. The software supporting the BPM system is made in LabVIEW. All system requirements are met. The achieved resolution of the beam position measurements is several times better than the required resolution of 100 µm.

Conclusion

The work performed in the framework of the thesis and presented in this report concentrated on the design of beam instrumentation and the electron beam parameter measurements at the radiation source ELBE. The infrared FEL imposes strong requirements on the electron beam quality, i.e., to such electron beam parameters as transverse emittance, energy spread, bunch length, and peak current. Among the applications of the electron beam at ELBE, the FEL is the most sensitive device to the beam quality and to the beam parameters' stability. Accurate and systematic beam measurements are a necessary step in the FEL commissioning.

Two different techniques used to measure the transverse emittance at ELBE were described. The emittance was measured in the ELBE injector where the beam energy is 250 keV and downstream of the accelerator module at a beam energy of about 12 MeV. It was demonstrated that there is no emittance growth during the beam acceleration by the superconducting linac. At the design bunch charge of the FEL, 77 pC, the normalized RMS emittance is measured to be about 8 mm×mrad. An electron beam with such an emittance will not cause any significant reduction of the FEL gain. However, a better accuracy of the emittance measurements is extremely desirable. The transverse emittance measurements at 77 pC bunch charge have a relative accuracy approaching 40 %. Furthermore, the accuracy of the emittance measurements at the low bunch charge, 1 pC in order of magnitude, is about 10 %. The situation is explained as follows. The average beam current in the diagnostic beam mode is limited for machine protection reasons. Hence, at low bunch charge one may make the macropulse much longer than in the case of higher bunch charge. Together with the nonlinearity of the combination of the Vidicon video camera and the Chromox view screen this leads to a lower signal-to-noise ratio of the beam profile measurements. Thus the SNR is much better in the case of low bunch charge. The situation can be improved using another type of video camera and a view screen made of a different material. CCD video cameras are approximately one order of magnitude more sensitive than the Vidicon type cameras and could be used to improve the emittance measurement accuracy. View screens made of YAG:Ce (Yttrium Aluminum Garnet doped with Cerium) crystals are commercially available now and have been successfully used for beam profile measurements. The YAG:Ce is a very efficient scintillator and produces much more light than the Chromox (Al_2O_3 ceramic). Thus it can be also used to improve the SNR and to make the emittance measurement accuracy better.

Results of the bunch length minimization in the ELBE injector using the stripline BPM were presented. The measurements are in good agreement with the transverse kicker cavity measurements. We have used the Martin-Puplett interferometer to

measure the bunch length at an electron beam energy of 12 MeV. The method and the experimental setup were described. The procedure for bunch length derivation from the interferometric measurements was explained. The experimental data are in good agreement with the bunch length predicted by PARMELA simulations. Thus at the exit of the accelerating module #1 a bunch with a charge of 77 pC was measured to be 1.4 ps long. As the next steps of the FEL commissioning the magnetic bunch compressor has to be put in operation and the bunch length has to be measured downstream of the S shaped beam line in the vicinity of the FEL undulator. While the Martin-Puplett interferometer is the most inexpensive way to measure the electron bunch length in the picosecond range the method has also some disadvantages. First of all to derive the bunch length from the measurement data a guess has to be made about the longitudinal bunch shape. We have assumed that the bunch shape is a Gaussian one. At the same time a Gaussian bunch shape is illogical for a linac beam, since such beams are not in equilibrium. We also have to make a guess on a shape of the low frequency cut-off function. However, the guess we did is explained well by the diffraction loss on the Golay cell input window. One more disadvantage of the method is that it does not work for a bunch length longer than 3 – 4 ps because of the low frequency cut-off. To overcome the problem one could use a detector with a bigger aperture. While measuring bunch length on a picosecond scale it is very desirable to do a crosscheck measurements using a completely different method. The electro-optical sampling has become to a very promising method of bunch length measurements. A Ti:Sa oscillator with a pulse length of about 10 fs is available at ELBE. Though there are several technical and physical problems to be solved, work on the electro-optical bunch length measurements is in progress at ELBE and is believed to be a good alternative to the Martin-Puplett interferometer measurements.

The system of stripline beam position monitors was developed for the ELBE accelerator. The system makes possible a nondestructive time-resolved online observation of the electron beam position. Using the BPM of the JLab FEL as a starting point, a new compact BPM was developed. The technology for BPM manufacturing is very reliable as well as the BPM itself during its use at the accelerator. At the present time 20 BPMs have been manufactured and installed at the accelerator, and are operational. The BPM is also used by a separate system for beam current measurements as a part of the machine protection system. The BPM electronics based on a logarithmic amplifier was developed, manufactured and operated at the accelerator. The software supporting the BPM system is made using LabVIEW. All system requirements are met. The achieved resolution of the beam position measurements is several times better than the required resolution of 100 μm. During experiments on a radiation physics beamline we discovered that there is a beam mode which the BPM system does not support. A beam with an average current of 10 nA is used to characterize the crystal producing the channeling radiation. Our present BPM system starts to show beam position at an average current of about 3 – 6 μA depending on the RF cable length. The addition of two cavity BPMs would be a good choice to upgrade the present BPM system so that a 10 nA beam could be located. One of the cavities could be placed downstream from the chamber with the radiating crystal while the second one could be placed upstream.

Bibliography

Chapter 1

[1.1]   W. B. Colson, C. Pellegrini, A. Renieri, Laser handbook volume 6, North-Holland (1990)

[1.2]   C. A. Brau, Free-Electron Lasers, Academic Press, Inc. (1990)

[1.3]   G. Dattoli, A. Renieri, A. Torre, Lectures on the free electron lasers theory and related topics, World Scientific Publishing Co. Pte. Ltd. (1993)

[1.4]   J. M. J. Madey, Nuovo Cimento 50B, (1979) 64

[1.5]   G. Dattoli, T. Letardi, J. M. J. Madey, Renieri, IEEE J. Quantum Electron. QE-20 (1984) 637

[1.6]   R. Wünsch, Freie Elektronen Laser an der Strahlungsquelle ELBE: Theoretische Vorhersagen und eindimensionale Modellrechnungen, Wissenschaftlich-Technische Berichte, FZR-276 (1999)

Chapter 2

[2.1]   P. Lapostolle, CERN rep. CERN/DI-70-36 (1970)

[2.2]   A. Hofmann, CERN 95-06, Vol. I (1995)

[2.3]   R. Twiss, N. Frank, Rev. Sci. Instrum. , 20, 1 (1949)

[2.4]   E. Courant, H. Snyder, Ann. Phys., 3, 1, (1959)

[2.5]   A. Chao, M. Tigner, Handbook of accelerator physics and engineering, World Scientific Publishing Co. Pte. Ltd. (1999)

[2.6]   R. Davidson, H. Qin, Physics of intense charged particles beams in high energy accelerators, Imperial College Press and World Scientific Publishing Co. Pte. Ltd. (2001)

[2.7]   J. Rosenzweig, G. Travish, Design considerations for the UCLA PBPL slit-based phase space measurement systems, PBPL (1994)

[2.8]   J. Teichert, private communication

Chapter 3

[3.1]   Radiation source ELBE design report (1998)

[3.2]   T. Smith, private communication

[3.3]   Peter vom Stein, Ph. D. Thesis "Hochfrequenz Elektroneninjektoren für CW-Beschleuniger", FZR-227, (1998)

[3.4]   P. Michel, private communication

[3.5]   J. D. Jackson, Classical Electrodynamics (Second Edition), John Wiley & Sons, Inc., New York, (1975)

[3.6]   V. L. Ginsburg, Teoreticheskaya fizika i astrofizika, Nauka, (1975)

[3.7]   K. Ricci, Ph. D. Thesis "Longitudinal electron beam measurements at the Stanford superconducting accelerator", Stanford University, (2000)

[3.8]   D. Martin, Polarizing (Martin-Puplett) interferometric spectrometers for the near- and sub-millimeter spectra. Chapter 2 in Infrared and Millimeter Waves, New York: Academic Press, (1982)

[3.9]   J. Lesurf, Millimeter-wave Optics, Devices & Systems, Adam Hilger Imprint by IOP Publishing Ltd., (1990)

[3.10]   N. Wiener, Acta. Math. 55, 117, (1930)

[3.11]   M. Born, E. Wolf, Principles of Optics, Pergamon, Oxford, (1975)

[3.12]   A. Murokh, J. Rosenzweig, M. Hogan, H. Suk, G. Travish, U.Happek, Bunch length measurement of picosecond electron beams from a photoinjector using coherent transition radiation, Phys. Rev. Lett., (1998)

[3.13]   P. Piot, Ph. D. Thesis "High brightness electron beam diagnostics and their applications to beam dynamics in a superconducting energy-recovering free-electron laser", Tomas Jefferson National Accelerator Facility, (1999)

[3.14]   M. Geitz, et al., Bunch length measurements using a Martin-Puplett interferometer at the TESLA test facility linac, Proceedings of the 1999 Particle Accelerator Conference, New York, (1999)

[3.15]   M. J. E. Golay, A pneumatic infrared detector, Rev. Sci. Instr. 18(5), 347 (1947)

[3.16]   M. J. E. Golay, The theoretical and practical sensitivity of the pneumatic infrared detector, Rev. Sci. Instr. 20(5), 816 (1949)

[3.17] E. Dereniak, G. Boreman, Infrared Detectors and Systems, John Wiley & Sons, Inc., (1996)

[3.18] A. Siegman, Lasers, University Science Books, (1986)

[3.19] F. Gabriel, private communication

Chapter 4

[4.1] Radiation source ELBE design report (1998)

[4.2] C. A. Brau, Free-Electron Lasers, Chapter 7, Academic Press, Inc. (1990)

[4.3] P. Evtushenko, P. Gippner, P. Michel, B. Wustmann, W. Seidel, D. Wohlfarth, A. Wolf, U. Wolf, R. Wünsch, C.A.J. van der Geer, Electron Beam Diagnostics and Undulator Field Adjustment of the ELBE IR-FEL, Proceedings of 25th International Free Electron Laser Conference, Tsukuba, (2003)

[4.4] M. Minty, Emittance preservation in linear accelerators, Proceedings of the Joint US-CERN-JAPAN-RUSSIA Accelerator School, St. Petersburg and Moscow, AIP Conference Proceedings 592, (2001)

[4.5] R. Lorenz, Cavity beam position monitors, Proceedings of the 1998 Beam Instrumentation Workshop, Stanford, AIP Conference Proceedings 451, (1998)

[4.6] R. Shafer, Beam position monitoring, Proceedings of the 1989 Beam Instrumentation Workshop, Upton, AIP Conference Proceedings 212, (1990)

[4.7] W. Barry, Nucl. Instrum. Meth., A301, (1991)

[4.8] R. Schurig, Diplomarbeit "Strahllagemessung für den linac der Strahlungsquelle ELBE", Hochschule für Technik und Wirtschaft Dresden, (2001)

[4.9] V. Balakin, A. Bazhan, P. Lunev, N. Solyak, V. Vogel, P. Zhogolev, Experimental results from a microwave cavity beam position monitor, Proceedings of the 1999 Particle Accelerator Conference, New York, (1999)

[4.10] R. Ursic, R. Flood, C. Piller, E. Strong, 1 nA Beam position monitoring system, Proceedings of the 1997 Particle Accelerator Conference, Vancouver, (1997)

[4.11] K. Bane, M. Sands, Wake fields of very short bunches in an accelerating cavity, SLAC-PUB-4441, (1987)

[4.12] K. Satoh, Beam position monitor using wall currents, Rev. Sci. Instr. 4, 450, (1979)

Bibliography

[4.13] R. Shafer, Characteristics of directional coupler beam position monitors, IEEE Trans. Nucl. Sci. 32, (1985)

[4.14] G. Vismara, Signal processing for beam position monitors, Proceedings of the 2000 Beam Instrumentation Workshop, Cambridge, AIP Conference Proceedings 546, (2000)

[4.15] K. Jordan, JLab FEL, private communication

[4.16] A. Büchner, J. Voigtländer, F. Gabriel, H. Langenhagen, Machine interlock system improvements by new beam loss monitors, Annual Report of the Radiation source ELBE 2002, Wissenschaftlich-Technische Berichte FZR-375, (2003)

[4.17] http://www.analog.com/, 0.1 GHz–2.5 GHz, 70 dB Logarithmic Detector/Controller, data sheet of the AD8313 logarithmic amplifier

[4.18] http://www.minicircuits.com/cgi-bin/spec?cat=amplifier&model=VNA-25&pix=xx211.gif&bv=4

[4.19] Agilent Technologies, http://www.agilent.com, Application None 57-1

[4.20] National Instruments Corp., http://www.ni.com

[4.21] National Instruments Corp., http://www.ni.com/datasocket/

Acknowledgment

Erklärung

Hiermit versichere ich, dass ich die vorliegende Arbeit ohne zulässige Hilfe Dritter und ohne Benutzung anderer als der angegebenen Hilfsmittel angefertigt habe. Die aus fremden Quellen direkt oder indirekt übernommenen Gedanken sind als solche kenntlich gemacht. Die Arbeit wurde bisher weder im Inland noch im Ausland in gleicher oder ähnlicher Form einer anderen Prüfungsbehörde vorgelegt.

Diese Dissertation wurde im Institut für Kern- und Hadronenphysik und in der Zentralabteilung Strahlungsquelle ELBE im Forschungszentrum Rossendorf unter der wissenschaftlichen Betreuung von Dr. Peter Michel und Prof. Dr. Eckart Grosse angefertigt.

Die Promotionsordnung der Fakultät für Mathematik und Naturwissenschaften der Technischen Universität Dresden vom 20. März 2000 erkenne ich an.

Pavel Evtushenko

Dresden, den 15. März 2004